Symposium on Seeing

P R O C E E D I N G S

Kona, Hawaii, 20-22 March 2007

A symposium organized by the Mauna Kea Weather Center
and sponsored by the National Science Foundation

Scientific Organizing Committee:
Steven Businger (UH)
Tiziana Cherubini (UH)
Ryan Lyman (UH)
Doug Simmons (Gemini Observatory)

Scientific Program Committee:
Steven Businger (UH)
Tiziana Cherubini (UH)
Mark Chun (IFA)
Francois Rigaut (Gemini)
Mark Sarazin (ESO)
Brent Ellerbroek (Calthec)

Edited by: Tiziana Cherubini and Steven Businger

The papers in this book comprise the proceedings of the Symposium on Seeing held in Kona Hawaii, on 20-22 March 2007. The National Science Foundation sponsored the symposium under Grant No. 0644453. The symposium also had financial and in kind support from the Gemini and Keck observatories and the Mauna Kea Weather Center. Any opinions, findings, and conclusions or recommendations expressed in this material are those of the author(s) and do not necessarily reflect the views of the National Science Foundation or the Symposium's organizers.

TABLE OF CONTENTS

In order of program

First Authors Index 213

<u>Session 1:</u> Instrumentation and observations to quantify the magnitude and distribution of atmospheric optical turbulence.

Sub-session 1a: Standard instrumentation/Calibration

Assembling composite vertical atmospheric turbulence profiles from DIMM, SLODAR and MASS contemporaneous records at Paranal
MARC SARAZIN 3

Accurate turbulence measurements with MASS and DIMM
ANDREI TOKOVININ 4

An instrument to measure the atmospheric time constant
AGLAÉ KELLERER 10

Unresolved critical issues of optical turbulence that effect seeing determinations
FRANK EATON 16

The seeing monitors: Instrumental noise and cross-calibration
ZOUHAIR BENKHALDOUN 22

Characterizing the TMT site selection equipment
MATTHIAS SCHOECK 23

The Thirty Meter Telescope DIMM systems
WARREN SKIDMORE 24

The TMT MASS System: Characterization and Application
SEBASTIAN ELS 25

Sub-session 1b: New Instruments and Methods

An optical turbulence profiler for the terrestrial atmosphere boundary-layer
JULIEN BORGNINO 26

First results from a Lunar SHABAR at CTIO
PAUL HICKSON 29

Low Layer SCIDAR: a turbulence profiler for the first kilometer with very high altitude-resolution
REMY AVILA 30

MOSP: Monitor of Outer Scale Profile
AZIZ ZIAD 31

Characterization of atmospheric optical turbulence along two horizontal path and comparison with vertical path turbulence
MARJORIE SHOEMAKE 38

Waves and Turbulence over Mauna Kea
JOHN MCHUGH 39

Sub-session 1c: Site Measurements campaign and Results

The Mauna Kea ground-layer characterization campaign
MARK CHUN 40

The Advance Technology Solar Telescope Site Survey: Instrumentation, Results and application to adaptive optics systems modeling
THOMAS RIMMELE 41

Statistical turbulence vertical profiles at the Roque de los Muchachos observatory and Teide observatory
JESÚS J. FUENSÁLIDA 42

PARANAL DIMM and MASS-LITE Comparison after two years of operation
JULIO NAVARRETE 43

The Seeing and Turbulence Profile at Las Campanas Observatory: GMT Site Testing Progress Report
JOANNA THOMAS-OSIP 44

Characterizing optical turbulence at Dome A on the Antarctic plateau
JON LAWRENCE 45

Site testing at Dome C, Antarctica
JEAN VERNIN 46

Session 2: Adaptive optics, interferometry, and other approaches to mitigate atmospheric optical turbulence.

Special issues in atmospheric monitoring and characterization for future extremely large telescopes
BRENT ELLERBROEK 49

Atmospheric Turbulence Profiling using Multiple Adaptive Optics
LIANQI WANG 50

Comparison of atmospheric conditions as measured by dedicated monitors & as seen on an adaptive optics wavefront sensor
NANCY AGEORGES 51

Instantaneous Seeing estimates using closed-loop AO images
SZYMON GLADYSZ 52

The Anisoplanatic Point Spread Function in Adaptive Optics
MATTHEW BRITTON 58

The widest contiguous field of view at selected sites
JEFF STOESZ 59

Adaptive optics using multiple guide stars
CHRISTOPH BARANEC 67

Some measurements of the short term variability of r_0
L. WILLIAM BRADFORD 74

Two Applications of Turbulence Characterization that Improve Deep AO Imaging with the Laser
ERIC STEINBRING 78

SLODAR Turbulence Profiling
RICHARD WILSON 79

Real-time sodium layer thickness monitoring with the Altair Laser Guide Star System
FRANCOIS RIGAUT 84

Session 3: **Approaches for modeling atmospheric optical turbulence.**

Optical Turbulence simulations with meso-scale models. Towards a new ground-based astronomy era 87
ELENA MASCIADRI

Mesoscale simulations above Antarctica for astronomical applications: first approaches 89
FRANCK LASCAUX

"COSMIC: Space based GPS". Constellation Observing System for Meteorology Ionosphere and Climate (COSMIC) 100
STEVEN BUSINGER

Modeling Optical Turbulence and Seeing over Mauna Kea: Algorithm Refinement 102
TIZIANA CHERUBINI

Modeling and Forecasting Optical Turbulence with DEEST 103
SARA C. ADAIR

Influence of Coastal Meteorological Processes on Aerosol Transport 104
SETHU RAMAN

A Ten Year Cloud Climatology of the Hawaiian Islands as Derived by GOES system 105
RAMAN ALLISS

Haleakala Seeing Characterization and Improved Wind Models for Several Astronomical Observatories 107
LEWIS ROBERTS

Testing turbulence model at metric scales with mid-infrared VISIR 110
ANDREI TOKOVININ

Session 4: **Applications of optical turbulence observations and custom forecasting in telescope astronomy.**

The "Missing Link" Between Meteorology and Astronomy 113
DOUGLAS SIMONS

Thermal Seeing Modeling as a Design and Performance Analysis Tool 114
KONSTANTINOS VOGIATZIS

Seeing estimation from 200 mb wind speed in the ELT campaign 119
BOUNHIR AZIZA

A new model to forecast seeing and Cn2 profiles from meteorological profiles
HERVÉ TRINQUET 120

Climatology of Sierra Negra
ESPERANZA CARRASCO 121

The Role of Weather Forecasts in Gemini Scientific Operations
DENNIS CRABTREE 125

POSTER Session :

Intercalibration between DIMM units
MAÑUEL NUNEZ 129

On the use of satellite data for Atmospheric Extinction Studies
ANTONIA M. VARELA 135

Dome seeing subtraction from G-SCIDAR measurements
JESÚS J. FUENSÁLIDA 138

Determination of the velocity vector of turbulence layers from G-SCIDAR
BEGOÑA GARCÍA-LORENZO 142

Evaluation of projection effects when determining the velocity vector of turbulence layers velocity from G-SCIDAR observations
BEGOÑA GARCÍA-LORENZO 148

Preliminary results of site testing campaigns at Samarkand and Suffa observatories in Uzbekistan
YUSUFJON TILLAYEV 153

DIMMA: *the First Unmanned Differential Image Motion Monitor*
ANTONIA M. VARELA 154

MASS-DIMM setup at Palomar
MICHAEL THOMSEN 159

The hybrid Shack-Hartmann/G-SCIDAR instrument.
M. ÁNGELES C. RODRÍGUEZ-HERNÁNDEZ 170

Characterizing ground-layer turbulence with a simple lunar scintillometer.
ANDREI TOKOVININ 171

A G-SCIDAR instrument for the inter-calibration of the atmospheric turbulence between the Roque de los Muchachos and Paranal observatories 176
JOSE M. DELGADO

From the simulated annealing method to Single Star Scidar.
ZOUHAIR BENKHALDOUN 177

Generalized Scidar measurements at Mt. Graham.
SEBASTIAN EGNER 178

Some observing campaigns with Single Star SCIDAR.
HABIB ABDELFETAH 184

Site testing in the northwest of the Argentina.
PABLO RECABARREN 185

The Past, Present, and Future of Site Testing for the Southern African Large Telescope (SALT). 189
STEVEN CRAWFORD

Climatology at the Roque de los Muchachos Observatory: Tropospheric and ground level regimes. 192
ANTONIA M. VARELA

Preliminary study of the seasonal variation of optical seeing above Oukaimeden site in the Moroccan High Atlas Mountains. 204
ABDELOUAHED ABAHAMID

Analysis of diurnal and seasonal variation of Fried's coherence length, isoplanatic angle, and greenwood frequency. 205
DARIELLE DEXHEIMER

Atmospheric conditions by dust pollution over ELT sites.
EL ARBI SIHER 206

How to Monte-Carlo Simulate the Optical Turbulence Boiling Beyond the Frozen Flow Hypothesis. 207
AMOKRANE BERDJA

El Roque de Los Muchachos site characteristics.
GIANLUCA LOMBARDI 209

SESSION 1

INSTRUMENTATION AND OBSERVATIONS TO QUANTIFY THE MAGNITUDE AND DISTRIBUTION OF ATMOSPHERIC OPTICAL TURBULENCE.

Assembling composite vertical atmospheric turbulence profiles from DIMM, SLODAR and MASS contemporaneous records at Paranal

Marc Sarazin* *(invited speaker)*
European Southern Observatory

Tim Butterley
University of Durham

Julio Navarrete
European Southern Observatory

Richard Wilson
University of Durham

ABSTRACT

Combining DIMM and MASS data provides access to the full profile of the atmospheric turbulence with a 500 m resolution at ground level. This has become a standard feature of most site monitoring programs worldwide. A version of SLODAR which probes the first kilometer above ground with 150 m resolution has been used in campaign mode at Paranal during the past years. The database accumulated when all three instruments were operated together is used to build a statistical estimate of standard turbulence profiles at Paranal.

*Corresponding author address: Marc Sarazin, European Southern Observatory
E-mail: msarazin@eso.org

Accurate turbulence measurements with MASS and DIMM

Andrei Tokovinin*
Cerro Tololo Inter-American Observatory, La Serena, Chile

Victor Kornilov
Sternberg Astronomical Institute, Moscow University, Moscow, Russia

ABSTRACT

We describe how to obtain accurate measurements of the C_n^2 integral in the free atmosphere and in the ground layer with a combined MASS-DIMM instrument. The instrument is briefly presented. The definition of "seeing" and its limits is re-stated. We evaluate various systematic effects and biases in the MASS method (semi-saturated scintillation, finite exposure, spectral response, non-poisson noise, inner scale) and in the DIMM method (noise, influence of aberrations, centering algorithms, finite exposure, propagation) by combining analytical approach with numerical simulation. Examples of the MASS-DIMM data are given.

*Corresponding author address: Andrei Tokovinin, Cerro Tololo Inter-American Observatory, Casilla 603, La Serena, Chile
E-mail: atokovinin@ctio.noao.edu

1. Introduction: what is "seeing"?

Image spread in a telescope caused by the optical turbulence in the atmosphere, *seeing*, is quantified by the Fried parameter r_0 or, equivalently, by the integral of the refractive-index structure constant C_n^2 over propagation path, $J = \int_{\rm path} C_n^2(z){\rm d}z$, with $r_0^{-5/3} = 0.423(2\pi/\lambda)^2 J$ (Roddier 1981). Quite often the seeing is expressed in radians or arcseconds as $\varepsilon_0 = 0.98\lambda/r_0$. However, the actual width of stellar images is, generally, not equal to ε_0, being influenced (sometimes significantly) by other factors such as finite telescope size, outer scale, guiding.

The above devinition of seeing is formulated for the Kolmogorov spectrum of optical distortions. It presumes that distortions are a stationary random process, while in fact they are not. Turbulence is intermittent, "patchy" in space and time (like clouds) and obeys the Kolmogorov model only approximately at spatial scales from $\sim$1 cm to $\sim$1 m. Seeing monitors measure wavefront distortions in this range and interpret them in terms of a single parameter r_0, seeing. Clearly, this parameter is only a theoretical abstraction, so it makes no sense to define or measure it with a very high accuracy (say 1%). As a parameter of the random process, r_0 cannot be "instantaneous".

2. MASS-DIMM instrument

Seeing is usually measured by a Differential Image Motion Monitor (DIMM) (Sarazin & Roddier 1990). Recently, a new instrument was developed by Kornilov et al. (2003) to measure the seeing in the free atmosphere (FA) above $\sim$500 m – the Multi-Aperture Scintillation Sensor (MASS). DIMM is sensitive to the phase distortions, while MASS measures the amplitude fluctuations, *scintillation*. Yet both deliver the same parameter, r_0 or J, with the only difference that DIMM samples the whole path, while MASS - only its upper part. The difference $J_{\rm GL} = J_{\rm DIMM} - J_{\rm MASS}$ informs us on the seeing produced in the ground layer (GL) below 500 m. The estimate $J_{\rm GL}$ makes sense only if both methods are accurate.

We combine MASS and DIMM in a single instrument, MASS-DIMM (Tokovinin & Kornilov 2007). It shares the light collected by a small ($D \geq 25$ cm) telescope between two apertures of DIMM and 4 concentric annular apertures of MASS. Both instruments sample synchronously the same turbulent path, so the errors caused by the non-stationarity are avoided. Otherwise, they would seriously affect the precison of $J_{\rm GL}$.

To date, 22 MASS-DIMM instruments have been fabricated at CTIO. Of these, 6 are used in the TMT site-testing program, 4 were recently delivered for a similar ESO program, the remaining units serve for monitoring turbulence at existing observatories world-wide. Data from these instruments are already used in several studies, e.g. (Tokovinin & Travouillon 2006). MASS data from Cerro Tololo and Cerro Pachón are available on-line[1]. MASS delivered measurements of exceptional free-atmosphere seeing at Dome C in Antarctica. Quite surprisingly, periods of calm upper atmosphere with a stable seeing of $0.2'' - 0.3''$ during whole night have been observed at all sites regularly with a small, but non-negligible probability of 5% - 10%. Such conditions resemble Antarctic sites and are potentially very important for adaptive optics, extending its capabilities for critical science. These special conditions were not detected before with DIMMs, being masked by the ever-present GL seeing.

[1] See MASS database at http://139.229.11.21/

3. Accuracy of MASS

MASS is essentially a fast photometer. Fluctuations of the stellar flux produced by the atmosphere are expressed as scintillation indices (normal and differential between pairs of apertures), while the signatures of instrumental effects (shot noise, counting statistics, background) are carefully removed from the calculated indices (Tokovinin et al. 2003). The indices are related to turbulence by means of *weighting functions* (WFs) which depend only on the aperture geometry and spectral bandwidth. In this sense, the calibration of MASS is absolute.

Careful measurement of the instrumental parameters used to calculate indices and WFs is needed to obtain accurate seeing data with MASS. Small deviations of the photon-counting statistics from the Poisson law are monitored by repeated detector tests and expressed through the non-poisson parameter. Potenital bias caused by the finite exposure time 1 ms is corrected in the software. The size of the apertures projected onto the telescope pupil must be determined by means of the optical magnification coefficient to a relative accuracy of $\pm 3\%$. The aperture geometry must not be altered by such effects as vignetting, non-uniform mirror coating or dust. Finally, the spectral response must be known with sufficient accuracy, although this is non-trivial. A method to check the response by photometry of standard stars of different colors has been recently developed. The color of the observed star also influences the spectral distribution of detected photons; it is taken into account by the MASS software.

Profile restoration in MASS is based on the weak-scintillation theory, while in reality the scintillation index s_A^2 in the smallest 2-cm aperture can sometimes exceed one. Numerical simulations have shown that the spatial spectrum of even moderately strong scintillation deviates from the standard theory and contains more power at high frequencies than expected. The result is an overestimation of the seeing by MASS – "over-shoots". Indeed, over-shoots have been systematically observed with MASS-DIMM when the seeing was dominated by high and strong turbulence.

Guided by numerical simulations, we have developed an empirical method to correct for over-shoots (Tokovinin & Kornilov 2007). It works only for moderately strong scintillation, $s_A^2 < 0.7$. Briefly, the measured indices are "translated" to their values that would correspond to the standard theory and then the usual method of profile restoration is applied. Figure 1 shows an example of MASS-DIMM data for a night where the FA seeing was strong. Yes, after proper processing, the GL seeing calculated from the difference appears relilable because it does not show the spikes originating in the high layers. Under stronger scintillation, the method does not work any longer.

Current version of the MASS software, *Turbina*, implements the new processing scheme and corrects for the over-shoots automatically. It also permits to re-process the extant MASS data. Thus, even if some instrumental parameters were not specified correctly, they can be re-measured before re-processing. Errors of various kinds can be corrected as well, e.g. a wrong setting of computer clock which entrained wrong air-mass calculation.

4. Accuracy of DIMM

It is commonly assumed that the DIMM method is very robust and "fool-proof", delivering correct seeing measurements as long as its unique calibration parameter, pixel scale, is determined. This is very far from reality.

Finite exposure time in a DIMM reduces the amplitude of the measured image motion and biases the seeing to lower values, sometimes significantly. Even with exposures as short as 5 ms some bias remains. Methods to correct this bias by taking interlaced exposures or binning the data have been developed (Tokovinin 2002).

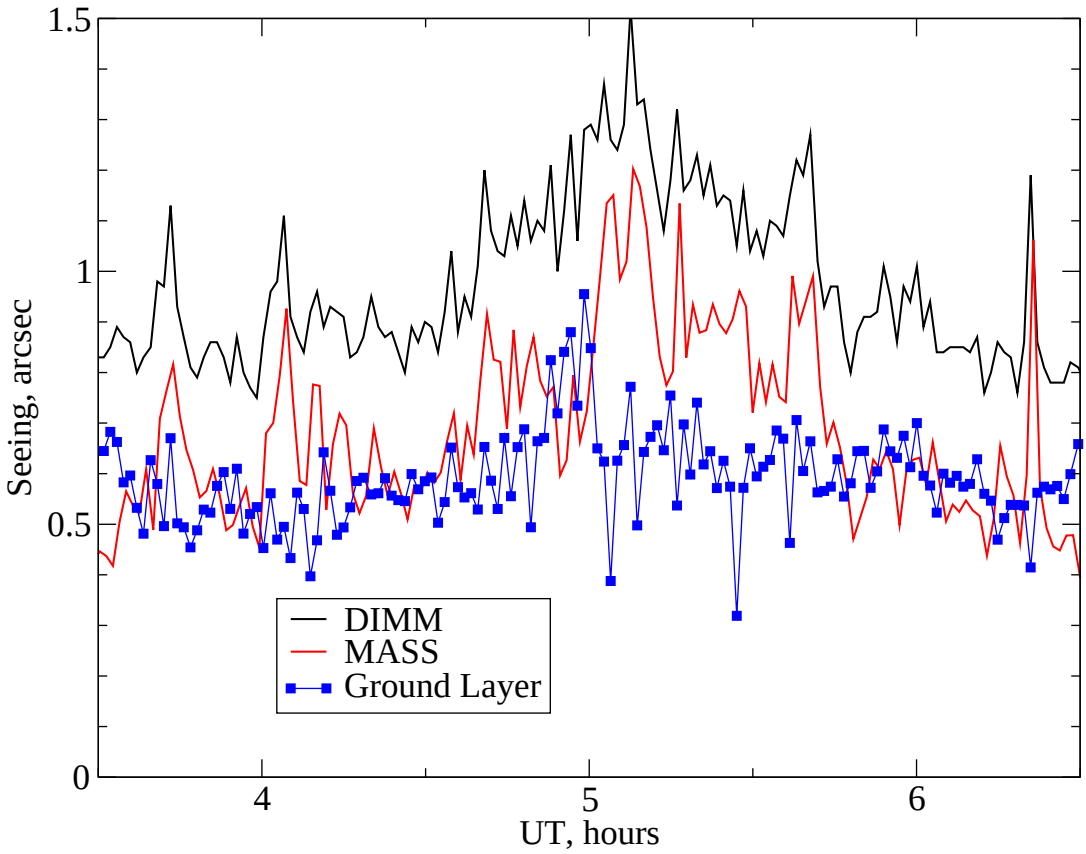

FIG. 1. Simultaneous measurements of the total seeing and free-atmosphere seeing with MASS-DIMM at Cerro Tololo on February 7/8, 2007. The GL seeing was calculated by subtracting the integrals. We see that the spikes of seeing in the upper atmosphere are not present in the GL seeing, hence the subtraction works.

The measured differential variance of angles σ^2 contains an additive contribution caused by the detector and photon noise. This noise term is usually, but not always, small. It depends on the parameters of centroid calculation, readout noise, and star brightness, so cannot be calculated once and for all. Most existing DIMM data-processing algorithms simply ignore the noise or subtract a fixed noise.

Additional noise could be created by the "jumps" of centroids due to finite pixels, under some conditions. Use of color CCDs in amateur DIMMs[2] is strongly discouraged because pixel filters in such CCD produce strong periodic errors.

The variance σ^2 is converted to the seeing by the equation

$$\sigma^2 = K\ (\lambda/D)^2\ (D/r_0)^{5/3}, \tag{1}$$

where the response coefficient K depends on the ratio of the baseline B to the apertures' diameter D and on the measurement direction, longitudinal or transverse (Tokovinin 2002). A more refined analysis shows that K also depends slightly on the method used to calculate the spot centroids.

[2]Web-cam DIMM of S. Cavadore at http://astrosurf.com/cavadore/seeing/monitor_DIMM/index.html

The theory of DIMM usually presumes that turbulence is located close to the pupil and produces pure phase distortions. In reality, both phase and amplitude of the light wave are affected. Propagation over a distance $z > D^2/\lambda$ (i.e. $z > 10\,\mathrm{km}$ for $D = 0.1\,\mathrm{m}$) reduces the response coefficient K, typically up to 10%.

A severe bias can be caused by a combination of small aberrations in a DIMM with propagation. Imagine a slightly defocused spot. Its centroid is still a good measure of the wave-front tilt for pure phase distortions. However, amplitude fluctuations at the pupil will also displace the center of the defocused spot, even without phase fluctuations. We expect that defocused (or, generally, aberrated) spots display additional difefrential motion caused by the scintillation and, as a result, DIMM would over-estimate the seeing. Both simulations and special experiments fully confirm this conclusion. Of course, this bias depends on the high-altitude turbulence. At a bad site where the strong ground layer dominates the seeing a defocused DIMM would still give reasonable results.

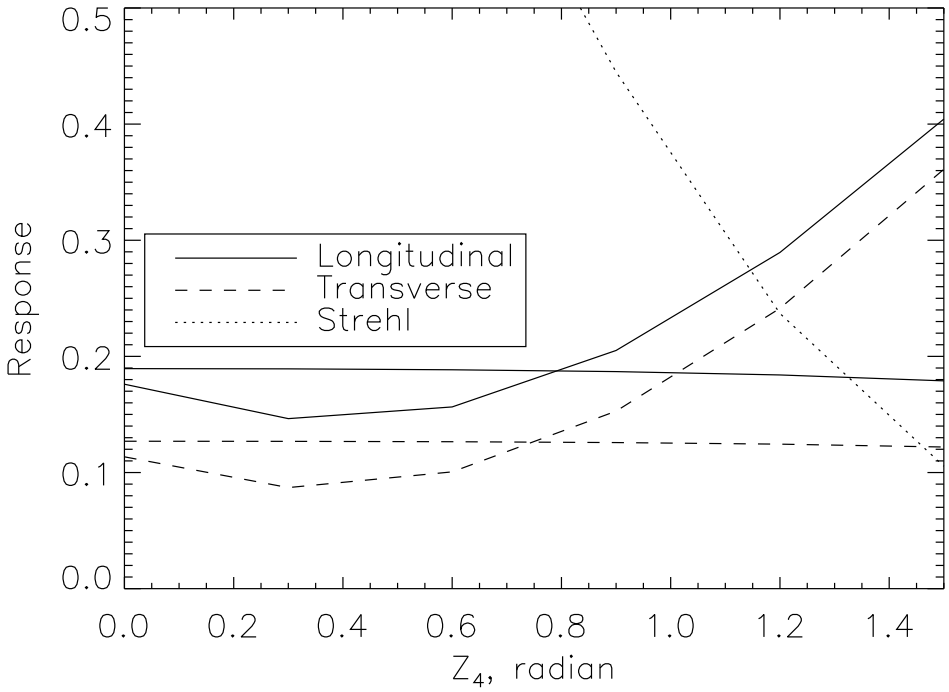

FIG. 2. Response coefficients K for the longitudinal (full lines) and transverse (dashed lines) differential image motion in a DIMM with $B = 0.25\,\mathrm{m}$, $D = 0.1\,\mathrm{m}$, as a function of spot defocus Z_4. Near-constant lines correspond to the turbulence at the ground, other lines – to a layer at 10 km. The dotted line shows the Strehl ratio.

We studied the bias in aberrated DIMM by both analytical method and numerical simulation. It turns out that for a small defocus the bias caused by propagation can be negative (K decreases by as much as 20%), but for a strong defocus or coma it is always positive, with K increasing up to a factor of 2 (Fig. 2). Positive bias can be avoided by careful control of the optical quality in a DIMM. To this end, Strehl ratio SR of each spot must be measured. Note that the measured Strehls depend on the colors of the stars because the spectral response of CCDs is usually broad. A criterion $SR \geq 0.6$ avoids the strong positive bias. However, the negative bias is largest for a rms defocus of only 0.3 radian, or $SR = 0.91$, which is very difficult to control.

Resuming, we see that potential biases in a DIMM are numerous and not always well controlled. They also depend on the atmospheric conditions such as the wind speed and the fraction of high-altitude turbulence. Thus, inter-comparison of two DIMM instruments can give concordant results under certain conditions (e.g. dominant ground layer), but it does not guarantee that they are free of biases and would measure the same seeing at some other good site. The agreement is a necessary, but not sufficient condition for getting accurate DIMM data. Careful control of all biases is essential.

5. Conclusions

Both MASS and DIMM can provide accurate measurements of r_0 with intrinsic bias of only few percent. However, to reach this goal, we need to measure and monitor carefully all essential instrument parameters and to control the data quality. The bias is a complex function of both instrument parameters and atmospheric conditions.

A new concept, not yet implemented in current site-testing practice, is *bias error budget* where we would quantify systematic offsets in r_0 caused by various factors and determine the overall bias. It appears that bias control to 1% is both unrealistic and unnecessary, because the seeing itself cannot be defined reasonably with such a high accuracy.

Agreement between two site-testing instruments working on the same site is a necessary, but not sufficient condition for getting un-biased data. These same instruments can diverge at another site or on another night. Traditional practice of inter-calibrating site-testing equipment is useful for un-covering problems and should be pursued, but only measurements of r_0 on the absolute scale can serve for a reliable site comparison.

References

Kornilov, V., Tokovinin, A., Voziakova, O. et al., 2003, Proc. SPIE, 4839, 837

Roddier, F. 1981, Progress in Optics, 19, 281

Sarazin, M., & Roddier, F. 1990, Astron. & Astrophys., 227, 294

Tokovinin, A. 2002, PASP, 114, 1156

Tokovinin, A., Kornilov, V., Shatsky, N., Voziakova, O., 2003, MNRAS, 2003, 343, 891

Tokovinin, A. & Travouillon, T., 2006, MNRAS, 365, 1235

Tokovinin, A. & Kornilov, V. 2007, MNRAS, in preparation

The fast defocus monitor, FADE – an instrument to measure the atmospheric coherence time.

Aglaé Kellerer*
European Southern Observatory, Garching bei München, Germany

Andrei Tokovinin
Cerro Tololo Inter-American Observatory, La Serena, Chile

ABSTRACT

In the context of site selection for future generations of telescopes, the coherence time is a particularly important parameter that determines the sensitivity of interferometers and the performance of adaptive-optics devices. But there is currently no suitable, simple technique to measure the coherence time: either the instrument is not well suited for site monitoring, or the method is burdened by intrinsic uncertainties and biases. Site testing and monitoring campaigns rely, therefore, predominantly on the assessment of the seeing.

To close the current gap, we suggest a method to measure the coherence time with a small telescope.

* *Corresponding author address:* Aglaé Kellerer, European Southern Observatory, Karl-Schwarzschildstr. 2, 85748 Garching bei München, Germany
E-mail: aglae.kellerer@eso.org

1. Introduction

The number of photons available for wave-front sensing in adaptive optic (AO) systems or for fringe tracking with an interferometer is directly proportional to the exposure time, which, in turn, is conditioned by the *atmospheric coherence time*, τ_0. Monitoring this parameter, together with the *seeing*, ε_0, and *isoplanatic angle*, θ_0, is thus essential for supporting high angular-resolution observations. It is also a major issue of the site-selection campaigns for next generations of large single-dish telescopes and interferometers. However, there is currently, no fully adequate technique to measure the coherence time. To fill this gap, we propose a new instrument termed *Fast Defocus monitor*, FADE.

2. Current methods of τ_0 measurement

Several instruments can measure the atmospheric coherence time, τ_0, or related parameters. Methods in the first group work well, but are not suitable for site monitoring:

- SCIDAR (SCIntillation Detection And Ranging) has provided good results on τ_0, but it requires large telescopes and manual data processing (Fuchs et al. (1998)).
- Balloons are expensive and provide only single-shot profiles of low statistical significance (Azouit and Vernin (2005)).
- AO systems and interferometers give good results, but are suitable neither for testing projected sites nor for long-term monitoring (Fusco et al. (2004)).

The following methods all use small telescopes and can thus be employed for site-testing. They all have their special attractions. However, with regard to the coherence time, each technique has its intrinsic problems:

- SSS (Single Star SCIDAR) in essence extends the SCIDAR technique to small telescopes: profiles of $C_\mathrm{n}(h)^2$ and $V(h)$ are obtained with less altitude resolution than with SCIDAR, and are then used to derive the coherence time (Habib et al. (2006)).
- The GSM (Generalized Seeing Monitor) can measure velocities of prominent atmospheric layers (Ziad et al. (2000)). By refined data processing, a correlation time τ_{AA} is deduced from the angle-of-arrival fluctuations, but this parameter is not directly related to τ_0.
- MASS (Multi-Aperture Scintillation Sensor) is a recent, but already well proven turbulence monitor (Kornilov et al. (2003)). One of its observables, related to scintillation in a 2 cm aperture, approximates the coherence time, but it is insensitive to the low-altitude layers and gives, thus, a biased estimate of τ_0.
- DIMM (Differential Image Motion Monitor) cannot determine τ_0, but an estimation of the coherence time is nevertheless obtained by combining the measured seeing with meteorological wind speed data (Sarazin and Tokovinin (2002)).

We conclude from this brief survey that there is, at this point, no sufficiently simple technique to measure τ_0 with a small telescope.

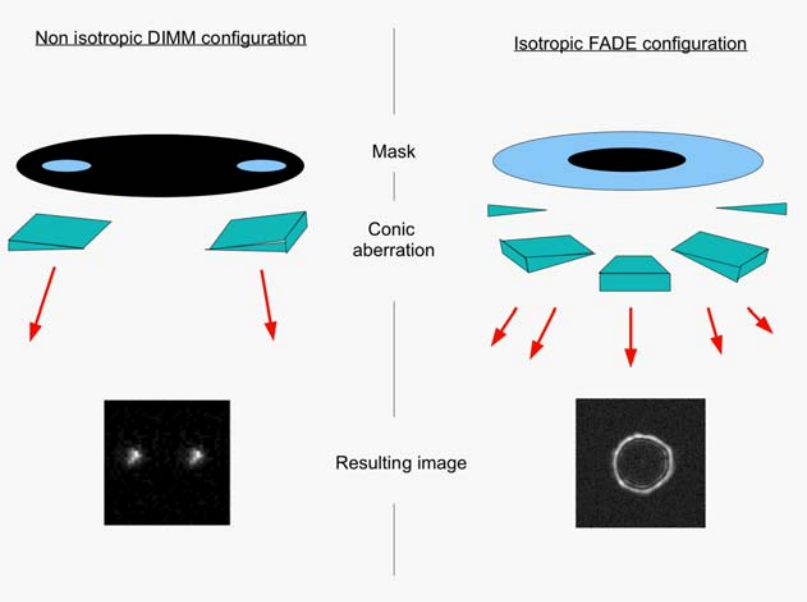

FIG. 1. FADE might be seen as an isotropic descendant of DIMM.

3. A new site monitoring instrument, FADE

We have, therefore, recently proposed such a method (Kellerer and Tokovinin (2007)). The image of a star is shifted somewhat out of focus, which converts it – due to an enlarged central blind area of the telescope – into an annulus. Insertion of a lens with suitable spherical aberration sharpens this wide annulus into a narrow ring. The combination of defocus and spherical terms is chosen to approximate a conic aberration. The radius of the ring is related to the defocus and thus serves to measure turbulence-induced focus fluctuations. As illustrated on Figure 1, FADE is an extension of the DIMM method to a full annular aperture.

The strength of the approach is its insensitivity to *tip* and *tilt*, which – being jointly caused by telescope vibrations and atmospheric turbulence – are not meaningful indicators of turbulence alone. Instead, it measures the aberration of next higher order *defocus*. A relation between the temporal variations of the radius and the coherence time has been developed in the framework of Kolmogorov's theory of turbulence.

First measurements with FADE were obtained at Cerro Tololo, Chile, from October 29th to November 2nd 2006. As indicated on Figure 2, the instrument incorporates a *Celestron* telescope with mirror diameter 35 cm and a fast CCD detector from *Prosilica*: sub-regions of 100×100 pixels can be read out at frame rates up to 740 Hz. Ring images were recorded during five nights, with short exposure-times between 0.2 ms and 2 ms, and over a broad range of instrument settings.

4. First observations

The measurements and their uncertainties have been analyzed and compared to simulated images. In particular, telescope aberrations blur the ring image. The rings also contain bright *scintillation* spots due to high-altitude turbulence. These effects can alter the radius estimates, and badly focused images – with ring-widths larger than 1.5 times the diffraction width – were therefore disregarded in the data analysis.

The seeing and coherence times derived from FADE are compared to simultaneous measurements by the DIMM and MASS instruments. At Cerro Tololo, the combined MASS-DIMM is installed at the focus of a 25-cm telescope, placed on a 6 m high tower, at 10 m distance from the dome where FADE was mounted. FADE and MASS-DIMM observed different stars and, thus, sampled different atmospheric volumes. The measurements are therefore not expected to coincide, still, the results should match statistically and follow similar trends.

Figure 3 compares the estimates of τ_0 and ε_0 obtained with FADE from October $29^{\rm th}$ to November $2^{\rm nd}$, to the results of MASS-DIMM. MASS is not sensitive to turbulent layers below $\sim 500\,$m altitude. This bias has here been corrected by adding, to the τ_0 estimates from MASS, a low-layer contribution evaluated with DIMM. However, this combined τ_0 estimate from MASS-DIMM has never been checked against other estimates, and cannot serve as a reference.

We note that the seeing values are better correlated than the coherence times. Statistically, it appears that FADE slightly under-estimates the seeing. This effect is reproduced with simulations of high-altitude turbulence and blurred ring images. In this case, FADE also under-estimates the coherence time. The bias on τ_0 can however not be ascertained by Figure 3 because the τ_0 estimates by MASS might likewise be biased.

5. Conclusion

A fuller account of our experiments will be submitted to the journal *Astronomy & Astrophysics* in June 2007 (Tokovinin et al. (2007)). As a next step, it is planned to assess the validity of the coherence time derived from FADE through simultaneous observations with an adaptive-optics system or an interferometer. The final aim is to use FADE for site monitoring and site testing campaigns. A particularly challenging and interesting project will be to monitor the coherence time at Dome C in Antarctica, which is a potential site for the next generation of telescopes and interferometers.

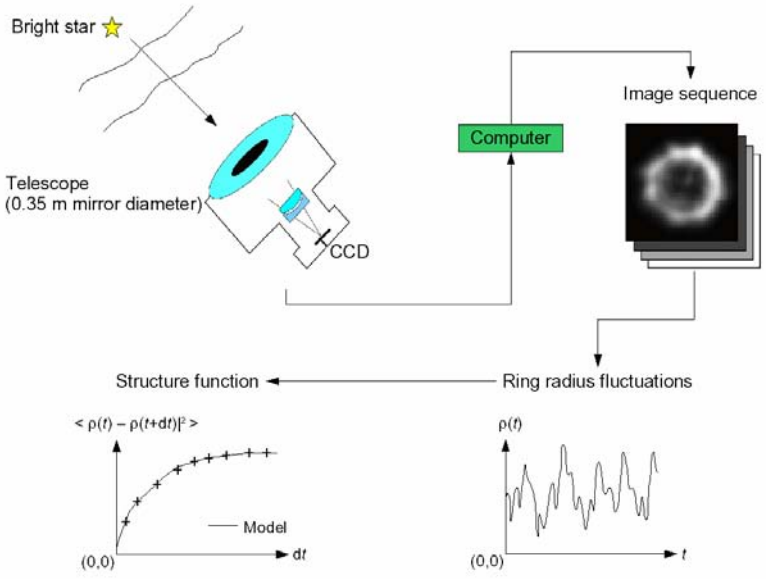

FIG. 2. Overview of the FADE instrument and data analysis.

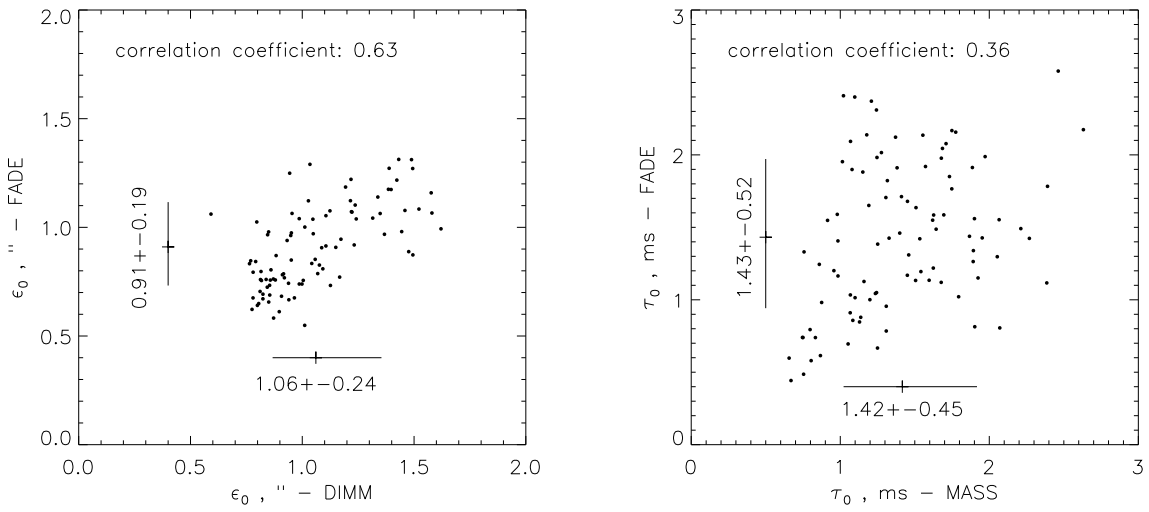

FIG. 3. Seeing and coherence time measured with FADE between October 29th and November 2nd, compared to simultaneous measurements by the MASS-DIMM. The average values and standard deviations of the parameters are indicated.

Acknowledgments.

It is a pleasure to thank Vincent Coudé du Foresto and Marc Sarazin for helpful discussions. The authors are grateful to Cerro Tololo observatory for its hospitality and support during the first mission, and acknowledge financial support from the European Southern Observatory.

References

Azouit, M. and J. Vernin, 2005: Optical Turbulence Profiling with Balloons Relevant to Astronomy and Atmospheric Physics. *PASP*, **117**, 536–543, doi:10.1086/429785.

Fuchs, A., M. Tallon, and J. Vernin, 1998: Focusing on a Turbulent Layer: Principle of the "Generalized SCIDAR". *PASP*, **110**, 86–91.

Fusco, T., N. Ageorges, G. Rousset, D. Rabaud, E. Gendron, D. Mouillet, F. Lacombe, G. Zins, J. Charton, C. Lidman, and N. N. Hubin, 2004: NAOS performance characterization and turbulence parameters estimation using closed-loop data. *Advancements in Adaptive Optics. Edited by Domenico B. Calia, Brent L. Ellerbroek, and Roberto Ragazzoni. Proceedings of the SPIE, Volume 5490, pp. 118-129 (2004).*, Bonaccini Calia, D., B. L. Ellerbroek, and R. Ragazzoni, Eds., Presented at the Society of Photo-Optical Instrumentation Engineers (SPIE) Conference, Vol. 5490, 118–129, doi:10.1117/12.563009.

Habib, A., J. Vernin, Z. Benkhaldoun, and H. Lanteri, 2006: Single star scidar: atmospheric parameters profiling using the simulated annealing algorithm. *MNRAS*, **368**, 1456–1462, doi:10.1111/j.1365-2966.2006.10235.x.

Kellerer, A. and A. Tokovinin, 2007: Atmospheric coherence times in interferometry: definition and measurement. *A&A*, **461**, 775–781, doi:10.1051/0004-6361:20065788, arXiv:astro-ph/0610207.

Kornilov, V., A. A. Tokovinin, O. Vozyakova, A. Zaitsev, N. Shatsky, S. F. Potanin, and M. S. Sarazin, 2003: MASS: a monitor of the vertical turbulence distribution. *Adaptive Optical System Technologies II. Edited by Wizinowich, Peter L.; Bonaccini, Domenico. Proceedings of the SPIE, Volume 4839, pp. 837-845 (2003).*, Wizinowich, P. L. and D. Bonaccini, Eds., Presented at the Society of Photo-Optical Instrumentation Engineers (SPIE) Conference, Vol. 4839, 837–845.

Sarazin, M. and A. Tokovinin, 2002: The Statistics of Isoplanatic Angle and Adaptive Optics Time Constant derived from DIMM Data. *Beyond conventional adaptive optics : a conference devoted to the development of adaptive optics for extremely large telescopes. Proceedings of the Topical Meeting held May 7-10, 2001, Venice, Italy. Edited by E. Vernet, R. Ragazzoni, S. Esposito, and N. Hubin. Garching, Germany: European Southern Observatory, 2002 ESO Conference and Workshop Proceedings, Vol. 58, ISBN 3923524617, p. 321*, Vernet, E., R. Ragazzoni, S. Esposito, and N. Hubin, Eds., 321–+.

Tokovinin, A., A. Kellerer, and V. Coudé du Foresto, 2007: Fade – an instrument to measure the atmospheric coherence time, to be submitted to A&A.

Ziad, A., R. Conan, A. Tokovinin, F. Martin, and J. Borgnino, 2000: From the Grating Scale Monitor to the Generalized Seeing Monitor. *AO*, **39**, 5415–5425.

Unresolved Critical Issues of Optical Turbulence That Affect Seeing Determinations

Frank D. Eaton*
Air Force Research Laboratory, Directed Energy Directorate, Kirtland AFB, NM

ABSTRACT

To date, modeling and simulation of laser beam propagation through atmospheric turbulence have relied upon a traditional theoretical basis that assumes the existence of homogeneous, isotropic, stationary, and Kolmogorov turbulence. Methodology is presented to determine the real impact of the refractive index structure parameter (C_n^2) on laser beam propagation including effects of non-classical turbulence as well as inner (l_0) and outer scale (L_0) effects. The variability of C_n^2 and l_0 on determining turbulence parameters over long paths is also discussed. Observations also clearly show turbulence is often layered and is produced by wave activity and episodic events such as Kelvin-Helmholtz instabilities. Other critical turbulence issues involve the relationship between mechanical and optical turbulence and the "volume filling" of radar. Planned observations addressing these issues will be obtained from three systems: a) an instrumented aircraft, b) a new measurement platform using a free-flying balloon that lifts a ring with a boom upon which are mounted fine wire (1-μm diameter) sensors to measure high-speed temperature and velocity fluctuations, and c) a 50 MHz radar at Vandenberg Air Force Base that senses at high temporal and spatial resolution to 20 km ASL. These systems provide estimates of C_n^2, eddy dissipation rate (ε), l_0, and L_0.

**Corresponding author address:* Frank Eaton, AFRL/DESA, 3550 Aberdeen Ave. SE, Kirtland AFB, NM 87117-5776

1. Introduction

Turbulence measurements to support laser propagation efforts have primarily been taken over integrated paths of interest to obtain the refractive index structure parameter (C_n^2), the Rytov variance (σ_R^2), the transverse coherence length (r_o), and the isoplanatic angle (θ_o) using appropriate optical sensors. Local determinations of C_n^2, the inner scale (l_o), and the outer scale (L_o) have been found using radar, sodar, and fine wire sensors. Preliminary results show that the assumptions of "classical theory" are frequently violated. The path variability of C_n^2, l_o, and L_o have also not been properly assessed regarding determining C_n^2 and σ_R^2 using scintillometers for beam propagation issues, particularly over long paths. Actual observations and evaluation of these turbulent characteristics coupled with beam calculations are required to evaluate the true effects of a real atmosphere on propagation.

Probably the systems that have led to the greatest understanding of the physics of atmospheric turbulence and related turbulence issues are radar systems. A nearly six-year continuous data set observed with a 50-MHz radar at White Sands Missile Range (WSMR) was used to examine slant path optical turbulence conditions (transverse coherence length, isoplanatic angle, and Rytov variance), (Eaton et al., 1999), examine persistent layers of enhanced C_n^2 in the lower stratosphere, (Nastrom and Eaton, 2001), estimate the inner and outer scales of turbulence (Eaton and Nastrom, 1998), study gravity waves and turbulence near thunderstorms, (Hansen et al., 2002), investigate the seasonal variation of gravity wave activity at WSMR, (Hansen et al., 2001), and study the coupling of gravity waves and turbulence (Nastrom and Eaton, 1993). Other MST radar studies relevant to this paper include examining the winds and turbulence at WSMR, (Nastrom and Eaton, 1995) estimating the eddy dissipation rates, (Nastrom and Eaton, 1997a), estimating diffusion coefficients, (Nastrom and Eaton, 1997b) examining the turbulent effects during the passage of a cyclone, (Nastrom and Eaton, 2003) and examining quasi-monochromatic inertia-gravity waves in the lower stratosphere (Nastrom and Eaton, 2006). A FMCW radar has ultra sensitivity for sensing turbulence in the planetary boundary layer and senses at high resolution (~2-m range and 12 s for obtaining each profile) (Eaton, et al., 1995).

Other Air Force Research Laboratory turbulence measurement programs included aircraft and scintillometer observations (Hahn et al., 1999), combined aircraft and radar observations (Eaton et al., 1998), turbulence measurements using a kite and tethered blimp platform (Eaton et al., 2000), and measurements in complex terrain using an ensemble of sensors (scintillometer, differential image motion monitor, sodar, and tower-mounted fine wire sensors) (Eaton et al., 2000). Similar fine wire probe systems were used on the aircraft, kite/tethered blimp experiments, and on the tower. This design was modified for the fine wire systems as described later in this paper for the balloon-ring platform.

2. Dominant Critical Issues

Actual measurements to examine if assumptions of "classical" turbulent conditions are violated are necessary. The measured results then should be used in beam calculations and compared to beam calculations assuming the "classical" conditions. A practical approach involves using the Mutual Coherence Function since this is convenient to vary parameters of interest. For example, different spectra can be used and ultimately results can be easily compared. Three spectra of interest are the Kolmogorov spectrum that assumes there are zero inner scales and infinite outer scales of turbulence, the von Karman spectrum that accounts for both scales, and the Andrews spectrum that additionally allows for incorporating the actual shape of the inner scale. VanZandt et al. (1978) addressed the problem regarding radar observations concerning C_n^2 and ε and they presented the relationship:

$$\varepsilon = \left(\gamma \overline{C}_n^2 \frac{N^2}{F^{1/3}} M^{-2} \right)^{3/2} \qquad (1)$$

Where γ. is a "constant," $\overline{C}_n^2$ is the mean refractive index structure parameter for the radar volume, N is the Brunt Vaisala frequency $\left[N^2 = g\left(\partial \ln\theta / \partial z\right) \right]$ where z is the height and θ is the potential temperature, F represents the fraction of the radar volume which is filled by turbulence, and M is the gradient of the generalized potential index.

3. Methodology and Instrumentation

Turbulence measurements to examine the stated critical issues will be taken using fine wire probes mounted on a balloon-ring platform, a tethered blimp/ kite platform, an instrumented aircraft, a 50 MHz radar, and various optical sensors. Both temperature and velocity data are measured on the balloon-ring platform with fine wire probes at various separations on a boom. The data are received by telemetry at the ground at the sampling rate (typically 3.0 kHz). The results of calculations of PSDs and structure functions for the observations of each probe will display if certain atmospheric conditions produce non-Kolmogorov turbulence.

The instrumented balloon-ring platform will be flown next to the 50 MHz radar located at Vandenberg AFB to provide simultaneous measurements of C_n^2, ε, winds, etc. These high spatial resolution observations will be compared to the same radar-obtained values within the radar scattering volume to examine radar scattering mechanisms as well as evaluating "F" in equation 1.

A Mooney aircraft has been instrumented with the same fine wire systems as are used on the balloon-ring platform system. Plans are to fly between Salinas Peak and North Oscura Peak (a 52.4 km path) collecting high-data-rate observations of temperature and velocity. These results will allow calculations of C_n^2, l_o, L_o, and ε at high resolution along the path. Several optical systems will be operated simultaneously between the two mountain peaks including a scintillometer, a pupil plane imager, an open loop wave front sensor, a transverse coherence length device, and a path profiler.

Simulations will be used to evaluate the effect of the path variability on the optical measurements.

Balloon wakes that contaminate measurements taken from sensors behind an ascending balloon have been documented by Tiefenau and Gebbeken (1989) and by constant-level balloons (Reynolds and Lamberth, 1966). A new platform was designed to examine balloon wake effects using a large "ring" so that sensors mounted facing upwards on the ring will be uncontaminated by the balloon wake. The "ring" is an inflatable polyethylene tube with a pressure relief valve. The "ring" is actually 8-sided with a diameter of about 30 feet and trails the balloon using several risers. The balloon wake passes through the center of the "ring" leaving the measurements uncontaminated. This system will be used at Holloman AFB and Vandenberg AFB with several tungsten fine wire (1-μm diameter) sensors to measure high-speed temperature and velocity fluctuations. These sensors are mounted on a 3m long boom with positions of 0m, 0.25m, 1.0m, 1.5m, and 3.0m. The associated electronics have automatic gain controls to allow measurements to be taken over a broad range of turbulent conditions. All channels are fed into a controller board that sends the information to a transmitter. The total instrumentation package including sensors, associated electronics, controller board, transmitter, and antenna weighs only a few pounds, allowing the overall system to fall within the same flight regulations as a conventional radiosonde. Data will be received by telemetry and a GPS unit on the package will aid in recovery. Very accurate calibrations are required to obtain data that can be used to calculate spatial differences of turbulence. The complete system is calibrated in a chamber covering the complete range of temperature anticipated. The rate of change in temperature is simulated in the chamber to agree with the rate of temperature change of the ascending balloon.

The 50 MHz radar is located at Vandenberg AFB. It has fixed coaxial-collinear antennas at right angles. Beams are directed 15^0 from the zenith at 45^0 and 135^0 azimuth, and one is vertical, permitting the three components of the wind vector to be resolved. The antenna is about 150m in diameter and produces a one-way beam width of 2.9^0. Received power, from which C_n^2, wind speed, and spectral width are derived, is observed for 1 min along each beam. Since the three different beams are sampled consecutively, a full profile is obtained every three minutes. Pulse coding applied to the 8-μs transmitted produces 1-μs nominal pulse lengths to give 150-m resolution along each beam axis. In normal operation, 112 range gates are used to sample from 3.22 -20 km in altitude. The transmitted power of 250 kW leads to a power aperture product of 1×10^8 W m^2.

The North Oscura Peak to Salinas Peak path is on White Sands Missile Range, NM. This is located above the Tularosa Basin-a desert basin bounded on both the eastern and western sides by mountain ranges. Vandenberg AFB is located on the coast of southern California. Therefore the conditions are of a typical littoral zone with a marine boundary layer.

4. Summary

This paper presents new methodology to examine several critical issues of optical turbulence. One is to evaluate the impact of real atmospheric turbulent conditions on laser beams by considering the non-classical effects of turbulence. High-resolution

measurements will be used and incorporated into theoretical beam calculations. Other specific objectives are to examine the relationship between mechanical turbulence and optical turbulence (since this is of interest for some modeling approaches), to investigate radar scattering mechanisms including the "filling factor" problem, to examine the effect of variable C_n^2 and l_o on extracting turbulent parameters over long paths, and to study the turbulent characteristics of both the desert environment and the marine boundary layer with associated littoral zone. From simultaneous VHF radar and balloon-ring system observations, the refractive index structure parameter (C_n^2), the eddy dissipation rate (e), the inner scale (l_o), and the outer scale (L_o) will be evaluated.

Acknowledgments.
Special appreciation is extended to Don Black for their help in fabricating the electronics and calibrating the equipment.

References

Eaton, F. D., S. A. McLaughlin, and J. R. Hines, 1995: A new frequency-modulated continuous wave radar for studying planetary boundary morphology, *Radio Science,* Vol 30, No. 1, pp. 75-88.

Eaton, F. D., G. D. Nastrom, B. Masson, I. L. Hahn, K. A. McCrae, S. R. Nowlin, and T. Berkopec, 1998: Radar and aircraft observations of a layer of strong refractivity turbulence, Proceedings of the SPIE, **3381,** AeroSense Airborne Laser Advance Technology, Orlando, FL.

Eaton, F. D., G. D. Nastrom, and A. R. Hansen, 1999: Middle atmosphere slant-path optical turbulence conditions derived from VHF radar observations, *Optical Engineering,* **38**, No. 2, 200-207.

Eaton F. D. and G. D. Nastrom, 1998: Preliminary estimates of the inner and outer scales from White Sands Missile Range, NM radar observations, *Radio Science*, **33**, No. 4, 895-903.

Eaton, F. D., B. B. Balsley, R. D. Frehlich, R. J. Hugo, M. Jensen, and K. A. McCrae, 2000: Turbulence observations over a desert basin using a kite/tethered-blimp platform, *Optical Engineering,* **39,** 2517-2526.

Eaton, F. D., W. P. Brown, S. D. Ford, J. E. Miller, S. D. Stokes, and V. M. Stone, 2001: Intercomparisons of turbulence observations in a mountain-valley system, Proc. of the SPIE, 4376, 134-140.

Hahn, I. L., B. P. Venet, F. D. Eaton, R. J. Hugo, and S. R. Nowlin, 1999: Refractive index structure parameter in the boundary layer as measured from an aircraft and a ground based scintillometer, *American Meteorological Society Paper 3B.2,* 13th Symposium on Boundary Layers and Turbulence, 79th Annual Meeting, Dallas, Texas.

Hansen, A. R. , G. D. Nastrom, J. A. Otkin, and F. D. Eaton, 2002: MST radar observation of gravity waves and turbulence near thunderstorms, *Journal of Applied Meteorology,* **41**, pp. 298-305.

Hansen, A. R. , G. D. Nastrom, and F. D. Eaton, 2001:Seasonal variation of gravity wave activity at 5-20 km observed with the VHF radar at White Sands Missile Range, New Mexico, *Journal of Geophysical Research,* **106**, No D15, 17,171-17,183.

Nastrom G. D., and F. D. Eaton, 1993: The coupling of gravity waves and turbulence at White Sands, New Mexico, from VHF radar observations, *Journal of Applied Meteorology,* **32**, No. 1, 81-87.

Nastrom G. D., and F. D. Eaton, 1995: Variations of winds and turbulence seen by the 50-MHz radar at White Sands Missile Range, New Mexico, *Journal of Applied Meteorology,* **34**, No. 10, 2135-2138.

Nastrom G. D., and F. D. Eaton, 1997a: Turbulence eddy dissipation rates from radar observations at 5-20 km at White Sands Missile Range, NM, *Journal of Geophysical Research,* **102**, No. D16, 19,495-19,505,.

Nastrom G. D. and F. D. Eaton, 1997b: A brief climatology of eddy diffusivities over White Sands Missile Range, New Mexico, *Journal of Geophysical Research-Atmospheres,* **102**, No. D25, 29,819-29,828.

Nastrom G. D., and F. D. Eaton, 2001:Persistent layers of enhanced C_n^2 in the lower stratosphere from VHF radar observations, *Radio Science,* **36**, No. 1, 137-139.

Nastrom G. D., and F. D. Eaton, 2003: A case study of atmospheric conditions at 4-19 km over Vandenberg AFB during passage of a cyclone, *Journal of Applied Meteorology,* **42**, No. 4, pp. 467-475.

Nastrom, G. D., and F. D. Eaton, 2006: Quasi-monochromatic inertia-gravity waves in the lower stratosphere from MST radar observations, *Journal of Geophysical Research,* Vol III, doi:10:1029. 2.

Reynolds, R. D., and R. L. Lamberth, 1966: Ambient temperature measurements from radiosondes flown on constant-level balloons, *J. Appl. Meteorol.,* **5,** 304-307.

Tiefenau, H. E. and A. Gebbeken, 1989: Influence of meteorological balloons on temperature measurements with radiosondes: nighttime cooling and daytime heating, *J. Atmos. and Oceanic Tech.,* **6,**36-4

Van Zandt, T. E., J. L. Green, K. S. Gage, and W. L. Clark, 1978: Vertical profiles of refractivity turbulence structure constant: Comparisons of observations by the Sunset radar with a new theoretical model, *Radio Science,* **13,**818-829.

The seeing monitors: Instrumental noise and cross-calibration

Zouhair Benkhaldoun*
Laboratoire de Physique des Hautes Energies et Astrophysique
Cadi Ayyad University Marrakech

ABSTRACT

These last years, several seeing monitors (DIMM) have been built almost everywhere, with a material that was intended to serve only amateurs of astronomy. In order to make a campaign of site testing in Morocco, we have built our own DIMM in Marrakech University. To make our instrumentation reliable, we wanted on the one hand to measure the instrumental noise and the influences of defocusing on the values of the seeing; and on the other hand to make cross-calibration of several instruments while using various diameter tubes (C8 and C11), various cameras and also from different mountings. We are presenting in this communication the results of these various tests.

*Corresponding author address: Zouhair Benkhaldoun, LPHEA, Cadi Ayyad University Marrakech.
E-mail: zouhair@ucam.ac.ma

Characterizing the TMT site selection equipment

Matthias Schoeck*
Thirty Meter Telescope

The TMT site selection team

ABSTRACT

The Thirty Meter Telescope (TMT) is currently acquiring site characterization data at five candidate sites. The site testing equipment includes several instruments for measuring the seeing and seeing profiles, in particular, Differential Image Motion Monitors (DIMM), Multi-Aperture Scintillation Sensors (MASS) and two different models of Sound Detection and Ranging (SODAR) units. All site testing equipment and data have gone through extensive calibrations and verifications in order to assure that a reliable and quantitative comparison between the candidate sites will be possible. Here, we summarize the equipment characterization efforts and the resulting accuracies of our site selection data.

*Corresponding author address: Matthias Schoeck, Thirty Meter Telescope.
E-mail: mschoeck@tmt.org

The Thirty Meter Telescope DIMM systems

Warren Skidmore*
Thirty Meter Telescope

Lianqi Wang
University of California, Irvine

Matthias Schoeck
Thirty Meter Telescope

Gary Chanan
University of California, Irvine

Edison Bustos, Juan Seguel and Robert Blum
Cerro Tololo Inter-American Observatory

ABSTRACT

I describe the TMT DIMM systems, concentrating on the high speed drift mode of observations, data reduction methods and our DIMM system cross comparison campaign. I show that with correct optical alignment of the telescopes and DIMM optics we can characterize the seeing to better than ±0.02 arc seconds. Requirements of any DIMM system used for acquiring high quality DIMM measurements are listed.

*_Corresponding author address:_ Warren Skidmore, Thirty Meter Telescope.
E-mail: was@tmt.org.

The TMT MASS System: Characterization and Application

Sebastian Els*
AURA-NIO, La Serena, Chile

TMT Site Testing Team

ABSTRACT

The Thirty Meter Telescope site testing campaign uses a combined MASS-DIMM device for turbulence monitoring. In order to investigate the reliability of the MASS device, we have conducted numerous tests on the impact of the various instrument parameters on the turbulence data produced by the MASS. These tests and their results will be presented, as well as the results of a side by side comparison of two MASS devices, demonstrating the precision of the MASS system. Finally, some MASS data from the TMT site testing network in northern Chile will be presented in view of the possibility of seeing forecasting.

*Corresponding author address: Sebastian Els, AURA-NIO, La Serena, Chile.
E-mail: sels@ctio.noao.edu.

An Optical Turbulence Profiler for the terrestrial atmosphere boundary-layer

Julien Borgnino*, Amokrane Berdja, Aziz Ziad and Jerôme Maire
Laboratoire Universitaire d'Astrophysique de Nice
Université de Nice Sophia Antipolis

ABSTRACT

The statistical analysis of the angle-of-arrival (AA) fluctuations appears to be well adapted to monitor the optical effects induced by atmospheric turbulence on the images observed using ground-based telescopes. Observing stars, it is widely used in the case of nighttime observations. In daytime, these fluctuations may be observed on solar limb images at the telescope focus but also in the pupil plane using a technique identical to a Foucault test. In this last case, the telescope pupil is observed through a diaphragm (slit) with a width of a few seconds of arc placed on the image of the solar limb. The AA fluctuations, considered according to the perpendicular to the solar limb, are thus transformed in intensity fluctuations. This is done at a first order approximation. A precise calibration must be performed. One can note here that this method is equivalent to the use of a Shack-Hartmann sensor, but with another spatial resolution. A special attention must be paid to the spatial and angular filtering associated with the use of the diaphragm on the solar limb. For the processing of the measurements this filtering will be taken into account. One can note that for nighttime experiments, the technique is the same observing the lunar limb. Some elements of discussion will be presented concerning the specificities of the use of the Sun or of the Moon like source.

The principle is described and the theory briefly summarized and illustrated by numerical simulations. This work leads to the presentation of a profiler allowing to quantify and localize with a high altitude resolution the optical turbulence which degrades astronomical images.

At first, the observation of the intensity fluctuations (recorded using a CCD camera) in the image of the pupil through the diaphragm, therefore the AA fluctuations, makes easy the estimate of the wavefront spatial coherence parameters. For estimating the Fried

parameter r_0, the method is differential, like in the Differential Image Motion Monitor (D.I.M.M.) widely used to estimate the quality of astronomical images. The measurements of the structure functions corresponding to baselines between two sub-apertures parallel and perpendicular to the solar (lunar) edge allow to deduce estimates of r_0.

The spatial coherence outer scale L0 may also be estimated using a distribution of sub-apertures on the pupil image analog to the one of the experiment G.S.M.(Generalized Seeing Monitor)which has allowed the evaluation of the major astronomical sites around the world. To have the same baselines that those of the standard G.S.M., it is necessary that the telescope diameter be at least equal to 1.5m. For smaller telescopes, another way could be the use of diaphragms of different sizes. This technique has been used in the past and the method has appeared notably robust.

Then, in order to obtain estimations of vertical profiles (of energy or turbulence outer scale) one can use a triangulation method observing two images of the telescope pupil through two diaphragms positioned at some angular distance on the solar (lunar) limb image. This experiment is identical to a SLODAR, the AA fluctuations being observed in the pupil image simultaneously for two angular directions in the sky, directions which can be easily selected like their angular separation. The possibility to choose this separation allows to hope, via a cross-correlation technique, a high vertical resolution. One can also consider that the AA fluctuations may be observed simultaneously for more than two directions in the sky (multiple objects for the SLODAR). For example, using 4 slits in non-redundant positions on the solar (lunar) limb images could lead simultaneously to 6 angular separations.

This study of the potentialities of the observation of the AA fluctuations in images of the telescope pupil using a technique identical to a Foucault test is done here in the context of the implementation of two other experiments.

The first one, is the Generalized Solar Seeing Monitor (M.I.Sol.F.A: Moniteur d'Images Solaires Franco-Algérien) which will be used for the comparison (in 2008) between solar diameter measurements performed from ground and space (PICARD mission (CNES)). It is based on simultaneous observations in the image and pupil planes of the AA fluctuations which leads, in the framework of a turbulence model, to the estimation of the

coherence parameters characterizing the wavefronts. The optical turbulence profiles C_n^2(h)will be also deduced. The objective is the modeling of the optical effects of atmospheric turbulence on ground measurements.

The other one is the Monitor for Outer Scale Profile (M.O.S.P), which allows the estimate of the angular correlation of the AA fluctuations deduced from Moon's limb observations. The outer scale profiles L_0(h) are generally estimated with given C_n^2(h) profiles measured simultaneously with a SCIDAR.

Results have been recently obtained during two campaigns at the Mauna Kea Observatory and at the Haute Provence Observatory.

In the two cases, observations in the pupil plane should be performed in the future.

*Corresponding author address: Julien Borgnino, LUAN, Université de Nice Sophia Antipolis, 28 Avenue, Valrose, France.
E-mail: Julien_Borgnino@unice.fr

First results from a Lunar SHABAR at CTIO

Paul Hickson* and Thomas Pfrommer
University of British Columbia

ABSTRACT

Since October 2006, we have operated a 12-element Lunar Shadow-Band Array (SHABAR) on the summit of Cerro Tololo. The instrument measures spatial correlations in scintillation of light from the moon at a sample rate of 100 Hz. From this, Cn2 profiles are derived for the lower 200 m of the atmosphere as well as time series of the estimated total and high-level seeing. This paper describes the instrument, analysis techniques and initial results.

*_Corresponding author address:_ Paul Hickson, University of British Columbia
E-mail: hickson@physics.ubc.ca

Low Layer SCIDAR: a turbulence profiler for the first kilometer with very high altitude-resolution

Remy Avila*
Universidad Nacional Autónoma de México

Richard Wilson
University of Durham

Mark Chun
University of Hawaii

Salvador Cuevas and Alejandro Farah
Universidad Nacional Autónoma de México

ABSTRACT

The Low Layer Scidar (LOLAS) is aimed at monitoring the turbulence profiles in the first kilometer, with an altitude resolution that can reach 17 m. Its concept is based on the Generalized Scidar technique, but is implemented on a 40-cm dedicated telescope, which makes it an autonomous instrument, ideal for long term site studies.
We present the LOLAS concept, peculiarities and first results.

Corresponding author address: Remy Avila,Universidad Nacional Autónoma de México.
E-mail: r.avila@astrosmo.unam.mx

MOSP: Monitor of Outer Scale Profile

Aziz Ziad*, Jérôme Maire and Julien Borgnino
LUAN,Université de Nice Sophia-Antipolis, CNRS, Observatoire de la Côte d'Azur

ABSTRACT

The Extremely Large Telescopes will be certainly equipped with Multi-Conjugate Adaptive Optics (MCAO) systems. The profile of the outer scale $\mathcal{L}_0(h)$ is a key parameter for these MCAO systems specification and optimization. A new instrument MOSP for $\mathcal{L}_0(h)$ extraction is presented. The first results obtained during observation campaigns at Mauna Kea and Haute Provence Observatory are presented and discussed.

*Corresponding author address: Aziz Ziad, LUAN, Université de Nice Sophia-Antipolis, 28 avenue Valrose, 06100 Nice, France.
E-mail: ziad@unice.fr

1. Introduction

Wavefront outer scale is a relevant parameter for the experimental performance evaluation of large aperture telescopes. The actual size of the outer scale has long been controversial, with measured values ranging from less than 10 m to more than 2 km. What is not controversial is the conclusion that when the diameter of the telescope approaches or exceeds the size of the outer scale, the optical consequences of atmospheric turbulence are changed dramatically from their traditional Kolmogorov behavior. In particular, power in the lowest Zernike aberration modes, e.g., tip and tilt and the overall stroke required for an adaptive-optics system can be much reduced. A finite outer scale has implications for interferometry as well (Winkler 1991, Conan 2000). With the current interest in the design of extremely large ground-based optical and infrared telescopes, reliable estimates of the outer scale profile have assumed considerable importance. A new instrument MOSP (Monitor of Outer Scale Profile) has been developed by our team for outer scale profile extraction. We retrieve the vertical distribution of wavefront outer scale by analysing angular correlation of wavefront Angle of Arrival fluctuations deduced from Moon's limb images motion. We use simulated annealing algorithm to deduce the height dependence of the wavefront outer scale with given structure constant of air-index C_N^2 profiles simultaneously measured with the SCIDAR instrument. We present results obtained during two campaigns of observation at the Mauna Kea Observatory (Hawaii) and Observatoire de Haute Provence (France). Estimated outer scale profiles exhibit smaller values in the boundary layer than in the free atmosphere. Comparisons with the Generalized Seeing Monitor (GSM) outer scale measurements are presented and discussed.

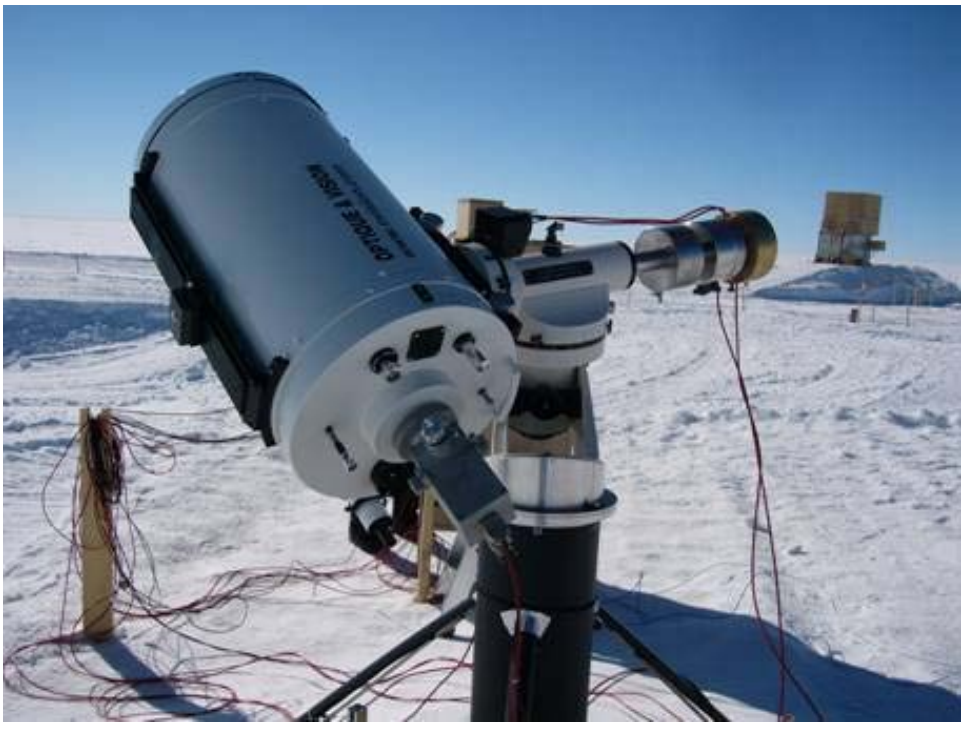

FIG. 1. MOSP at the Dome C site in Antarctica.

2. MOSP instrument

a. Optical devise

The principle of the MOSP instrument is based on the angular correlation of wavefront Angle of Arrival (AA) fluctuations deduced from Moon's limb image motion. The AA fluctuations are measured perpendicularly to the lunar limb leading to transverse correlations for different angular separation along the moon.

The MOSP instrument consists of small telescope ($D \leq 60cm$) having a large focal length $f \sim 10m$. In the case a telescope with small f, a diverging Barlow lens is used increasing the effective focal length of the system, thereby increasing the magnification of the instrument. But this is to the detriment to the field of view (FOV). A compromise has to be found between these parameters.

Images at the focal plane are recorded using a PixelFly CCD camera with 640×480 pixel matrix and $(9.9 \times 9.9)\mu m^2$ pixel size. Its dynamic range of the analogic/digital conversion is 12 bits. The readout noise is 12 e- rms and the imaging frequency is 33Hz. In order to freeze atmospheric effects on Moon's limb image motion, the exposure time was set to 1 or 2ms. The spectral response of the camera is maximal for $\lambda = 0.5\mu m$ in a $375 - 550\mu m$ range.

b. Data processing

The first step of data processing is to retrieve accurately AA fluctuations from Moon's limb motion. After processing on each image a flat and dark field correction, each image $I(x, y)$ is slightly blurred with a median filter M on 3×3 pixel blocks. It avoids possible outliers due to Poisson noise or Moon's small features with relative high intensity differences that can affect the detection of the limb. This type of filtering is more effective than convolution when the goal is to simultaneously reduce noise and preserve edges (Pratt 1978). Each output pixel with coordinates (x, y) contains the median value in the 3-by-3 neighborhood around the corresponding pixel in the input image. Then, an image gradient $G(x, y)$ is processed by convolution with a 3×3 Prewitt edge detector (Pratt 1978) defined as $P = \begin{pmatrix} -1 & -1 & -1 \\ 0 & 0 & 0 \\ 1 & 1 & 1 \end{pmatrix}$, or $-P$ if y-axis points to the Moon center. Detection of the limb position in absolute value of the image gradient is determined by a centroid calculation over each column.

We process $N = 2000$ images (about one minute of acquisition) that gives a set of limb angular positions obtained at a time t. In order to retrieve transverse AA fluctuations $\alpha_\perp$ in a particular set of limb's position, we subtract to this set the temporal mean limb position obtained. The structure function of transverse AA fluctuations is calculated as

$$D_{\alpha_\perp}(\Theta) = \frac{1}{N} \sum_{i=1}^{i=N} \frac{1}{\Theta_m - \Theta} \sum_{k=1}^{k=\Theta_m - \Theta} \left[\alpha_\perp(k) - \alpha_\perp(k + \Theta)\right]^2 \quad (1)$$

where Θ is the angular separation in pixels and Θ_m is the maximal extent accessible in the image, i.e. 640 pixels in our case. This differential variance calculated for each image has the practical advantage of being insensitive to vibration effects of the telescope and tracking errors.

The theoretical form of this angular structure function is given by (Borgnino et al. 1992, Avila

et al. 1997, Bouzid et al. 2002):

$$D_{\alpha,t}(\theta) = 2.4sec(z) \int_0^{+\infty} dh C_N^2(h) \int_0^{+\infty} df f^3 \left[f^2 + \frac{1}{\mathcal{L}_0(h)^2} \right]^{-11/6} \times \left[1 - J_0(2\pi f \theta h) - J_2(2\pi f \theta h) \right] \left[\frac{2J_1(\pi \mathrm{D} f)}{\pi \mathrm{D} f} \right]^2 cos^2(\pi \lambda h f^2) \quad (2)$$

where f is the modulus of the spatial frequency, z is the zenithal distance, D is the aperture diameter, h is the altitude and Θ is the angular separation.

Retrieving $C_N^2(h)$ and $\mathcal{L}_0(h)$ profiles from the AA structure functions (Eq.2) is a non-linear inverse problem. We use simulated annealing (SA) algorithm for minimizing the cost function E, defined as the sum over the angular extent of the squared difference between measured and theoretical AA structure functions $E = \sum_\theta (D_{\alpha_\perp}(\theta) - D_{\alpha_t}(\theta))^2$. This algorithm was developed to statistically find the best global fit of a nonlinear non-convex cost-function (Kirkpatrick et al. 1983).

3. Results

Two different campaigns have been organized with the MOSP instrument. The first one was performed at the Observatoire de Haute Provence (OHP) in France between the 24th November and 06th December 2004. Site testing instruments GSM (Martin et al. 1994, Ziad et al. 2000) and SCIDAR (Fuchs et al. 1998) were also observing simultaneously. During the OHP campaign, a 20-cm telescope (f/15) was used with a $\times 3$ diverging Barlow lens. The Second observation campaign has been carried out at the Mauna Kea Observatory in Hawaii between the 13th and 19th July 2005 with simultaneous observation using the SCIDAR instrument installed at the UH 2.2m telescope, 150m northeast of the 0.61m telescope used by the MOSP. The UH 60cm telescope is a Cassegrain with a 9.24m focal length (f/15.2).

As the difference in altitude between the UH0.6m and the UH2.2m telescopes is about 30m, a difference of total turbulent energy on the propagation path can occur. Firstly, we estimate both $C_N^2(h)$ and $\mathcal{L}_0(h)$ from the Moon limb. We compensate the value of the SCIDAR C_N^2 in the lower slices until the C_N^2 integration over altitude corresponds to the initial integration of $C_N^2(h)$ estimated with Moon's limb. Then, these modified simultaneous SCIDAR C_N^2 profiles are used with the SA algorithm in order to have only $\mathcal{L}_0(h)$ as unknowns. Total error expected is about 10%. The vertical resolution obtained is a trade-off between the need to have a good sample of the first kilometer above the observatory and the reliability expected for results.

Fig.2 shows examples of profiles obtained during the OHP and Mauna Kea campaigns . Median profiles obtained during whole missions show lower values of the outer scale for the first kilometer of the atmosphere. This result can be completed with theoretical relation found by (Ishimaru 1978) who found that the outer scale is on the order of height near the ground.

The simulated annealing algorithm is also appropriate to extract both $C_N^2(h)$ and $\mathcal{L}_0(h)$. In this case, the MOSP can be a completely independent instrument. However, the optimal vertical resolution in the free atmosphere is small compared to the SCIDAR one and results obtained are less reliable. Example of $C_N^2(h)$ profile obtained is compared with simultaneous Scidar measurement and show a good agreement (Fig. 3).

The comparison between the outer scale measured by GSM and the integrated MOSP outer scale (Borgnino et al. 1990) measured simultaneously gives excellent agreement.

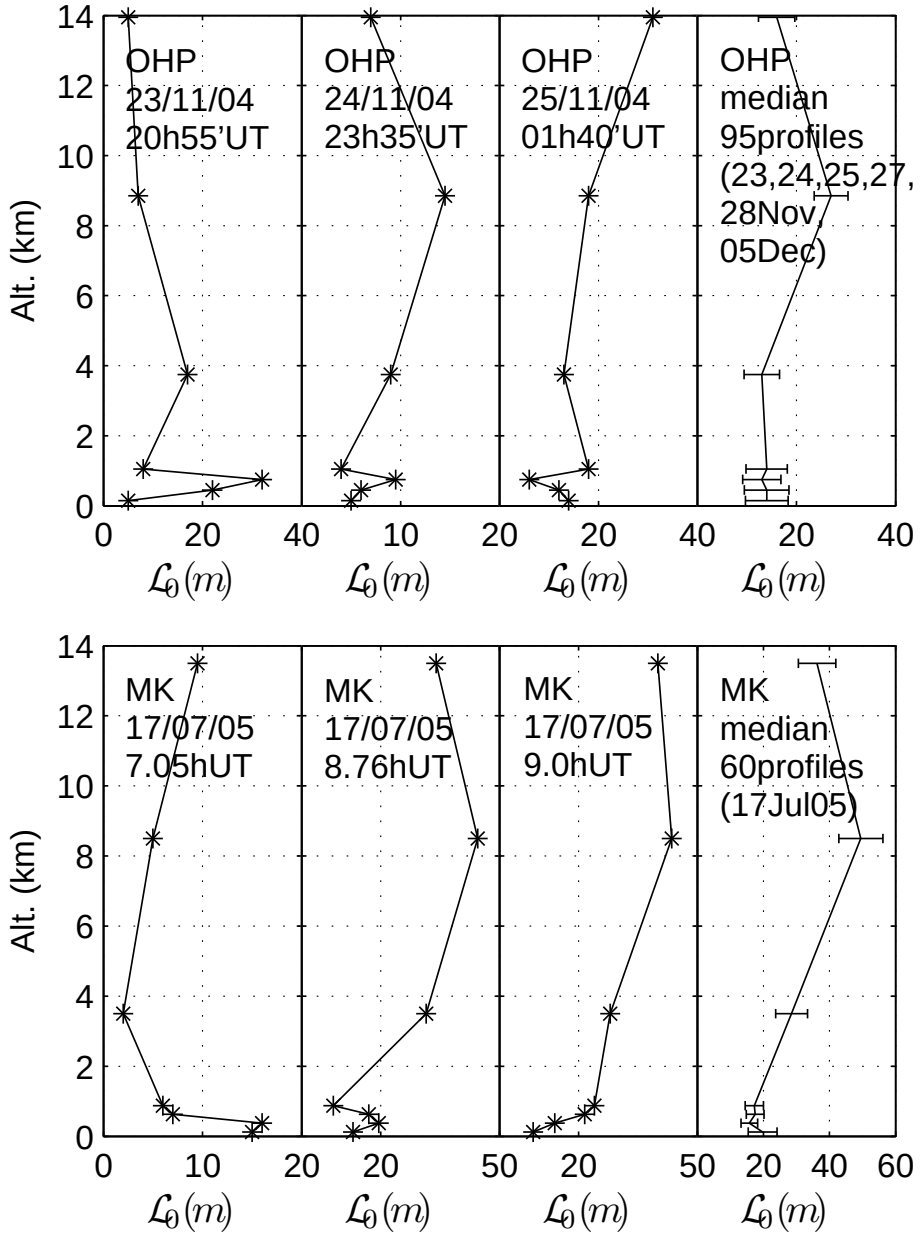

FIG. 2. Examples of outer scale profiles obtained at the OHP (top) and Mauna Kea Observatory (bottom) during several nights. Altitudes are above the observatory. In the right, median outer scale values for whole campaigns are represented with the standard deviation of the values obtained.

4. Conclusion

For the first time monitoring of the outer scale profile is possible from Moon's limb observations with a simple device and small telescope apertures. This instrument is also able to extract simultaneously both of C_N^2 and outer scale profiles. From the first observations, measured outer

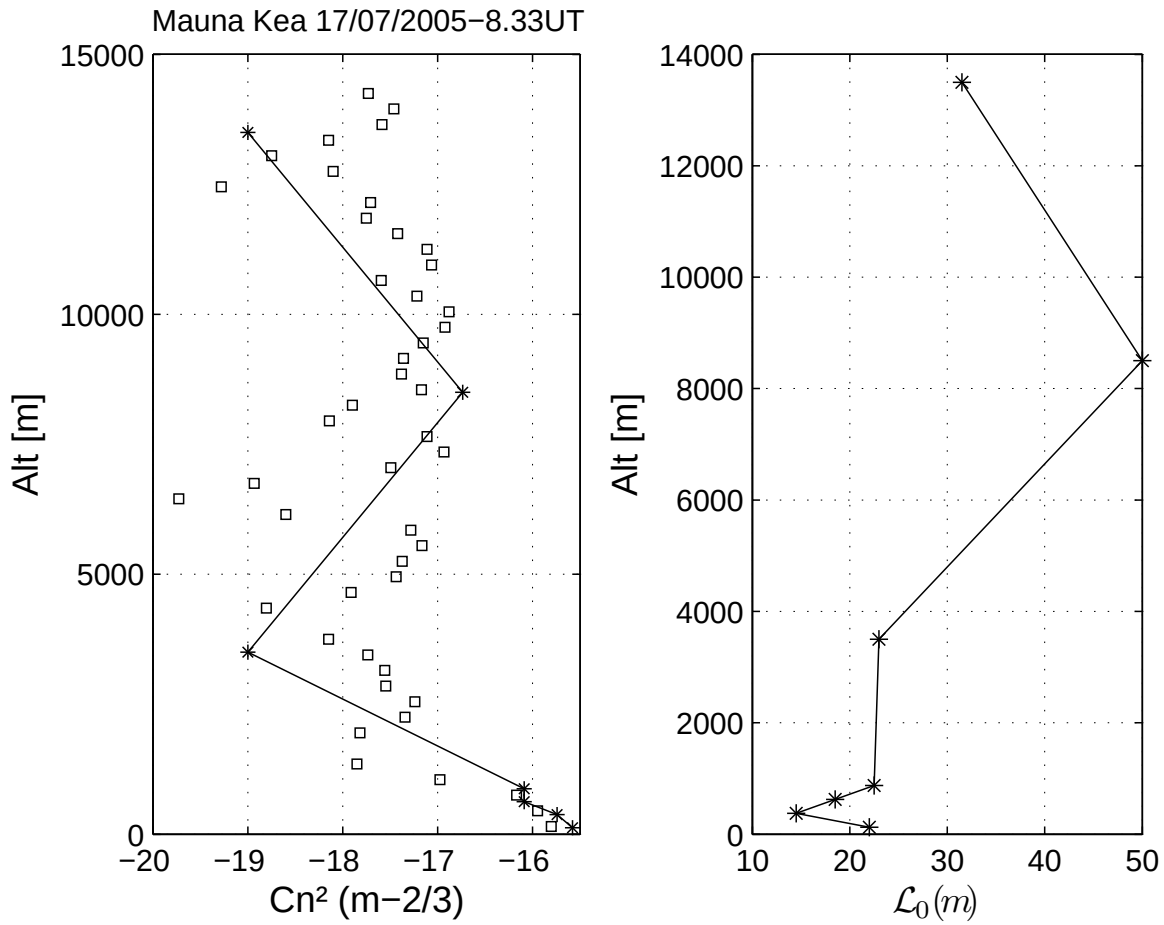

FIG. 3. Example of C_N^2 and outer scale profiles (solid line) that can be retrieved simultaneously using the simulated annealing method. Comparisons with simultaneous SCIDAR profile (square markers) are in close agreement despite different vertical resolutions of these instruments.

scale profiles exhibit smaller values in the boundary layer than in the free atmosphere. Comparisons with GSM outer scale measurements give excellent agreement.

References

Avila R., Ziad A., Borgnino J., Martin F., Agabi A., Tokovinin A., 1997, J. Opt. Soc. Am. A, 14, p.3070-3082

Borgnino J., Martin F., Ziad A., 1992, Optics Communications, 91, p.267-279

Borgnino J., 1990, Appl. Opt., 29, p.1863-1865

Bouzid A., Irbah A., Borgnino J., Lantéri, H., 2002, ASP Conf. 266: Astronomical Site Evaluation in the Visible and Radio Range (Ed. Vernin J., Benkhaldoun Z., Muñoz-Tuñón C.), p.64

Conan R., 2000, PhD thesis, Univ. Nice Sophia-Antipolis

Fuchs A., Tallon M., Vernin J., 1998 PASP, 110, p.86-91

Ishimaru A., 1978, Wave propagation and scattering in random media II (New York, Academic Press, Inc.)

Kirkpatrick S., Gelatt C. D., Vecchi M. P., 1983, Science, 220, p.671-680

Maire J., Ziad A., Borgnino J., Mourard D., Martin F., Jankov S., Bonneau D., Patru F., 2006, A&A, v.448, 3, p.1225-1234

Martin F., Tokovinin A., Agabi A., Borgnino J., Ziad A., 1994, A&AS, 108, p.173-180

Pratt W. K., 1978, Digital image processing (A. Wiley-Interscience Publication, New York: Wiley)

Winker D. M., 1991, J. Opt. Soc. Am. A, 8, p.1568-1573

Ziad A., Conan R., Tokovinin A., Martin F., Borgnino J., 2000, Appl. Opt., 39, p.5415-5425

Characterization of Atmospheric Optical Turbulence along Two Horizontal Paths and Comparison with Vertical Path Turbulence

Marjorie Shoemake*
Boeing-LTS

Barbara Landesman
Lockheed Martin Space Systems Company

ABSTRACT

Atmospheric turbulence data along one mile (Path 1) and two mile (Path 2) horizontal paths have been collected with scintillometers at the Air Force Research Laboratory Starfire Optical Range (SOR) in Albuquerque, New Mexico. The data along Path 1 were collected with a Long Baseline Optical Anemometer & Turbulence Sensor (LOA) manufactured by Optical Scientific Inc. (OSI), and the data along Path 2 were collected with a Scintec Boundary Layer Scintillometer (BLS900). Data from Path 1 have been collected continuously on a 24/7 basis since March 2003. The Path 2 scintillometer data have been collected continuously from November 2005 – April 2006. Scintillometers are optical instruments that calculate path average C_n^2 from the intensity fluctuations of a light source as a function of time. Solar radiation (heat flux), wind speed, wind direction, and temperature within the boundary layer have a direct influence on atmospheric turbulence, therefore diurnal and seasonal variations of C_n^2 are expected. From the Path 1 and Path 2 C_n^2, Fried's coherence length, r_0, and isoplanatic angle, θ_0 scaled to 500 nm were derived. A two-dimensional contour representation of a bivariate normal distribution for the natural logarithm of atmospheric parameters of r_0, and θ_0, the isoplanatic angle were then created. Comparison of the horizontal path statistics to vertical path statistics made with a DIMM show the utility of horizontal path testing to simulate ground to space turbulence under certain conditions. The overlay graphically illustrates times during which the horizontal data is a good representation of the vertical turbulence as well as the times during which the opposite is true.

*Corresponding author address: Marjorie Shoemake, Boeing-LTS.
E-mail: marjorie.shoemake@kirtland.af.mil

Waves and Turbulence measurements over Mauna Kea

John McHugh*
University of New Hampshire

George Jumper
Air Force Research Lab

Ivan Dors
University of New Hampshire

John Roadcap
Air Force Research Lab

ABSTRACT

A series of turbulence measurements were performed recently over Mauna Kea on the island of Hawaii. The measurements were made from ascending balloons, and included both turbulence and meteorological measurements. A sequence of nine balloons were launched during the campaign; three each on the nights of December 12, 13, and 17, 2002. The results indicate a variety of altitudes that experience strong turbulence. Of further interest is the measurement of ascent rate of the balloons. During the first two nights of the campaign, the ascent rate of the balloons near the tropopause increased to as much as 12.9 m/s for brief periods; more than twice the expected speed. These altitudes experienced particularly strong levels of turbulence. The regions of high ascent rates are local regions of upwelling, associated with strong mountain wave activity. This conclusion is in agreement with mesoscale model results. The experiments indicate a much stronger flow than predicted by the model, but both model and experiments agree that the regions of high ascent rate are located near the tropopause altitude. Further measurements were made simultaneously with a DIMM's seeing monitor, located on the summit of Mauna Kea, and the GroundWinds LIDAR, located on nearby Mauna Loa, and will be compared with the balloon measurements.

Corresponding author address: John McHugh, University of New Hampshire.
E-mail: john.mchugh@unh.edu

The Mauna Kea ground-layer characterization campaign

Mark Chun*
University of Hawaii

Richard Wilson
University of Durham

Remy Avila
Universidad Nacional Autónoma de México

Don Weir

ABSTRACT

We have begun a 12-month study of the distribution of turbulence within the first kilometer above the summit of Mauna Kea for the Gemini Observatory. The campaign uses a combination of a SLODAR and a LOLAS to provide a dataset of the turbulence strength and velocity with high-temporal sampling (1 minute) and high spatial sampling (dh~25m) as well as the integrated and free-atmosphere seeing. We discuss the issues in combining and operating the SLODAR/LOLAS instrument and present examples from the dataset.

*Corresponding author address: Mark Chun, University of Hawaii.
E-mail: mchun@ifa.hawaii.edu

The Advance Technology Solar Telescope Site Survey: Instrumentation, Results and application to adaptive optics systems modeling.

Thomas Rimmele*
National Solar Observatory

Frank Hill
National Solar Observatory

The ATST Site Survey Working Group

ABSTRACT

The ATST site survey evaluated six sites were with a set of instrumentation that consisted of a solar differential image motion monitor, a scintillometer array, dust monitor, weather station, and miniature coronagraph. The site survey data was used to compare the test sites in terms of statistics of the fraction of clear time, seeing, dust levels, sky brightness, water vapor, and weather. We will describe the instrumentation and summarize the site survey results, which led to the selection of Haleakala as the ATST site. Haleakala was selected due to its high quantities of excellent seeing and its very dark sky with little seasonal variation. We used the extensive site survey data combined with Cn2 profile measurements from previous survey activity at Haleakala and recent measurements from Mauna Kea to perform adaptive optics systems modeling for ATST's conventional AO system and a possible future MCAO system. The resulting performance predictions will be summarized. ATST's future needs for atmospheric characterization of the Haleakala site will be discussed.

*Corresponding author address: Thomas Rimmele, National Solar Observatory.
E-mail: rimmele@nso.edu

Statistical turbulence vertical profiles at the Roque de los Muchachos observatory and Teide observatory

Jesús J. Fuensalida*, Begoña García-Lorenzo, Jose M. Delgado,
Ángeles Hernández-Rodríguez
Instituto de Astrofísica de Canarias

and

Jean Vernin
Univ. de Nice Sophia Antipolis, France

ABSTRACT

A suitable characterization of the vertical turbulence distribution on a site should be based in statistical behaviour such as it is required for other parameters in site testing. We present the statistical results of the optical-turbulence profiles at the Roque de los Muchachos observatory and Teide observatory over annual periods. The data were obtained using the generalized SCIDAR technique at the 1m Jacobus Kapteyn Telescope and 1.5m Carlos Sanchez Telescope under unbiased statistical sample criteria because the campaigns were done monthly in the new moon nights. Statistically, most of the turbulence is concentrated close the observatory level (2400 m above sea level) with no more than two turbulent layers at higher altitudes. The temporal evolution of monthly statistical turbulence profiles indicates that the turbulence is concentrated at lower altitude layers during winter. We find a seasonal behaviour of turbulence structure at the ORM.

*Corresponding author address: Jesús J. Fuensalida, Instituto de Astrofísica de Canarias. E-mail: jjf@iac.es

Paranal DIMM and MASS-LITE Comparison after two years of operation

Julio Navarrete* and Marc Sarazin
European Southern Observatory

ABSTRACT

The aim of this paper is to present the results obtained by the two instruments (DIMM and MASS-LITE) running simultaneous measurements of relevant atmospheric parameters like seeing,coherence time isoplanatic angle at ESO Paranal Observatory over two years of operation (Sep. 2004 to Sep. 2006)

*Corresponding author address: Julio Navarrete, European Southern Observatory.
E-mail: jnavarre@eso.org

The Seeing and Turbulence Profile at Las Campanas Observatory: GMT Site Testing Progress Report

Joanna Thomas-Osip*
Las Campanas Observatory/GMT/OCIW

ABSTRACT

We report preliminary results obtained during the first two years of the GMT site testing campaign at Las Campanas Observatory. Seeing is measured through the use of differential image motion monitors (DIMM) at three potential GMT sites as well as at the Magellan Telescopes for reference purposes. The turbulence profile in the free atmosphere is measured with a multi-aperture scintillation sensor (MASS) also located near the Magellan Telescopes. We examine the contribution to the seeing arising in the ground layer (defined here as below an altitude of 500 m) through the difference between the turbulence integrals in the full atmosphere (as measured by DIMM) and in the free atmosphere (as measured by MASS).

*Corresponding author address: Joanna Thomas-Osip, Las Campanas Observatory, GMT, OCIW.
E-mail: jet@lco.cl

Characterizing optical turbulence at Dome A on the Antarctic plateau

Jon Lawrence*, Michael Ashley and John Storey
University of New South Wales

ABSTRACT

The free-atmospheric turbulence above the South Pole is known to be very calm above a ~250 m thick turbulent boundary layer. Dome C station, located higher on the Antarctic plateau, experiences similar free-atmosphere conditions but with a much lower surface boundary layer height (~30 m). It is likely that the optical turbulence at Dome A, the highest point on the Antarctic plateau (first visited in 2005 by a Polar Research Institute of China expedition), is confined even closer to the ice level. Obtaining data from this site represents a difficult technological challenge, due to the remote location and extreme environmental conditions. A collaboration between PRIC, NAOC, and UNSW intends to deploy the PLATO (PLATeau Observatory) to Dome A in the 2007/8 Austral summer. This observatory will characterize the Dome A atmospheric optical turbulence via an instrument suite which could include a Multi-Aperture Scintillation Sensor for upper atmosphere turbulence and a high-resolution Surface layer Non-Doppler Acoustic Radar for near ground turbulence.

*Corresponding author address: Jon Lawrence, University of South Wales.
E-mail: jl@phys.unsw.edu.au

Site testing at Dome C, Antarctica

Jean Vernin*, Abdelkrim Agabi, Eric Aristidi, Merieme Chadid,
Hervé Trinquet and Aziz Ziad
Nice University

ABSTRACT

Here we present the more recent results about site testing at Dome C for what concern high angular resolution in Astronomy: Seeing, isoplanatic angle, coherence time and vertical profiles of optical turbulence and wind speed. Emphasis will be put on the very specific properties of the surface layer at Dome C, thickness and variations.

*Corresponding author address: Jean Vernin, Nice University.
E-mail: vernin@unice.fr

SESSION 2

ADAPTIVE OPTICS, INTERFEROMETRY, AND OTHER APPROACHES TO MITIGATE ATMOSPHERIC OPTICAL TURBULENCE.

Special issues in atmospheric monitoring and characterization for future extremely large telescopes

Brent Ellerbroek* *(invited speaker)*
Calthec, Pasadena, CA

Glen Herriot
Herzberg Institute of Astrophysics

Luc Gilles
Thirty Meter Telescope Project

ABSTRACT

A variety of atmospheric parameters and characteristics become increasingly important considerations for adaptive optical (AO) systems on future extremely large telescopes (ELTs) with aperture diameters greater than approximately 20 to 30 meters. These include the turbulence outer scale (L_0), which influences the stroke and bandwidth requirements for deformable mirrors and tip/tilt mirrors; the thickness, structure, and temporal variability of the mesospheric sodium layer, which have a strong impact upon the design and performance of laser guide star (LGS) AO systems; and the validity of the Taylor (or frozen flow) hypothesis, which determines the potential performance of predictive algorithms for tip/tilt and higher order wavefront control. In addition, the multi-LGS AO systems proposed for future ELTs provide an interesting opportunity for real-time SLODAR characterization of the atmospheric C_n^2 profile during astronomical observations. We describe these issues and present sample results obtained as part of the design and evaluation of AO systems for the Thirty Meter Telescope (TMT) project.

Corresponding author address: Brent Ellerbroek, Calthec, Pasadena, CA.
E-mail: brente@caltech.edu

Atmospheric Turbulence Profiling using Multiple Adaptive Optics

Lianqui Wang*
Calthec, Pasadena, CA

Gary Chanan
University of California, Irvine

Matthias Schoeck
The Thirty Meter Telescope Project

ABSTRACT

The Slope Detection And Ranging (SloDAR) method recovers atmospheric turbulence altitude profiles from the time averaged spatial cross-correlation of the wavefront slopes measured by Shack Hartmann wavefront sensors (SHWFS). The Palomar Multi-Guide Star Unit (MGSU) is set up to test tomographic multiple guide star adaptive optics on the 5-meter telescope and provides an ideal test bed for SloDAR turbulence profiling. The MGSU contains four independent SHWFS cameras. Each pair of cameras (six pairs in total) was used to perform SloDAR analysis. An engineering run with natural guide stars was carried out in February 2006. In this talk we will present the SloDAR profiling results and compare these with simultaneous DIMM/MASS measurements. We will also discuss the methods used to deal with such problems as static aberrations and bright sky backgrounds (with 4x4 pixels in each subaperture). In addition we performed wind profiling using time delayed cross-correlations to determine wind speed and direction. We were able to measure five layers with different altitudes, wind speeds and directions and to use these results to improve the resolution of the turbulence profiles by a large factor.

*Corresponding author address: Lianqui Wang, University of California, Irvine.
E-mail: lianqiw@uci.edu

Comparison of atmospheric conditions as measured by dedicated monitors & as seen on an adaptive optics wavefront sensor

Nancy Ageorges*, Julio Navarrete
European Southern Observatory, Chile

and

Marc Sarazin
European Southern Observatory, Garching

ABSTRACT

NaCo is an adaptive optics fed NIR camera installed at ESO VLT-UT4 and operating for the last 4 years. The system uses the wavefront sensor information to estimate its performance and some typical atmospheric turbulence parameters like r_0, and τ_0. We propose here to compare these online estimated performances as a function of atmospheric parameters measured with both the Paranal Atmospheric Monitor and the Multi-Aperture Scintillation Sensor.

*Corresponding author address: Nancy Ageorges, European Southern Observatory, Chile.
E-mail: nageorge@eso.org

Instantaneous seeing estimates using closed-loop AO images

Szymon Gladysz*
Department of Experimental Physics, National University of Ireland, Galway

Julian Christou
Division of Astronomical Sciences, National Science Foundation, Arlington, VA22203[1]

Lewis C. Roberts, Jr. and L. William Bradford
The Boeing Company, Kihei, HI 96753, USA

ABSTRACT

The temporal variability of atmospheric seeing at short time scales has been investigated by using closed-loop adaptive optics (AO) imaging from two different AO systems at the 3 m Shane Telescope at Lick Observatory (LO) and at the 3.6 m AEOS at Haleakala. The "instantaneous" Strehl ratios were obtained directly from the short-exposure data for the LO observations and from Fourier propagating the measured residual wavefront slopes for the AEOS data. For both sets of data under quasi-stationary conditions, the distribution of the Strehl ratio shows a negative skewness. We have related that effect to the log-normal distribution of the "instantaneous" Fried parameter, r_e.

*Corresponding author address: Szymon Gladysz, Department of Experimental Physics, National University of Ireland, Galway, Ireland
E-mail: Szymon.Gladysz@NUIGalway.ie

[1] on leave from the Center for Adaptive Optics, University of California, Santa Cruz, CA 95064

1. Introduction

The post-processing image sharpening technique of "lucky exposures" (or frame selection) has recently made a comeback into professional astronomy due to the availability of low-noise, fast-readout CCDs in the visible band (Law, Mackay and Baldwin, 2006). The method is advocated as a substantially cheaper alternative to real-time compensation using adaptive optics. This "lucky exposures" imaging prompted our study of the closed-loop AO short-exposure images to investigate how effective this approach would be for closed-loop AO imaging. Even though frame selection has been previously used with AO-assisted imaging (Brandner et al., 1995; Janson et al., 2006), its performance across the range of compensation levels has not been investigated. Given that AO systems stabilize the image quality we expected relatively less high-quality outliers – which are the basis of this method – than in the case of non-compensated imaging.

2. Observations

a. Lick Observatory

The authors were privileged to use the AO-equipped 3-m Shane telescope at the Lick Observatory for several nights in 2005 and 2006. The 61-actuator system provides partial correction in the infrared. Closed loop, *K*-band images of single stars ($m_I = 6 - 9$) were obtained using the high-speed sub-array mode with a size of 64 × 64 pixels of the 256 × 256 pixel IRCAL camera (Lloyd et al., 2000). This corresponds to the field size of 4.864 × 4.864 arcseconds. In the *K*-band data where the diffraction-limit is 151 mas, the data was effectively Nyquist sampled with a pixel scale of 76 mas/pixel.

The sub-array measurements were captured with typical exposure time of 22ms. This meant that image blurring caused by the residual image motion after tip-tilt correction was not significant. Each dataset comprised ten thousand images. The frames were re-centred using the peak-tracking algorithm (Gladysz, Christou and Redfern, 2006).

"Instantaneous" Strehl ratio was chosen as the image-quality metric due to its robustness and relative simplicity of computation. Four non-stationary Strehl ratio sub-series are plotted in Fig. 1. A number of trends occurring on the timescales < 1 sec can be noticed. These trends would not normally be noticed when temporal *averages* related to atmospheric seeing are recorded. These temporal changes measured in the focal plane, with correlation scales less than a second, are produced by real changes in the atmospheric turbulence, and are not the effect of measurement error (either the instantaneous Strehl ratio estimation error or the wavefront sensor measurement error propagating through the system).

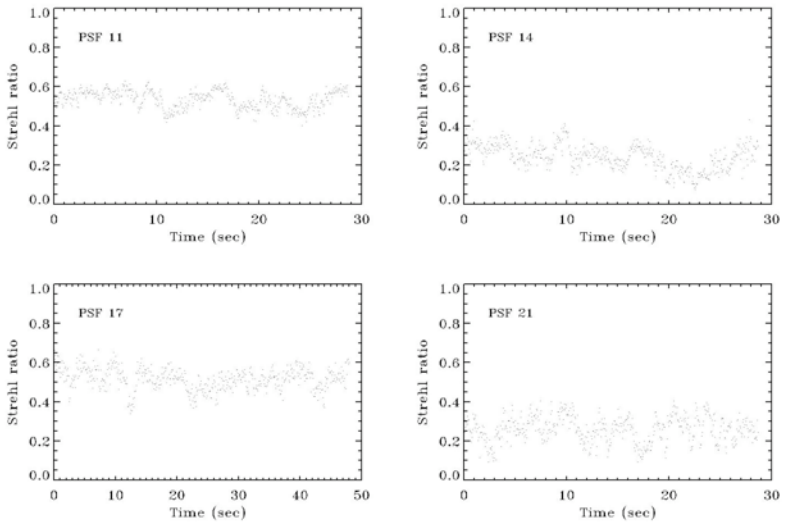

Fig. 1 Time series plots for several chosen Lick datasets (denoted PSF 1, 2, etc.). Only the first few hundred values are plotted.

Of particular interest here was the distribution of the instantaneous image quality, as quantified by the short-exposure Strehl ratio. A positively-skewed (high-end tail) instantaneous Strehl ratio distribution has been observed during a "lucky imaging" (no AO) campaign at the Nordic Optical Telescope (Baldwin et al., 2001). Such a distribution benefits frame selection – plenty of high-quality outliers imply high-resolution and signal-to-noise ratio of the final stacked image. The histograms we found for the Lick quasi-stationary datasets all displayed negative skewness (Fig. 2).

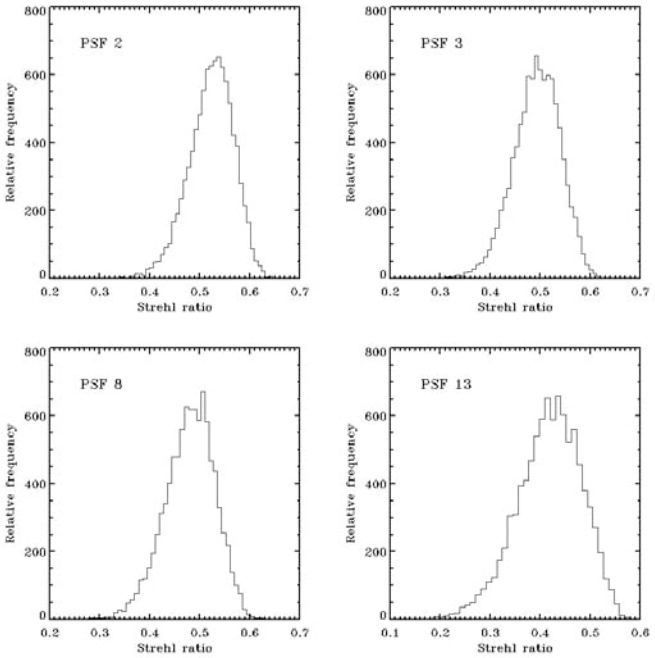

Fig. 2 Histograms of the instantaneous Strehl ratio for four quasi-stationary time series.

The proposed explanation for this effect relies on the introduction of the "instantaneous" Fried parameter, r_e, first proposed by Christou, McCarthy and Cobb, (1987). r_0 is defined only for an ensemble, and r_e represents the statistical variations of the ensemble member, say variation of MTF of the individual short exposure. r_e captures the short-term variability in the atmosphere. It could be measured as a spatial average of a large number of simultaneous angle-of-arrival fluctuations instead of the temporal average of many r_e which is the traditional way of estimating r_0.

The instantaneous Strehl ratio is related to the phase variance of the image-forming wavefront via the Maréchal approximation. Phase variance in turn can be expanded using the AO error budget equations which rely on r_0. We extend this procedure to the short-exposure case, replacing r_0 with r_e, and assuming log-normal distribution for the latter. Given a bijective functional relationship between the instantaneous Strehl ratio and r_e, SR = $f(r_e)$, one can obtain the Probability Density Function (PDF) of SR. The PDF we found this way provides a very good fit to the histograms of the stationary SR sequences (Gladysz, Christou and Redfern, 2006).

The problem with the above transformation is that the distribution of r_e is not known. While the distribution of the r_0 has been extensively measured during site testing campaigns (Barletti et al., 1977; Walters and Bradford, 1997) and good fits with the log-normal PDF have been found, only a few papers mention the measurements of its instantaneous counterpart. In Section 3 we report on the existing measurements of r_e.

b. Advanced Electro-Optical System

Observations with the Advanced Electro-Optical System (AEOS) telescope (Roberts and Neyman, 2002) were carried out over six nights in 2004 and 2005 (Christou et al., 2006). No high-speed focal plane data was available here. The images were generated from the reconstructed closed-loop residual phases measured at a frame rate of 200Hz. The phases were numerically propagated through the obscured 3.6m aperture to generate the corresponding PSFs at the sensing wavelength of 0.625μm. It has to be emphasized that the PSFs obtained this way did not suffer from non-common-path errors in the system, and the resulting Strehl ratios were extremely high. Also, there was no readout noise in the images. It should also be mentioned that these PSFs corresponded to estimated wavefronts, and the aberrations which were not sensed by the wavefront sensor did not influence them.

Computing the instantaneous Strehl ratio for the AEOS data was done by comparing the frames with the numerically obtained diffraction-limited image. Similarly to the Lick measurements, the AEOS Strehl ratio histograms displayed low-end tails. The negative skewness was very significant in this data. Thus, the negatively-skewed distribution which was first observed at the Lick Observatory is confirmed beyond any reasonable doubt.

3. Distribution of r_e

r_e had been measured occasionally (Christou, McCarthy and Cobb, 1987) and its log-normality had been briefly signaled (Mariotti et al., 1983). Given a single 2000-frame speckle dataset from the Lick Observatory, r_e estimate was computed for each frame by fitting the speckle transfer function to individual intensity power spectra. These power spectra were first reduced by the average sky power spectrum. Because the resulting spectra showed large anisotropy we calibrated them by subtracting the mean anisotropic

content and shifting by the theoretical speckle transfer function. The histogram of r_e values had a significant high-end tail. After the logarithmic transformation the dataset was fitted with a Gaussian cumulative distribution function (Fig. 3). The quality of the fit was very good.

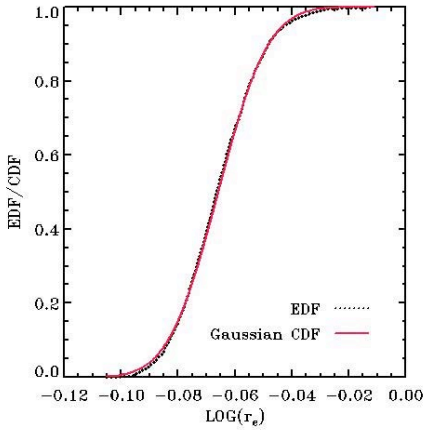

Fig. 3 Gaussian fit to the estimates of log(r_e) extracted from non-compensated speckles.

4. Conclusions

We have demonstrated the need to explain short-timescale correlations in the instantaneous Strehl ratio by the introduction of the instantaneous seeing parameter r_e. The distribution of this parameter, which we suspect to be log-normal, helps explain the unusual, negative skewness of the AO-corrected Strehl ratio.

References

Baldwin, J. E., R. N. Tubbs, G. C. Cox, C. D. Mackay, R. W. Wilson, and M. I. Andersen, 2001: Diffraction-limited 800nm imaging with the 2.56m Nordic Optical Telescope. *Astronomy and Astrophysics*, **368**, L1-L4.

Barletti, R., G. Ceppatelli, L. Paternò, A. Righini, and N. Speroni, 1977: Daytime r_0 evaluated from vertical microthermal measurements. *Applied Optics*, **16**, 2419-2421.

Brandner, W., J. Bouvier, E. K. Grebel, E. Tessier, D. de Winter, and J.-L. Beuzit, 1995: Low-mass star formation in CG1: a diffraction limited search for pre-main sequence stars next to NXPup. *Astronomy and Astrophysics*, **298**, 818-826.

Christou, J. C., D. W. McCarthy, Jr., and M. L. Cobb, 1987: Image selection and binning for improved atmospheric calibration of infrared speckle data. *Astronomical Journal*, **94**, 516-522.

Christou, J. C., S. Gladysz, M. Redfern, L. W. Bradford, and L. C., Roberts, Jr., 2006: Characterization of the variability of the Strehl ratio of adaptive optics point spread functions. *Proceedings of the 2006 AMOS Technical Conference, September 10-14*.

Gladysz, S., J. C. Christou, and M. Redfern, 2006: Characterization of the Lick adaptive optics point spread function. *SPIE Proceedings*, **6272**.

Janson, M., W. Brandner, T. Henning, and H. Zinnecker, 2006: Early ComeOn+ adaptive optics observation of GQ Lup and its substellar companion. *Astronomy and Astrophysics*, **453**, 609-614.

Law, N. M., C. D. Mackay, and J. E. Baldwin, 2006: Lucky imaging: high angular resolution imaging in the visible from the ground. *Astronomy and Astrophysics*, **446**, 739-745.

Lloyd, J. P., M. C. Liu, B. A. Macintosh, S. A. Severson, W. T. Deich, and J. R. Graham, 2000: IRCAL: the infrared camera for adaptive optics at Lick Observatory. *SPIE Proceedings*, **4008**, 814-821.

Mariotti, J. M., A. Chelli, F. Sibille, R. Foy, P. Lena, and G. Tchountonov, 1983: Infrared speckle imaging - Improvement of the method; results on Miras and protostars. *Astronomy and Astrophysics*, **120**, 237-248.

Roberts, L. C., Jr. and C. R. Neyman, 2002: Characterization of the AEOS adaptive optics system. *Publications of the Astronomical Society of the Pacific*, **114**, 1260-1266.

Walters, D. L. and W. L. Bradford, 1997: Measurements of r_0 and θ_0: two decades and 18 sites. *Applied Optics*, **36**, 7876-7886.

The Anisoplanatic Point Spread Function in Adaptive Optics

Matthew Britton*
Caltech Optical Observatories

ABSTRACT

In a classical adaptive optics system, anisoplanatism introduces a field dependent degradation in the point spread function (PSF). This degradation also evolves in time due to changes in the atmospheric turbulence profile. This talk presents the results of an experiment in which adaptive optics images of a 21" binary observed with the Palomar Adaptive Optics system on the Hale 5 m telescope and turbulence profile measurements from a DIMM/MASS unit were acquired contemporaneously. The measured turbulence profiles were used together with images of the primary to predict the evolution of the long exposure PSF of the secondary. These predictions were shown to agree with the observed images to a high degree of accuracy. These PSF predictions were then used to derive differential astrometry of the binary accurate to 1 mas and differential photometry accurate to .1%.

*Corresponding author address: Matthew Britton, Caltech Optical Observatories
E-mail: mbritton@astro.caltech.edu

The widest contiguous field of view at Dome C and Mount Graham

Jeff Stoesz*, Elena Masciadri, Franck Lascaux and Susanna Hagelin

INAF - Osservatorio Astrofisica di Arcetri, Florence, Italy

ABSTRACT

The image quality from Ground-Layer Adaptive Optics (GLAO) can be gradually increased with decreased contiguous field of view. This trade-off is dependent on the vertical profile of the optical turbulence (C_n^2 profiles). It is known that the accuracy of the vertical distribution measured by existing C_n^2 profiling techniques is currently quite uncertain for wide field performance predictions, 4 to 20 arcminutes. With assumed uncertainties in measurements from Generalized-SCIDAR (GS), SODAR plus MASS we quantify the impact of this uncertainty on the trade-off between field of view and image quality for photometry of science targets at the resolution limit. We use a point spread function (PSF) model defined analytically in the spatial frequency domain to compute the relevant photometry figure of merit at infrared wavelengths. Statistics of this PSF analysis on a database of C_n^2 measurements are presented for Mt. Graham, Arizona and Dome C, Antarctica. This research is part of the activities of ForOT (3D Forecasting of Optical Turbulence above astronomical sites).

*Corresponding author address: Jeff Stoesz, INAF - Osservatorio di Arcetri, Largo Enrico Fermi 5, Firenze, FI 50125, Italy.

E-mail: stoesz@arcetri.astro.it

1. Introduction

Characterization of the optical turbulence in the first few kilometres above the telescope is important for predicting the performance of Ground-Layer Adaptive Optics (GLAO) telescopes as a function of field of view diameter. Systems that have been proposed will correct visible or near-infrared science fields that are typically 4 arcminutes, and potentially up to 20 arcminutes in diameter and contiguous. There are several measurement techniques being advanced to provide statistics on the vertical distribution of the structure function coefficient $C_n^2(h)$, and in this paper we explore the impact of a potential bias from generalized-SCIDAR and MASS measurements. The first of two sites we will investigate is a typical mid-latitude observatory site, Mount Graham (32.7 N, 109.87 W, 3200 meters), measured with generalized-SCIDAR. There are conifer trees at the summit with a height similar to the SCIDAR telescope's primary mirror, about 8 meters above the ground. The second is Dome C (75.1 S, 123.3 E, 3260 meters), an Antarctic site with MASS and SODAR measurements by Lawrence et al. (2004) and balloon measurements by Agabi et al. (2006).

The GLAO PSF figure of merit that is of particular importance to wide field astronomy is radius of 50% encircled energy, computed at several points in the contiguous field of view and then averaged. It will be symbolized as $EE50$ here. $EE50$ is very closely related to the integration time to achieve some signal to noise ratio in background-limited point source photometry in the field (Andersen et al. 2006), a rather common science application for fields of view 4 to 20 arcminutes in diameter. Roughly,

$$\text{integration time} \propto EE50^2. \tag{1}$$

We will compute $EE50$ starting with an analytically defined phase Power Spectral Density (PSD) for anisoplanatism and fitting error using established theory (Jolissaint et al. 2006; Tokovinin 2004). Table 1 lists the model parameters selected here. Computation from the analytic PSD is a fast method to discover the performance gradient of $EE50(\theta)$, where θ is the diameter of the field of view.

The exact range of altitudes in the first few kilometres where bias has greatest impact depends on the basic GLAO system parameters, namely the diameter of the guide star asterism (also θ) whose signal is averaged and the effective pitch that is controlled by the ground conjugated deformable mirror (Δ). The ratio $h_{GZ} = \Delta/\theta$ defines the altitude below which any contribution to anisoplanatism is negligible. The term gray-zone (GZ) was coined (Tokovinin 2004) to identify the altitudes above h_{GZ}, where the contribution to anisoplanatism is not negligible (also known as

TABLE 1. The parameters and implicit assumptions of the GLAO PSF model.

phase PSD	von Kármán, $L_o = 30$ meters
telescope diameter	$D = 8$ meters
Beacons	4 point sources at range $H = 90$ km at zenith
Beacons	evenly distributed on a circle of diameter θ in the field
image wavelength	$\lambda = 1.25\mu m$
image locations	sampling a square field of view with vertices that intersect the circle
Deformable Mirror	cartesian grid of actuators with pitch Δ
Deformable Mirror	each actuator has a sinc-like influence function
Deformable Mirror	conjugated to height = 0

partially corrected zone).[1] Fig.1 helps illustrate this in terms of performance in the focal plane. The plot shows the $EE50$ figure of merit as a function of the height of one layer of turbulence added to a typical, smooth profile. The layer contains half of the total turbulence strength of the smooth profile. Fig.1 shows that the largest performance gradient is at altitudes just above h_{GZ}. The gradient vanishes above $h_D = D/\theta$, where D is the telescope diameter. In the following sections we will re-compute $EE50(\theta)$ with estimated bias in the proportion of turbulence attributed to heights above or below h_{GZ}.

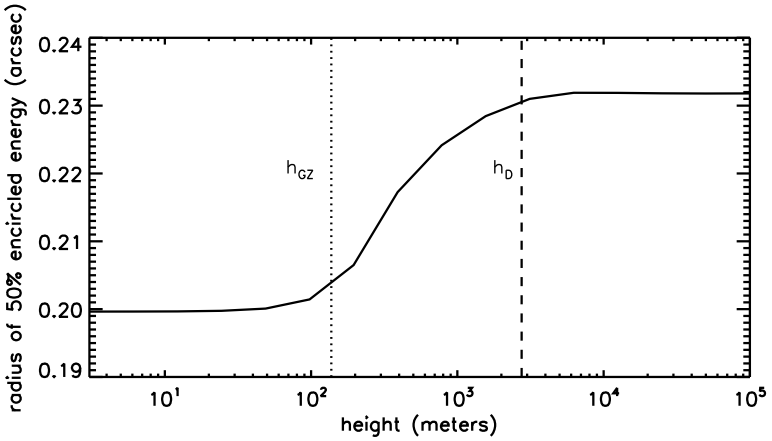

FIG. 1. The gray-zone begins above h_{GZ}.

2. Mount Graham and Dome C profile monitoring data

The Mt. Graham G-SCIDAR measurements include 851 in High Vertical Resolution (HVR) mode and 9911 in regular mode, both have been reduced to discretized turbulence strength J_i at height h_i. These were computed (Egner et al. 2006, 2007) from the normalized covariance function of the irradiance fluctuations, which are proportional to J_i, which are in turn related to $C_n^2(h)$ by

$$J_i = \int_{h_{bi}}^{h_{b_{i+1}}} dh\, C_n^2(h). \tag{2}$$

The intrinsic vertical resolution of SCIDAR is roughly given by

$$\frac{0.78}{\rho}\sqrt{\lambda|h + h_{gs}|} \tag{3}$$

where ρ is the binary separation ($35''$), λ is the wavelength of the scintillation signal ($0.5\mu m$), and h_{gs} is the conjugation height of the generalized SCIDAR analysis plane (about $-3500m$). The regular mode resolution will represent free-atmosphere, above 1000 meters. The current HVR data set samples the scale height of the boundary-layer and provides data up to 1000 meters altitude. In a subsequent section we will describe how the ground-layer and free-atmosphere are reduced to form a composite statistical model.

[1] Looking at the approximate error transfer function in equation (8) of Tokovinin (2004) one can see why this is the case.

For Dome C we will use 1701 MASS+SODAR profile monitoring measurements at Dome C by Lawrence et al. (2004) during the Antarctic winter of 2004. These data sample only two grid points between 30 and 1000 meters and do not sample any turbulence below 30 meters. However, there exist balloon-borne micro-thermal measurements (Agabi et al. 2006) that give us an estimate of the scale height and total strength of the ground-layer, and with this information we model the statistics of eight grid points from a height of zero to 200 meters. The turbulence measurements recorded by SODAR in the Lawrence et al. (2004) data we appropriate to a slab concentrated at 250 meters between the modelled ground layer and the lowest MASS measurement at 500 meters.

For the Dome C altitudes from zero to 200 meters we define the following exponential model to

$$C_n^2(h) = Ae^{(-h/h_A)}. \tag{4}$$

Using Eqn.(2) it follows that

$$J_i = -Ah_A \left(e^{(-h_{bi+1}/h_A)} - e^{(-h_{bi}/h_A)} \right). \tag{5}$$

Using a average, weighted by $C_n^2(h)$

$$\begin{aligned} h_i = & \frac{\int_{h_{bi}}^{h_{bi+1}} dh\, C_n^2(h)\, h}{\int_{h_{bi}}^{h_{bi+1}} dh\, C_n^2(h)}. \\ = & \frac{-Ah_A \left[(h_{bi+1} + h_A)e^{(-h_{bi+1}/h_A)} - (h_{bi} + h_A)e^{(-h_{bi}/h_A)} \right]}{J_i}. \end{aligned} \tag{6}$$

It has been observed with balloon measurements at Cerro Pachon (Tokovinin and Travouillon 2006) that the strength of ground-layer is governed primarily by the scale height. In our model we will make the scale height dictate the strength exclusively. A lognormal distribution of values of the scale height, h_A, while $A = 740. \times 10^{-16}$ and is fixed, will give a lognormal distribution in seeing.

The Mt. Graham (MG) scenario has weaker overall seeing (median 0.74 arcseconds) than Dome C (DC, median 1.2 arcseconds). To illustrate the differences in the vertical distributions for these two sites we reduce the data to cumulative histograms of seeing in three slabs, shown in Fig.2. The Dome C free atmosphere (right panel) and even upper ground-layer slab (middle)are quite calm. The concentration of the ground-layerturbulencemeasured at Mt. Graham is possibly at the limit ofvertical resolution by the HVR-GS technique, about 200 meters using equation 3. The DC scenario clearly has most turbulence concentrated between the telescope and 30 meters range (left panel Fig.2).

3. Reduction to composite profiles

Since the measurements of the ground-layer and free-atmosphere at these sites is not simultaneous, we must create composite profiles that would closely reproduce the PSF statistics as though we had computed them on a full set of $J_i(h_i)$ data, uninterrupted in h and sampled at the same time. To do this we sort and combine the profiles of as described in Tokovinin and Travouillon (2006) using the assumption of uncorrelated ground-layer and free-atmosphere seeing. We will briefly re-describe the process here in the context of our data.

The Mt. Graham HVR will provide the ground-layer below 1000 meters and the regular SCIDAR measurements will provide the free-atmosphere above 1000 meters. Three groups of profiles

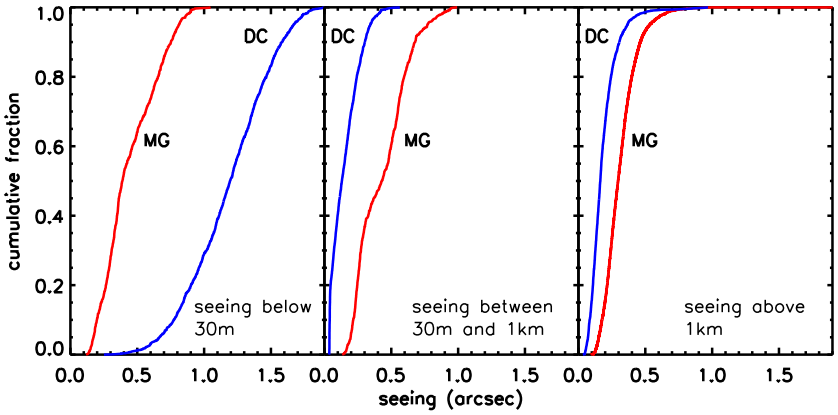

FIG. 2. Comparison of the Dome C (DC) and Mount Graham (MG) turbulence profile data used here.

in the ground-layer are identified using the sum of J_i. The first group are those profiles within 5% of the 25th percentile are combined in a simple average for J_i. We call them the "good" case. The 50th and 75th percentile profiles area combined similarly and called "typical" and "bad". In each group the grid of h_i is identical and hence remains unchanged by the combining process. The same process is done for the free-atmosphere. The result is a reduction to three ground layer profiles and three free-atmosphere profiles, which together have nine permutations for composite profiles that can reproduce the PSF statistics as though we had computed them on all of the $J_i(h_i)$ data.

For Dome C we sort and combine the MASS+SODAR profile monitoring measurements of the free-atmosphere above 200 meters in the same way we described for Mt. Graham. The ground-layer model does not need to be sorted; the choice of three scale heights $h_A = [14, 9, 22]$ meters provide the median, first and last quartile of the integrated ground-layer.

4. Resampling the Composite Profiles

In all cases the shape of the composite profiles, whether averaged over time or defined by a function is smooth and well sampled by the grid of $J_i(h_i)$ defined so far. Hence, we are permitted to resample the the $J_i(h_i)$ grid for the GLAO PSF model, which is affected by the density of points in the gray-zone. We increase the number of grid points in the gray-zone until the PSF figure of merit has reached an asymptote. This is trivial for the ground-layer of Dome C, we can define the h_b grid and then re-compute $J_i(h_i)$ with Eqn.(5) and Eqn.(6). For the measurements of Mount Graham and the free-atmosphere of Dome C we divide several measured $J_i(h_i)$ grid into more numerous $J_j(h_j)$ using nearest neighbour interpolation of the original discretized $C_n^2(h)$ data.

5. Predicted GLAO performance gradient

The reduced composite $C_n^2(h)$ profiles for each site are input for the computation of field averaged radius of 50% encircled energy of PSFs at a wavelength of $1.25\mu m$, outlined in §1, and symbolized $EE50$. The aim is to asses the impact on GLAO performance by potential biases in the measured vertical distribution of the turbulence strength. We have selected the performance $EE50(\theta)$ metric to do this. Fig.3 is a 3x3 multi-panel plot showing $EE50(\theta)$ at Mt. Graham (red)

and Dome C (blue). The thicker lines are the median values while the thinner ones are the first and last quartiles of the ordinate.

Let us first consider the central column of plots to identify the fundamental differences between weak and strong free-atmosphere sites. In the upper one we see the Mt. Graham (red) $EE50$ gracefully increasing with θ, as the bottom of the gray-zone (§1) reaches into the boundary-layer turbulence 100 to 250 meters thick. For this top middle panel the actuator pitch of the DM was 0.5 meters and the Dome C scenario only very weakly affected by anisoplanatism, a consequence of an inadequate number of actuators for that scenario. In the central panel the pitch is 0.38 meters, which improves correction at Mt. Graham slightly in all conditions, and greatly improves Dome C for median or better conditions. The median and first quartile $EE50(\theta)$ curves of Dome C and Mt. Graham have similar shape because the ground-layer profiles at Mt. Graham have similar exponential shape. The bottom plot shows the potential gain for Dome C when the wavefront is controlled to a pitch of 0.1 meters. In the central column of plots, the important distinction between the two sites is that Dome C is always under-actuated with $\Delta = 0.5$ and sometimes near the diffraction-limited $EE50$ with $\Delta = 0.1$. Mt. Graham on the other hand has more high altitude turbulence and is always limited by anisoplanatism for these Δ.

Next, consider the columns of panels to the left and right of Fig.3 showing uncertainties pertinent to field of view trade-offs in GLAO telescope design.As indicated in figure 4 in Tokovinin et al. (2005) both MASS and SCIDAR measurements are believed to produce faithful total integrals of turbulence, however, the vertical distribution may be biased. The left column of plots in Fig.3 were computed from the $J_i(h_i)$ times 0.5 in the domain $h_{gz} < h_i < 6km$, the balance was conserved by putting turbulence in the lowest layer, below h_{GZ}. Likewise the the right column of plots is $J_i(h_i)$ times 1.5 in the domain $h_{gz} < h_i < 6km$, with the balance conserved by removing turbulence from the lowest layer. The change from the central column of plots to the left or the right is the slope of the curves, germane to designing a field of view trade-off. The performance of a wide field survey can be expressed using the number of square arcminutes of sky that can be imaged to some limiting magnitude per unit time. For a theoretical seeing-limited telescope this is of course proportional to θ^2. For a GLAO telescope with field of view θ it will be roughly proportional to $(\theta/EE50(\theta))^2$. $EE50(\theta)$ in the middle row of Fig.3 ($\Delta = 0.38$ meters) the slope of the median Mt. Graham $EE50(\theta)$ in the domain $10 < \theta < 20$ arcminutes is about 45% less or more in the left or right panels. It is about $\mp 15\%$ for Dome C. In terms of $integration\ time(\theta) \propto EE50(\theta)^2$ in the domain $10 < \theta < 20$ we find the slope is $\pm 60\%$ for Mt. Graham, $\pm 30\%$ for Dome C. In other words, at a mid-latitude site similar to Mt. Graham, the predicted survey coverage of the GLAO telescope could potentially be wrong by as much as 60%.

6. Summary

The GLAO telescope scenario simulated here is a common design for wide field science demanding a contiguous field. The estimate of 50% uncertainty in the proportion of turbulence strength between the the corrected-zone and the gray-zone (in the first 6 km) is based on a comparison between MASS and SCIDAR and here we calculate an uncertainty of 60% in the slope function $EE50(\theta)$. Dome C is truly a unique site, and more immune to the 50% uncertainty. However, if the true uncertainly is not simply multiplicative the uncertainty propagated to $EE50(\theta)$ for Dome C might be similar to that of Mt. Graham.

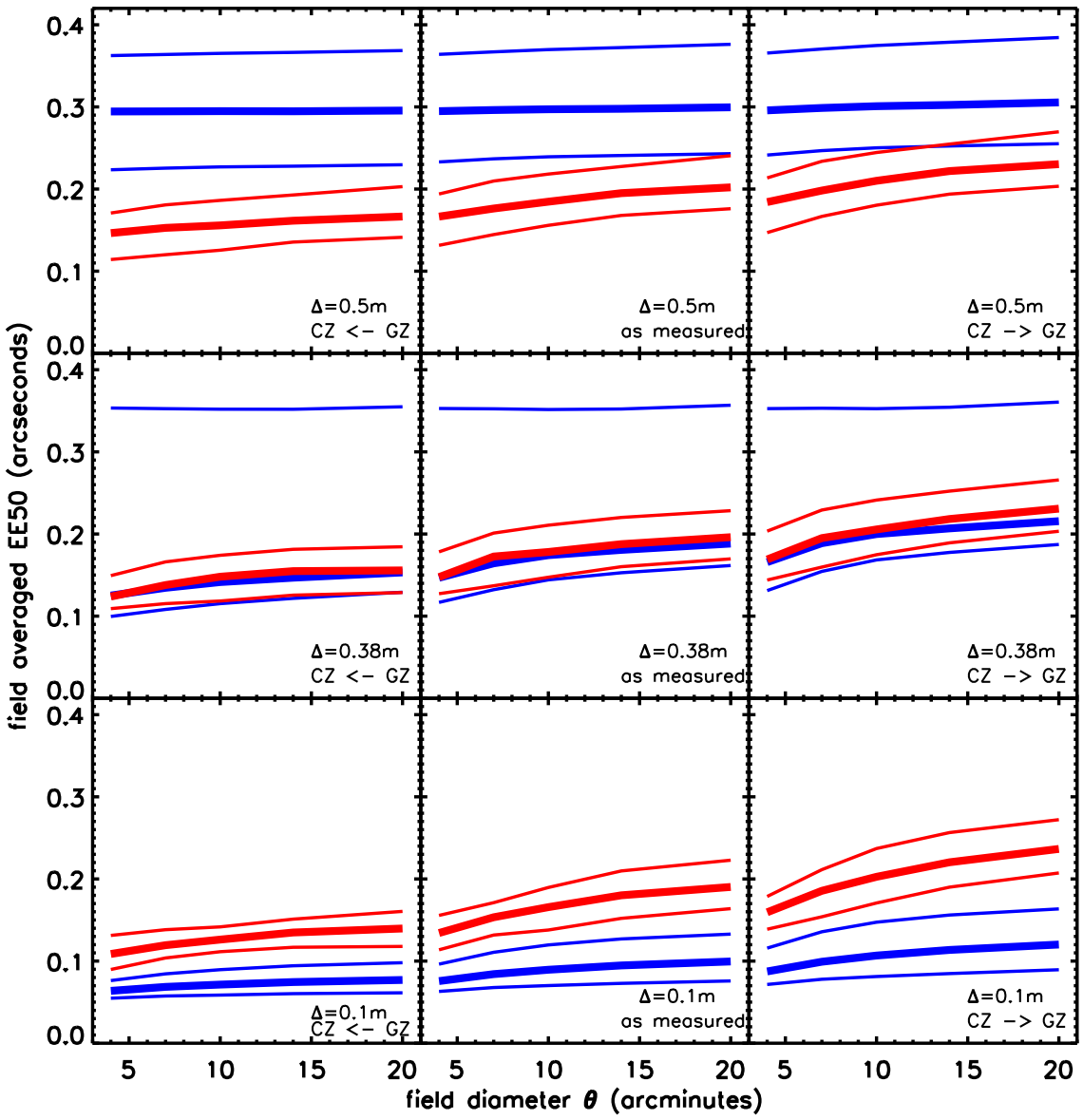

FIG. 3. The field averaged radius of 50% encircled energy on PSFs at $1.25\mu m$, plotted as a function of the GLAO field of view.

Acknowledgments.

We would like to thank the authors of Lawrence et al. (2004) for providing their SODAR+MASS data. This work has been funded by the Marie Curie Excellence Grant (ForOT) - MEXT - CT - 2005 - 023878

References

Agabi, A., E. Aristidi, M. Azouit, E. Fossat, F. Martin, T. Sadibekova, J. Vernin, and A. Ziad, 2006: First Whole Atmosphere Nighttime Seeing Measurements at Dome C, Antarctica. *PASP*, **118**, 344–348, doi:10.1086/498728, arXiv:astro-ph/0510418.

Andersen, D. R., J. Stoesz, S. Morris, M. Lloyd-Hart, D. Crampton, T. Butterley, B. Ellerbroek, L. Jolissaint, N. M. Milton, R. Myers, K. Szeto, A. Tokovinin, J.-P. Véran, and R. Wilson, 2006: Performance Modeling of a Wide-Field Ground-Layer Adaptive Optics System. *PASP*, **118**, 1574–1590, doi:10.1086/509266, arXiv:astro-ph/0610097.

Egner, S. E., E. Masciadri, and D. McKenna, 2007: Generalized SCIDAR measurements at Mt. Graham. *PASP accepted*.

Egner, S. E., E. Masciadri, D. McKenna, and T. M. Herbst, 2006: Beyond conventional G-SCIDAR: the ground-layer in high vertical resolution. *Advances in Adaptive Optics II. Edited by Ellerbroek, Brent L.; Bonaccini Calia, Domenico. Proceedings of the SPIE, Volume 6272, pp. 627256 (2006).*, Presented at the Society of Photo-Optical Instrumentation Engineers (SPIE) Conference, Vol. 6272, doi:10.1117/12.671380.

Jolissaint, L., J.-P. Véran, and R. Conan, 2006: Analytical modeling of adaptive optics: foundations of the phase spatial power spectrum approach. *Optical Society of America Journal A*, **23**, 382–394.

Lawrence, J. S., M. C. B. Ashley, A. Tokovinin, and T. Travouillon, 2004: Exceptional astronomical seeing conditions above Dome C in Antarctica. , **431**, 278–281, doi:10.1038/nature02929.

Tokovinin, A., 2004: Seeing Improvement with Ground-Layer Adaptive Optics. *PASP*, **116**, 941–951, doi:10.1086/424805.

Tokovinin, A. and T. Travouillon, 2006: Model of optical turbulence profile at Cerro Pachón. *MNRAS*, **365**, 1235–1242, doi:10.1111/j.1365-2966.2005.09813.x.

Tokovinin, A., J. Vernin, A. Ziad, and M. Chun, 2005: Optical Turbulence Profiles at Mauna Kea Measured by MASS and SCIDAR. *PASP*, **117**, 395–400, doi:10.1086/428930.

Adaptive optics using multiple guide stars

Christoph Baranec*, Michael Lloyd-Hart, N. Mark Milton,
Thomas Stalcup, Miguel Snyder, and Roger Angel
Center for Astronomical Adaptive Optics,
The University of Arizona, Tucson, Arizona

ABSTRACT

Over the past several years, experiments in adaptive optics (AO) involving multiple natural and laser guide stars have been carried out by our group at the 1.55 m Kuiper telescope and the 6.5 m MMT telescope. From open-loop data we have calculated the performance gains anticipated from ground layer adaptive optics and laser tomography adaptive optics. For the first time, we expect to close the AO control loop around five laser beacons in July 2007 where we predict image quality of <0.2" FWHM in K band over a 2' field. The work here is intended to be both its own productive scientific endeavor for the MMT, but also as a proof of concept for the advanced AO systems designed to support observing at Large Binocular Telescope and the future Giant Magellan Telescope.

*Corresponding author address: Christoph Baranec, Center for Astronomical Adaptive Optics, 933 N. Cherry Ave., Tucson, AZ, 85721
E-mail: baranec@as.arizona.edu

1. Open-loop NGS ground-layer AO

Observational tests of open-loop ground-layer wavefront recovery (GLAO) have been made using a constellation of four natural guide stars (NGS) at the 1.55 m Kuiper telescope in Arizona (Baranec, et al. 2007). The wavefronts from the four stars were measured simultaneously on a Shack-Hartmann wavefront sensor (WFS). The WFS placed a 5 by 5 array of square subapertures across the pupil of the telescope, allowing for wavefront reconstruction up to the fifth radial Zernike order. We found that the wavefront aberration in each star can be roughly halved by subtracting the average of the wavefronts from the other three stars. Wavefront correction on this basis leads to a reduction in width of the seeing-limited stellar image by up to a factor of 3, with image sharpening effective from the visible to near infrared wavelengths over a field of at least 2 arc minutes. Figure 1 shows the FWHM of ground-layer corrected and seeing limited simulated PSFs as a function of wavelength for stars located from 17 to 85 arc seconds away from the center of the GLAO constellation.

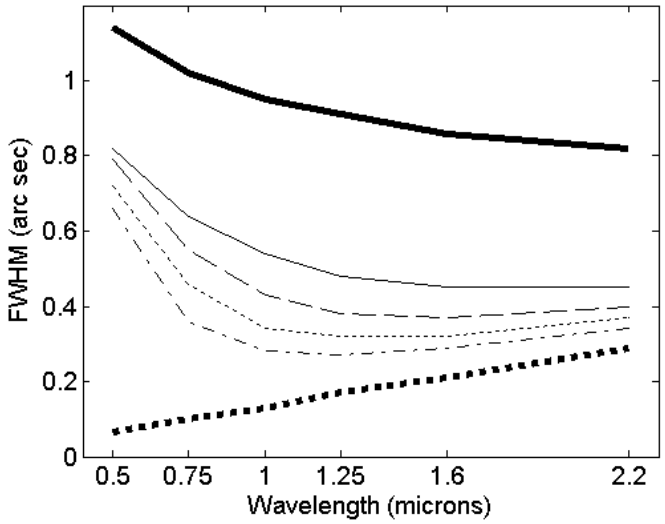

Fig. 1. FWHM vs. wavelength of simulated PSFs. The seeing-limited PSF is the thick solid line; the GLAO-corrected PSFs are the thin lines showing a star 17 arc sec (solid line), 65 arc sec (dot-dashed line), 85 arc sec (dotted line), and 113 arc sec (dashed line) from the center of the GLAO constellation. The diffraction-limited PSF is the thick dashed line.

2. MMT multiple laser guide star AO system

The MMT's multiple laser guide star (LGS) system is comprised of four main components: the laser beam projector, a Cassegrain mounted wavefront sensor, a real-time reconstructor computer and the adaptive secondary mirror.

The laser beam projector has been in use since June 2004 (Stalcup et al. 2004) and has supported several open-loop observing runs. The system projects five Rayleigh LGS from behind the secondary of the MMT into a regular pentagon of beacons on the sky with a radius of 60 arc seconds. These beacons are dynamically refocused in the return optics (Georges et al. 2003) between an elevation of 20 to 29 km above the telescope to increase the photon return.

For a more thorough description of the WFS instrument, see Lloyd-Hart et al. 2006b. Although the basic design is similar to that used in previously published experiments, we have made substantial improvements to our system, increasing our throughput and SNR, allowing us to run our LGS WFS at a faster 460+ frames per second. In addition, three other cameras are installed in the instrument: a fast tip-tilt camera with a searchable 2 arc minute field using an electron multiplying L3 CCD, a standard 12 x 12 natural guide star Shack-Hartmann wavefront sensor which can be used for open-loop testing or for low bandwidth wavefront sensing, and a wide field video camera used for acquisition.

The real-time reconstructor reads the laser wavefront sensor and tilt sensor and computes corrections to be applied to the adaptive secondary mirror, which has been used routinely over the past several years to support the MMT's NGS AO system.

3. Open-loop LGS ground-layer AO

In earlier work with the prototype system over the past 2 years, simultaneous real-time data streams from the LGS and NGS sensors have been captured. Analyses of the open-loop data have been very encouraging. In brief, the instantaneous corrected stellar wavefront is computed as the difference between the reconstructed NGS wavefront and the average wavefront derived from the LGS measurements, with the global image motion taken from the tilt camera. Integrated point-spread functions (PSFs) have been calculated from continuous 60 s sequences of data under a variety of atmospheric and instrumental conditions.

In an experiment at the MMT in June 2005 (Lloyd-Hart, et al. 2006a), the telescope was steered so as to collect data with a bright NGS at several points across a radius of the LGS constellation. GLAO wavefront corrections of Zernike orders 2 through 6 were calculated from the LGS, assuming a temporal lag of 0.02 s. To the corrected stellar wavefronts were added random amounts of Zernike orders 7 through 100 drawn from an uncorrected Kolmogorov distribution to account for the unsensed higher order modes. Synthetic residual tilt errors were also added assuming that global image motion was measured from a NGS at the center of the field, with noise and anisoplanatic errors determined empirically from separate observations of a five star asterism on a wide field tilt camera. Table 1 summarizes a number of measures of image quality calculated from the resulting PSFs. Encircled energy plots for the same PSFs are shown in Figure 2.

TABLE 1. Radially averaged quality metrics computed for synthetic GLAO PSFs from open-loop wavefront data. Results are shown for field angles of 5, 25, and 50 arc sec for in both H (λ = 1.6 μm) and K (λ = 2.2 μm) bands.

Metric	Field angle (″)						Diffraction limit		Seeing limit (r_0 = 22.5cm)	
	5		25		50					
	H	K	H	K	H	K	H	K	H	K
FWHM (″)	0.10	0.10	0.13	0.12	0.14	0.13	0.052	0.070	0.36	0.34
θ_{50}	0.21	0.13	0.21	0.14	0.21	0.14	0.048	0.064	0.27	0.25
θ_{80}	0.51	0.46	0.51	0.47	0.51	0.47	0.095	0.13	0.52	0.51
Peak intensity	0.082	0.21	0.056	0.16	0.55	0.14	1.0	1.0	0.015	0.028

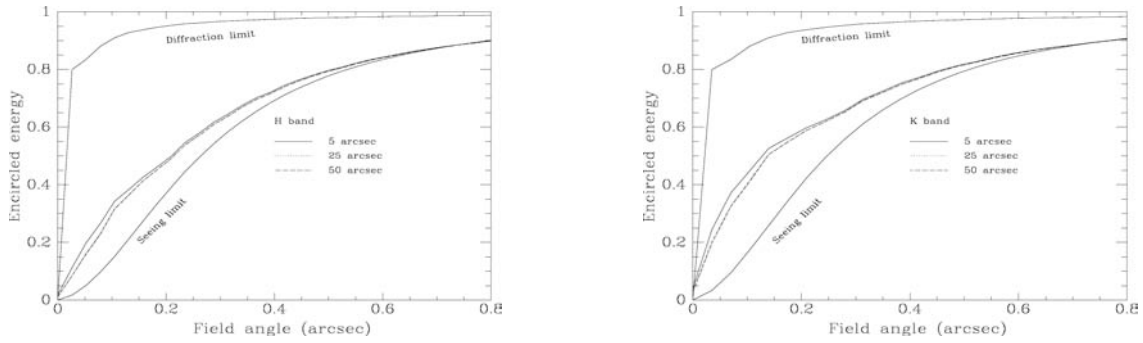

Fig. 2. Encircled energy graphs for synthetic GLAO PSFs in the H (left) and K (right) bands. Plots are shown for three different radii within the LGS constellation, though the results for 25 and 50 arc sec radii are almost indistinguishable. All assume that a single tip-tilt star is used at the center of the LGS constellation. Also shown for comparison are curves for PSFs at the diffraction limit and the seeing limit. The latter assumes the mean value of r_0 (22.5 cm at 500 nm) at the time of the observations, and no additional contribution from telescope vibrations or tracking errors.

Analysis of the average power in the Zernike modes of the NGS wavefronts shows that the mean r_0 was 22.5 cm at $\lambda =$ 500 nm with an outer scale L_0 of 19 m (Chassat 1992). Even though the seeing was already excellent, GLAO further improved the resolution, to within about a factor 2 of the diffraction limit in K band ($\lambda =$ 2.2 μm). The 50% encircled energy radius θ_{50} also saw substantial improvement, particularly in the K band. Furthermore, the variability of the PSF over the explored field, with a radius of 50 arc sec, is remarkably small.

While these results by themselves are encouraging, we find that the value of GLAO is not restricted to periods when the seeing is already good. Unlike conventional AO where the diffraction limit is the goal, the more modest reach of GLAO is also more robust to adverse atmospheric conditions. Data from a period when the value of r_0 was 10.1 cm, approximately half the value for the results above and at the site's 75th percentile, show that improvement of the K band PSF to FWHM of 0.2 arc sec will still be possible under such conditions (Lloyd-Hart, et al. 2005).

4. Open-loop LGS tomographic AO

Results of open-loop tomographic wavefront sensing (LTAO) have been analyzed using the same data used to predict GLAO correction. A full description of the tomographic algorithm used here is found in Baranec et al. 2006 and Lloyd-Hart, et al. 2006a. The RMS residual wavefront aberration after correction with both the GLAO and LTAO techniques over Zernike orders 2 through 8 were calculated. Figure 3 shows two examples of the RMS residual wavefront error as a function of time over four seconds. The data on the left represents a set taken in June 2005, with seeing parameters: $r_0 = 14.8$ cm at 500 nm wavelength, $L_0 = 12$ m. Data on the right represents a set taken in April 2006, with seeing parameters: $r_0 = 18.0$ cm, $L_0 = 13.5$ m. The RMS residual errors for each set are

presented in table 2. Notice that there is improvement in the floor of the tomographic residual in the most recent data. This is a measure of the information content in our recovered wavefront estimates, and the improvement is due in part to improved alignment of optics, increased throughput and faster frame rate. The residual is now dominated by the fitting error of our chosen LGS and NGS Shack-Hartmann WFSs.

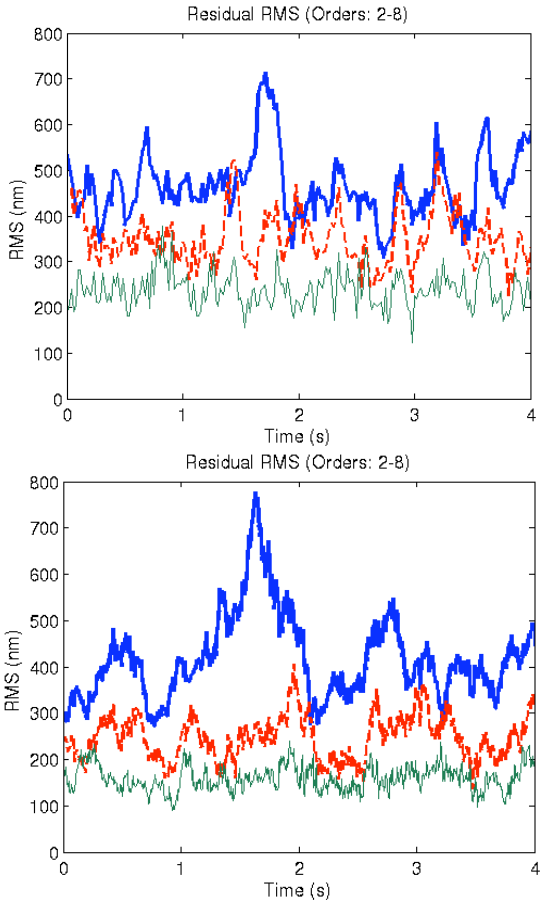

Fig 3. An example of the RMS residual error over Zernike orders 2 through 8 for an uncorrected stellar wavefront (thick solid), after GLAO correction (dashed) and after LTAO correction (thin solid). Data from June 2005 are presented in the top panel and data from April 2006 are presented in the bottom panel.

TABLE 2. Residual RMS wavefront errors for the data sets presented in figure 3.

	June 2005	April 2006
Uncorrected	511 nm	448 nm
GLAO Corrected	360 nm	249 nm
LTAO Corrected (with a single tip/tilt star)	259 nm	172 nm
LTAO Corrected (with 3 tip/tilt field stars)	243 nm	N/A

From the residual wavefront errors after ground layer and tomographic estimation at each time step, a synthetic corrected PSF can be calculated. These are computed for a source on axis in K band from a 60 s continuous data sequence from June 2005 recorded in seeing conditions of r_0 = 14.7 cm at 500 nm wavelength. The reconstruction estimated the first 44 modes of the star's wavefront, now including tip-tilt. The integrated PSFs include uncompensated Zernike modes from orders 9 through 100 drawn from a Kolmogorov distribution.

Table 3 below shows the corresponding widths and relative peak intensities for the time averaged PSFs, and for PSFs computed similarly in the J band and H band. With tomographic correction, the K band is corrected almost to the diffraction limit, with a 15-fold increase in peak intensity to a Strehl ratio of 16%. This relatively low order reconstruction is insufficient to achieve the diffraction limit at the shorter wavelengths, but the improvement in resolution and peak brightness are both substantial.

TABLE 3**.** Image quality metrics at J, H and K.

Metric	Waveband	Uncorrected	GLAO	LTAO	Diffraction Limit
FWHM (arcsec)	J	0.774	0.378	0.113	0.040
	H	0.683	0.171	0.086	0.052
	K	0.553	0.125	0.089	0.070
Relative peak Intensity	J	1.0	2.0	3.9	498
	H	1.0	3.7	9.4	239
	K	1.0	7.0	15.0	92

5. Current work

The next step in our LGS AO program at the MMT is to demonstrate a closed-loop GLAO system. Our first attempt occurred during a six night run at the end of December, but due to inclement weather, there was very little usable sky time and we were unable to close the GLAO loop. Nevertheless, we were able to use the time effectively to do a full systems test. We were able to spend additional time on remaining minor hardware and software issues, as well as calibrate the orientation of the wavefront sensors to the deformable secondary mirror. A second attempt occurred in early April. We were able to close the tip/tilt loop, but found the full LGS loop to be unstable due to a programmatic error and are currently investigating the problem. We will be doing off telescope closed-loop tests with a newly redesigned test stand to hold the MMT's deformable secondary in an optical setup with our wavefront sensor to validate the loop in early June.

Another four night telescope run is planned for the beginning of July where we expect to collect the first set of ground-layer corrected images using two science cameras, PISCES (McCarthy et al. 2001) and Clio (Sivanandam et al. 2006). We intend to explore the image quality, stability and sensitivity of GLAO correction as a function of waveband. PISCES is a 1-2.5 μm imager with a field of view of 1.9 arc min, at a scale of 0.11 arc sec/pixel. This is well matched to the expected FWHM performance of the GLAO corrected field and will be able to examine PSF non-uniformity and temporal stability across a wide field. Clio is a 1–5 μm imaging camera optimized for observing at

3.5 and 4.8 μm with a field of view of 15 ×12 arc sec and Nyquist sampling at 3.5 μm (0.048 arc sec/pixel) which will be able to more fully characterize the PSF. In these thermal wavelengths we expect to see a Strehl ratio of 30-40% in median seeing conditions. Imaging with Clio will be of particular interest when observing faint (V>13) targets.

References

Baranec, C., Lloyd-Hart, M., & Milton, N. M., 2007: Ground-layer wavefront reconstruction from multiple natural guide stars. *Astrophysical Journal*, **661**, 1332-1338.

Baranec, C., Lloyd-Hart, M., Milton, N. M., Stalcup, T., Snyder, M., & Angel, R., 2006.: Tomographic reconstruction of stellar wavefronts from multiple laser guide stars. *Proc. SPIE*, **6272**.

Chassat, F. 1992: Ph. D. Thesis (Paris-Sud)

Georges, J., Stalcup, T., Angel, R., & Mallik, P., 2003: Field tests of dynamic refocus of Rayleigh laser beacons. *Proc. SPIE,* **5169**.

Lloyd-Hart, M., Baranec, C., Milton, N. M., Snyder, M., Stalcup, T., & Angel, J. R. P., 2006a: Experimental results of ground-layer and tomographic reconstruction from multiple laser guide stars. *Optics Express*, **14**, 7541-7551.

Lloyd-Hart, M., Baranec, C., Milton, N. M., Stalcup, T., Snyder, M., Putnam, N., & Angel, J. R. P., 2005: First tests of wavefront sensing with a constellation of laser guide beacons. *Astrophysical Journal*, **634**, 679-686.

Lloyd-Hart, M., Stalcup, T., Baranec, C., Milton, N. M., Rademacher, M., Snyder, M., Meyer, M., & Eisenstein, D., 2006b: Scientific goals for the MMT's multi-laser-guided adaptive optics. *Proc. SPIE*, **6272**.

McCarthy, D., Ge, J., Hinz, J., Finn, R. A., & deJong, D. S., 2001: PISCES: A Wide-Field, 1-2.5 mum Camera for Large-Aperture Telescopes. *Publications of the Astronomical Society of the Pacific*, **113**, 353-361.

Sivanandam, S., Hinz, P., Heinze, A., Freed, M., & Breuninger, A., 2006: Clio: a 3-5 micron AO planet-finding camera. *Proc. SPIE*, **6269**.

Stalcup, T., Georges, J., Snyder, M., Baranec, C., Putnam, N., Milton, M., Angel, R., & Lloyd-Hart., M., Field tests of wavefront sensing with multiple Rayleigh laser guide stars and dynamic refocus. *Proc. SPIE*, **5490**.

Some measurements of the short term variability of $\mathbf{r}_0$

L. William Bradford* Lewis C. Roberts, Jr.
the Boeing Company, Kihei, Hawaii

1. Introduction

For the observational astronomer, the implications of atmospheric turbulence are evident in any long exposure image of a point source: the image is not the Airy pattern described by diffraction theory , but a rather more extended blur of roughly Gaussian shape King (1971). The measure of the "seeing" was the full width across the image whe Fried advanced the statistical models of the effects of turbulence on light propagating down through the atmosphere Fried (1965, 1966). Out of this work came the identification of a particular spatial coherence length scale r_0. A later analysis Korff (1973) discussed the relation of the FWHM to r_0. Later, Sarazin and Roddier (1990) cited a numerical estimation that led to the oft-used result

$$FWHM = \frac{C\lambda}{r_0}, \tag{1}$$

where $C = 0.98$. For convenience we have set $C = 1$.

Fried later introduced the differential angle-of-arrival method of estimating r_0, which can be used to make rapid sequences of measurements of the differences in wavefront slope between pairs of apertures Fried (1975).

2. Data Collection and Processing

The Visible Imager is the current science camera for the Advanced Electro-Optical System (AEOS) telescope's adaptive optics (AO) system Roberts and Neyman (2002). In 2004–2006, we collected about 10000 images of bright ($M_v \approx 2$ to $M_v \approx 4$) stars using a filter centered at 850nm. Observed stars were within 20° of zenith. Data were collected with exposure times such that images did not saturate, with no exposures shorter than 0.5 s or longer than 2 s. The images were collected open loop (tip/tilt and AO control loops off), so images needed to be centered in the 10 arcsecond field of view. Typically a set of 100-120 images were taken successively. From the this data, we have selected 3209 one-second exposures, and 2495 two-second exposures.

Images were automatically processed using a MATLAB script that gives an estimate of FWHM even in poor seeing. Values of r_0 are computed for each FWHM. From those we computed time series, power spectra, and histograms of the data.

3. Analysis of the Data

In Figure 1, we show some example time series of r_0 from long exposure images for poor, moderate and excellent seeing conditions. We also show a small segment of a time series of

*Corresponding author address: the Boeing Company, 535 Lipoa Pkwy, Suite 200, Kihei HI 96753. lawrence.w.bradford@boeing.com

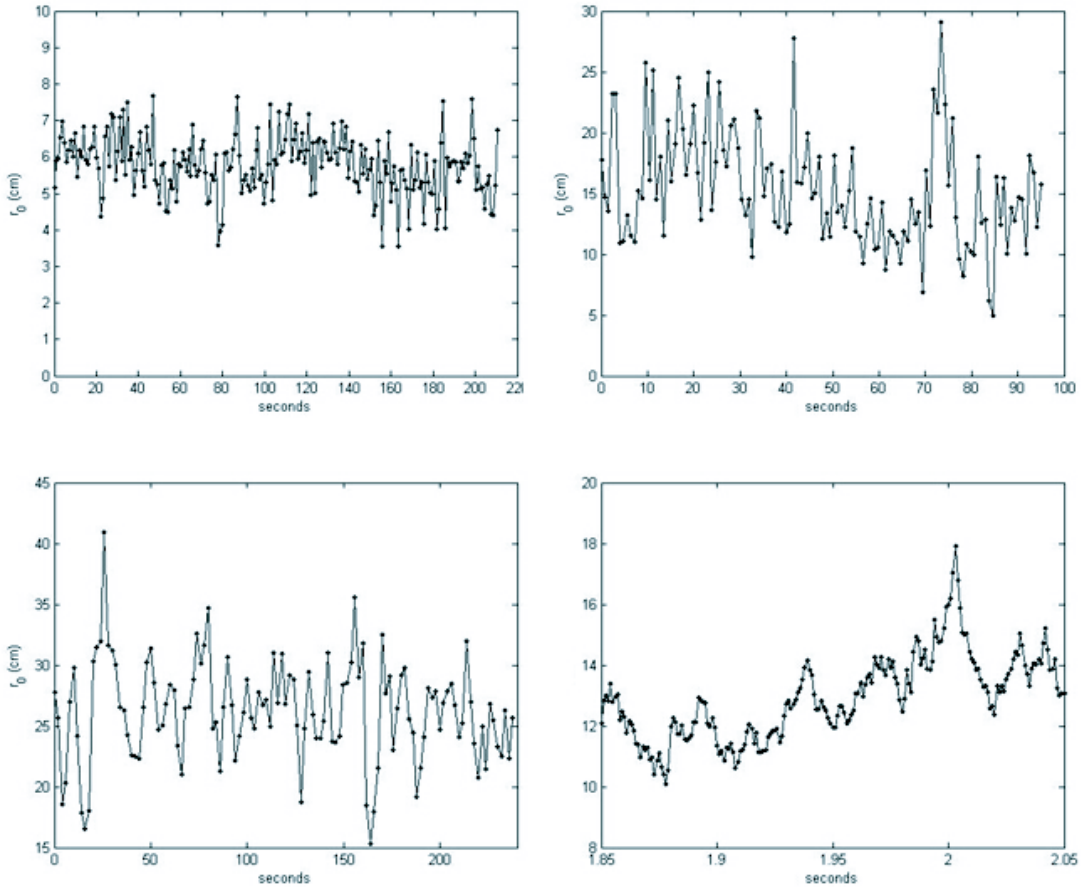

FIG. 1. Upper left: Sequence of r_0s computed from one second exposures using the AEOS Visible Imager science camera. The median r_0=5.8 cm. Upper right: Sequence of r_0s computed from 0.8 second exposures. The median r_0 is 14.6 cm, which is very close to the site median. Lower left: Sequence of r_0s computed from two second exposures. The seeing shown here is some of the best seen in our data. Significant variability is seen in the data set which has a median r_0=26.5 cm. Lower right: A section of r_0 derived from AEOS wave front sensor slope measurements processed by a differential angle-of-arrival code. The sensor frame rate was 1 KHz. Even at these short time scales, significant variability exists. Note trends in values and low noise. The low noise reflects the large number of differential angle of arrival pairs used to calculate r_0. Data has been corrected to a wavelength of 0.5μm and zenith.

r_0 calculated from Shack-Hartmann wavefront sensor data using differential angle of arrival. We find that qualitatively similar variations of r_0 occur on both time scales.

Although not true in every instance, we find that when r_0 is low, the measured values tend to stay low. When r_0 is high, there can be significant variability. This variability does not seem to represent noise in the measurement however. Examination of the time series shows that while there are instances of significant swings in value from one measurement to the next, there are many instances of trends in the measurements. We feel that the measurements reflect true variations in the seeing on the time scale of seconds.

Another way of looking at the variability is shown in Figures 2. Here we have plotted change

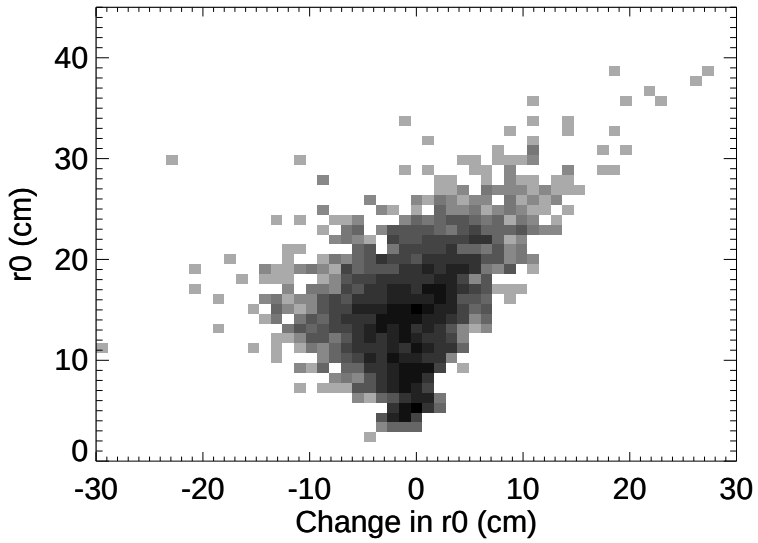

FIG. 2. Change in r_0 between a one second measurement and its successor versus the value of r_0 for the first measurement. Color represents the number of data points plotted. The data show that more variability in r_0 is seen with larger values of r_0, while low values of $r_0$are less likely to change significantly. A skew toward positive changes in r_0 results from the data being bounded by r_0=0 cm. Data has been corrected to a wavelength of 0.5μm and zenith.

in r_0 from one frame to the next on the horizontal axis, and the value of r_0 for the first of the two frames on the vertical axis. Number of measurements for that r_0 is represented by the intensity. There are many values of r_0 between 10 cm and 20 cm, fewer at higher and lower values. Also more values of the subsequent r_0 measurement are close to the first measurement. Therefore the the density of points is high. As the difference in r_0 increases, fewer points are to be found. There is also a bias in that there is a limit on the amount of negative change in r_0 because r_0 cannot be less than zero. More data would improve the utility of the plot.

4. Conclusions and Implications

We have found that r_0 can vary significantly over a period of seconds to minutes. To be sure, this is not a new result. Some of the data described in Walters and Bradford (1997) contained measurements of r_0 at a relatively fine temporal resolution with some data sets, particularly at good seeing sites, showing similar large jumps. However, our analysis of the statistics of changes in r_0 from one measurement to the next adds to the knowledge base of r_0 variability.

Future publications will demonstrate that significant variability exists on much shorter times scales as shown in Figure 1 which shows some measurements of r_0 made using differential angle of arrival measurements with the AEOS AO System's Shack-Hartmann wavefront sensor.

Acknowledgments.

This research was funded by the Air Force Office of Scientific Research under contracts F29601-00-D-0204 and FA9451-05-C-0257.

References

Fried, D. L., 1965: Statistics of a geometric representation of wavefront distortion. *J. Opt. Soc. Am.*, **55 (10)**, 1427–1435.

———, 1966: Optical resolution through a randomly inhomogeneous medium for very long and very short exposures. *J. Opt. Soc. Am.*, **56 (10)**, 1372–1379.

———, 1975: Differential angle of arrival: Theory, evaluation, and measurement feasibility. *Radio Sci.*, **10 (1)**, 71–76.

King, I. R., 1971: The profile of a star image. *Pub. A.S.P.*, **89**, 199–200.

Korff, D., 1973: Analysis of a method for obtaining near-diffraction-limited information in the presence of atmospheric turbulence. *J. Opt. Soc. Am.*, **63 (8)**, 971–980.

Roberts, L., Jr. and C. R. Neyman, 2002: Characterization of the AEOS adaptive optics system. *Pub. Astro. Society of the Pacific*, **114**, 1260.

Sarazin, M. and F. Roddier, 1990: The ESO differential image motion monitor. *Astron. Astrophys.*, **227**, 294–300.

Walters, D. and L. Bradford, 1997: Measurements of r_0 and θ_0: two decades and 18 sites. *Appl. Opt.*, **36**, 7876–7886.

Two Applications of Turbulence Characterization that Improve Deep AO Imaging with Laser

Eric Steinbring*, Jason Melbourne, Anne Metevier and David Koo
Herzberg Institute of Astrophysics/NRC, CfAO

ABSTRACT

Laser AO observations are now becoming routine. This is a huge boon to extragalactic astronomy, bringing to bear 8 to 10-m-class telescopes on faint high-redshift galaxies that are otherwise unreachable from the ground. The Center for Adaptive Optics Treasury Survey (CATS) has exploited this. It employs Keck laser AO to obtain deep (~1 hr) NIR exposures over relatively large fields (~50" X 50") already imaged with HST. The PSF is of comparable sharpness to HST in the optical, and even better in the NIR. But to capitalize on this the PSF must be well characterized. Two techniques we have employed are presented. One requires calibration observations of a globular cluster taken during the night, and the other utilizes independent turbulence profile information provided by the nearby TMT site testing tower. How these translate into improved galaxy photometry is discussed.

*Corresponding author address: Eric Steinbring, Herzberg Institute of Astrophysics/NRC, CfAO.
E-mail: Eric.Steinbring@nrc-cnrc.gc.ca

SLODAR Turbulence Profiling

Richard Wilson* and Timothy Butterley
University of Durham, Department of Physics, South Road, Durham DH1 3LE, UK

ABSTRACT

SLODAR (SLOpe Detection And Ranging) is an optical method for profiling of the altitude and velocity of atmospheric turbulence, by using a telescope equipped with a Shack-Hartmann wavefront sensor to observe double stars. Prototype stand-alone (small telescope) SLODAR systems have been deployed at Cerro Paranal and Mauna Kea for detailed characterization of ground-layer turbulence. Future enhancements will include full automation of the stand-alone SLODAR monitors, and detailed characterization of atmospheric turbulence via high order SLODAR wavefront sensing on large telescopes.

*Corresponding author address: Richard Wilson, University of Durham, Department of Physics, South Road, Durham DH1 3LE, UK
E-mail: r.w.wilson@durham.ac.uk

2. SLODAR Turbulence Profiling

SLODAR (SLOpe Detection And Ranging) (Wilson, 2003) is an optical method for profiling of the strength, altitude and velocity of atmospheric turbulence. A telescope equipped with a Shack-Hartmann wavefront sensor (WFS) is used to observe a double star target so that two sets of WFS spots are imaged on to the detector. The WFS spot patterns may be interleaved (for a target with narrow separation) or fully separated (for a wider target). Each of the target stars effectively projects a copy of the aberration produced by the turbulent layers onto the ground, with a separation that depends on the altitude of the layer and the separation angle of the double star. The spatial cross-covariance of the WFS slope (centroid) data is calculated for each star. Then for each turbulent layer there is a corresponding peak in the time-averaged covariance function at a spatial offset proportional to the layer altitude. The shape of the peaks in the cross-correlation - the 'response function' of the SLODAR system - has only a weak dependence on the layer altitude. Hence recovery of the Cn2(h) profile can be carried out via a simple least-squares fit of the theoretical response functions (Butterley, Wilson & Sarazin, 2006).

The resolution in altitude of the SLODAR system depends on the sub-aperture size of the WFS and the angular separation of the double star. Hence the system can be optimized to profile the whole atmosphere (using narrow targets), or to profile the low altitude turbulence in detail (using a wide target). For a given target separation the maximum altitude for profiling is proportional to the maximum spatial offset measured, and hence the telescope aperture diameter. However the minimum usable size of the sub-apertures, and hence the altitude resolution, is limited by signal requirements and scintillation effects to approx 5cm.

The translational (wind) velocity of the turbulent layers as a function of altitude can be determined from the spatio-temporal cross-correlation, by measuring the displacement of the peaks in the cross-correlation when a time offset is introduced between the WFS data streams for the two target stars.

3. Existing Systems

The SLODAR technique has been applied to large telescopes (Wilson 2003, Lambert et al. 2006, Wang et al. 2007), and also developed as a stand-alone turbulence profiler based on small telescopes (Wilson et al. 2005). Durham CfAI and ESO implemented a prototype small telescope system for characterization of the ground-layer (below 1km) turbulence at the Paranal observatory (figures 1 and 2) (Sarazin et al. 2007). The instrument employs an electron-multiplication CCD camera to permit high speed wavefront sensing with good SNR at low photon rates.

A similar instrument has been installed at the Mauna Kea observatory as part of a study to characterize the ground-layer turbulence at the site, funded by the Gemini observatory and carried out by a collaboration of the University of Hawaii, University of Durham and UNAM (Chun et al. 2007). This system can also be configured as a LOLAS (Low Layer SCIDAR) instrument (Avila et al. 2007).

Fig. 1: Left: Durham/ESO prototype SLODAR System. Right: The SLODAR instrument transferred to an Astelco NTM100 mount and tower/enclosure (E-ELT site testing equipment) at Cerro Paranal for a test of fully robotic operation (2007).

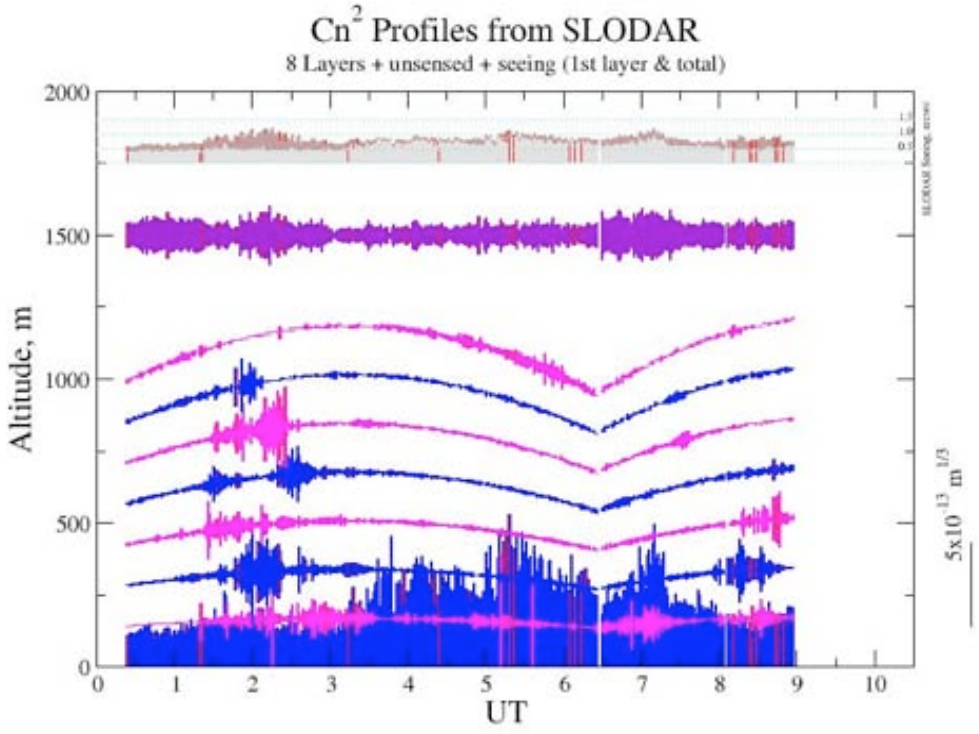

Fig. 2 Example SLODAR turbulence profile data for Paranal, 22 March 2005

4. Future Plans

The prototype SLODAR stand-alone monitors are largely automated in operation but require operator intervention for target acquisition, startup and shutdown. Enhancements are being made to permit unsupervised (robotic) operation. This requires improvements to the pointing accuracy and stability of the telescope mount (see figure 1) and to the stability of the telescope optical alignment. Modifications to the optical configuration of the WFS will also permit straightforward interchange between whole atmosphere profiling (narrow targets) and GL profiling (wide targets), without any change to the optical configuration. It may also be possible to exploit measurements of the fluctuation of intensity of the WFS spots due to scintillation - as well as the phase slope - to increase the resolution and accuracy for profiling to high altitudes, and to improve the performance of the system in the presence of scintillation (Vedrenne 2006).

Measurements with the SLODAR systems at the Cerro Paranal and Mauna Kea observatories have shown that the thickness of the ground-layer is often not resolved by the instrument - i.e. a strong signal is observed only in the first resolution element in altitude. This indicates that the ground layer is frequently less than ~50m thick. The predicted performance of AO correction for an ELT depends critically on the detailed structure of the ground/surface layer turbulence, so that measurements with higher resolution are required. A SLODAR monitor with increased field-of-view will be implemented, to accept very wide double star targets (~10 arc-minutes) and permit profiling of the ground layer with a resolution of ~10m in altitude.

Durham CfAI also plans to deploy a very high order WFS (~40x40 sub-apertures) on a large telescope (2m or larger) for high-resolution SLODAR profiling. In particular, by increasing the number of spatial resolution elements, it will be possible to explore the temporal evolution of individual turbulent layers in detail: e.g. layer wind velocities and velocity dispersion, and the validity of Taylor 'frozen flow' for layers at different altitudes.

References

R. Avila, J.-L. Aviles, R. Wilson, M. Chun, S. Cuevas, A. Farah, 2007: Low Layer SCIDAR: a turbulence profiler for the first kilometer with very high altitude-resolution. *This meeting.*

T. Butterley, R. Wilson, and M. Sarazin, 2006: Determination of the profile of atmospheric optical turbulence strength from SLODAR data. *MNRAS* **369**(2): 835.

M. Chun, R. Wilson and R. Avila, 2007: The Mauna Kea ground-layer characterization campaign. *This meeting.*

A. Lambert, C. Jenkins and M. Goodwin, 2006: Turbulence profiling using extended objects for slope detection and ranging (SLODAR). *Proc. SPIE* **6316**.

M. Sarazin, T. Butterley, J. Navarrete, R. Wilson, 2007: Assembling composite vertical atmospheric turbulence profiles from DIMM, SLODAR and MASS contemporaneous records at Paranal. *This meeting.*

L. Wang, G. Chanan, and M. Schoeck, 2007: Atmospheric profiling using multiple adaptive optics. *This meeting*.

R. Wilson, 2003: SLODAR: measuring optical turbulence altitude with a Shack-Hartmann wavefront sensor. *MNRAS* **337**(1), 103-108.

R. Wilson, J. Bate, J.C. Guerra, N. Hubin, M. Sarazin, C. Saunter, 2004: Development of a portable SLODAR turbulence profiler. *Proc. SPIE* **5490**, 758.

N. Vedrenne, V. Michau, C. Robert and J.-M. Conan, 2006: Improvements in C_n^2 profile monitoring with a Shack-Hartmann wavefront sensor. *Proc. SPIE* **6303**.

Real-time sodium layer thickness monitoring with the Altair Laser Guide Star System

Francois Rigaut*, Damien Gratadour and Matthieu Bec
Gemini Observatory, Hawaii

ABSTRACT

While quad-cell photon counting wavefront sensors used in many astronomical adaptive optics (AO) systems allow to detect weaker sources thanks to a lower or non-existent read-out noise, the limited field of view as well as the undersampling of the spot lead to severe non-linearity issues. A quad-cell usually requires the use of the so-called centroid gains, factors that translate the intensity ratio into a physical value for the spot displacement. The value of these gains is related to the spot extent, i.e. the natural seeing and the spot elongation in the case of Laser Guide Star (LGS AO). We present a novel method for optimizing these centroid gains during the observations that allows us to estimate the best gains to apply in real-time and offers an estimate of the local sodium layer thickness as a by-product. To assess the validity of the method, we present a series of measurements acquired during few nights of Altair LGS commissioning that shows that the estimated centroid gain values are correlated to the seeing values while they are not correlated to the estimated sodium layer thickness.

*Corresponding author address: Francois Rigaut, Gemini Observatory, Hawaii.
E-mail: frigaut@gemini.edu

SESSION 3

APPROACHES FOR MODELING ATMOSPHERIC OPTICAL TURBULENCE

Optical Turbulence simulations with meso-scale models. Towards a new ground-based astronomy era

Elena Masciadri* *(invited speaker)*
Osservatorio di Arcetri, Firenze, Italy

ABSTRACT

The optical turbulence characterization made with atmospherical meso-scale models for astronomical applications is a relatively recent approach (first studies have been published in the ninety). Simulations retrieved from such models can be fundamental for the optimization of the AO techniques and characterization and selection of astronomical sites. In most cases, simulations and measurements provide complementary information on turbulence features.

The potentialities related to the numerical approach and the most fundamental scientific challenges related to meso-scale atmospheric models rely upon the possibility (1) to describe a 3D map of the CN2 in a region around a telescope, (2) to forecast the optical turbulence i.e. to know with some hours in advance the state of the turbulence conditions above an astronomical site and (3) to perform a climatology of the optical turbulence extended over decades. The forecast of the optical turbulence is a fundamental requirement for the optimization of the management of the scientific programs to be carried out at ground-based telescopes foci. Ground-based astronomy will remain competitive with respect to the space-based one only if telescopes management will be performed taking advantage of the best turbulence conditions. The future of new ground-based telescopes generation relies therefore upon the success of these studies.

No other tool of investigation with comparable potentialities can be figured out at present to achieve these 3 scientific goals.

However, these highly challenging goals are associated to an intrinsic difficulty in parameterizing a physical process such as turbulence evolving at spatial and temporal scales smaller than what usually resolved by a meso-scale model.

In this talk I will summarize the main results and progress achieved so far in this field since the ninety and I will present the most important scientific goals for the near and far future research. I will conclude with a brief presentation of the main research lines and

motivations supporting the project (FOROT) on-going at the Osservatorio Astrofisico di Arcetri (Italy).

Corresponding author address: Elena Masciadri, Osservatorio di Arcetri, Firenze, Italy.
E-mail: masciadri@arcetri.astro.it

Mesoscale numerical simulations above Antarctica: first approaches

Franck Lascaux*, Elena Masciadri , Susanna Hagelin and Jeff Stoesz
Osservatorio Astrofisico di Arcetri, Florence, Italy

ABSTRACT

Mesoscale simulations were performed in Antarctica with the use of the French non-hydrostatic model Meso-NH, in the frame of the ForOT (Forecast of Optical Turbulence above astronomical site) project. The work presented here is the first step to try to discriminate between sites having different seeing conditions above the Antarctic Plateau and towards a universal calibration of the model. Indeed we need to test which is the best configuration of the model giving the best results looking at standard meteorological parameters. The site of Dome C in Antarctica was chosen for this study because it is thought to become an astronomical site in the near future, due to its very good seeing conditions. Using wind profiles and surface temperatures observations, different configurations of the model are tested and validated. Numerical simulations have been performed, testing horizontal resolution, vertical resolution, description of the surface, and the impacts of these different configurations on the prediction of the wind and temperature above the Antarctic Plateau. We first show that the ECMWF (European Centre for Medium-range Weather Forecasts) analyses are well adapted to be used as initial and boundaries conditions for the mesoscale model. However an effort should be put in the description of the surface and the boundary layer, where discrepancies between analyses and observations are the most important. The conclusion of this work is that a high horizontal resolution together with the use of grid-nesting is crucial for a better prediction of the state of the atmosphere. More over, the initial description of the surface appears to be important.

* *Corresponding author address:* Franck Lascaux, Osservatorio Astrofisico di Arcetri - INAF, 5 Largo E. Fermi, 50125 Florence, Italy.
E-mail: lascaux@arcetri.astro.it

1. Introduction

The ForOT (Forecast of Optical Turbulence above astronomical site) project is aimed to study optical turbulence with measurements and numerical simulations. The final goal is to create an automatic system using a mesoscale meteorological model to forecast optical turbulence with a few hours in advance above astronomical sites. The meteorological model can also be used to characterize different potential astronomical sites. The idea is to help selecting the sites optimized for adaptive optics techniques.

We use the French non-hydrostatic mesoscale model named Meso-NH. It is developed jointly by the CNRM (Centre National de Recherches Météorologiques - National Center of Meteorological Researches) and the Aerology Laboratory, in Toulouse, France. It's a well established research model with hundred of users worldwide. Its physics will be implemented in the next generation of operational model of numerical weather prediction of the French meteorological center of Météo-France.

In the first section we describe the numerical setup. A short presentation of the Meso-NH model is followed by a statistical study of ECMWF analyses above Dome C in winter and summer justifying their use as initial and boundaries conditions for the model. Then in a second section we present the results of different numerical simulations predicting the short-term evolution of the state of the atmosphere in Antarctica. The goal was to find the best configuration of the mesoscale model allowing for a good weather prediction above Dome C. Finally conclusions of this work are presented in the last section.

2. Numerical setup

a. Meso-NH model configuration

Meso-NH is the French non-hydrostatic mesoscale research model. It solves a system of equation based upon the Lipps and Hemler (1982) anelastic formulation. A Gal-Chen and Sommerville (1975) coordinate on the vertical and a C-grid, in the formulation of Arakawa and Messinger (1976), for the spatial digitalization is used. The temporal scheme is an explicit three-time-level leap-frog scheme with a time filter (Asselin 1972). In one of the simulation, the two-way interactive grid-nesting technique (Stein et al. 2000) was used. with increasing horizontal mesh-sizes, the innermost domain being centered above Dome C. The 1D turbulent scheme is a 1.5 closure scheme (Cuxart et al. 2000) with the Bougeault and Lacarrère (1989) mixing lenght. The surface exchanges are computed in an externalized surface scheme (SURFEX). It includes different packages: ISBA (Noilhan and Planton 1989) for vegetation; TEB (Masson 2000) for urban area. The ECMWF analyses are used as initial and boundaries conditions. Their validity is discussed in the next part of this section.

b. Statistical study of ECMWF analyses above Dome C, Antarctica

We compare standard meteorological paramaters extracted from ECMWF analyses in winter and in summer above Dome C, Antarctica, with radiosoundings from the PNRA (Programma Nazionale Ricerche in Antartide - http://www.climantartide.it) available from March 2005 to November 2006.

Figure 1 and Figure 2 display a comparison of mean vertical profile of wind and temperature above Dome C in summer 2005 and winter 2005/2006, respectively. First it can be noticed that in winter the radiosoundings balloons reach a lower altitude than in summer (12 km in mean in

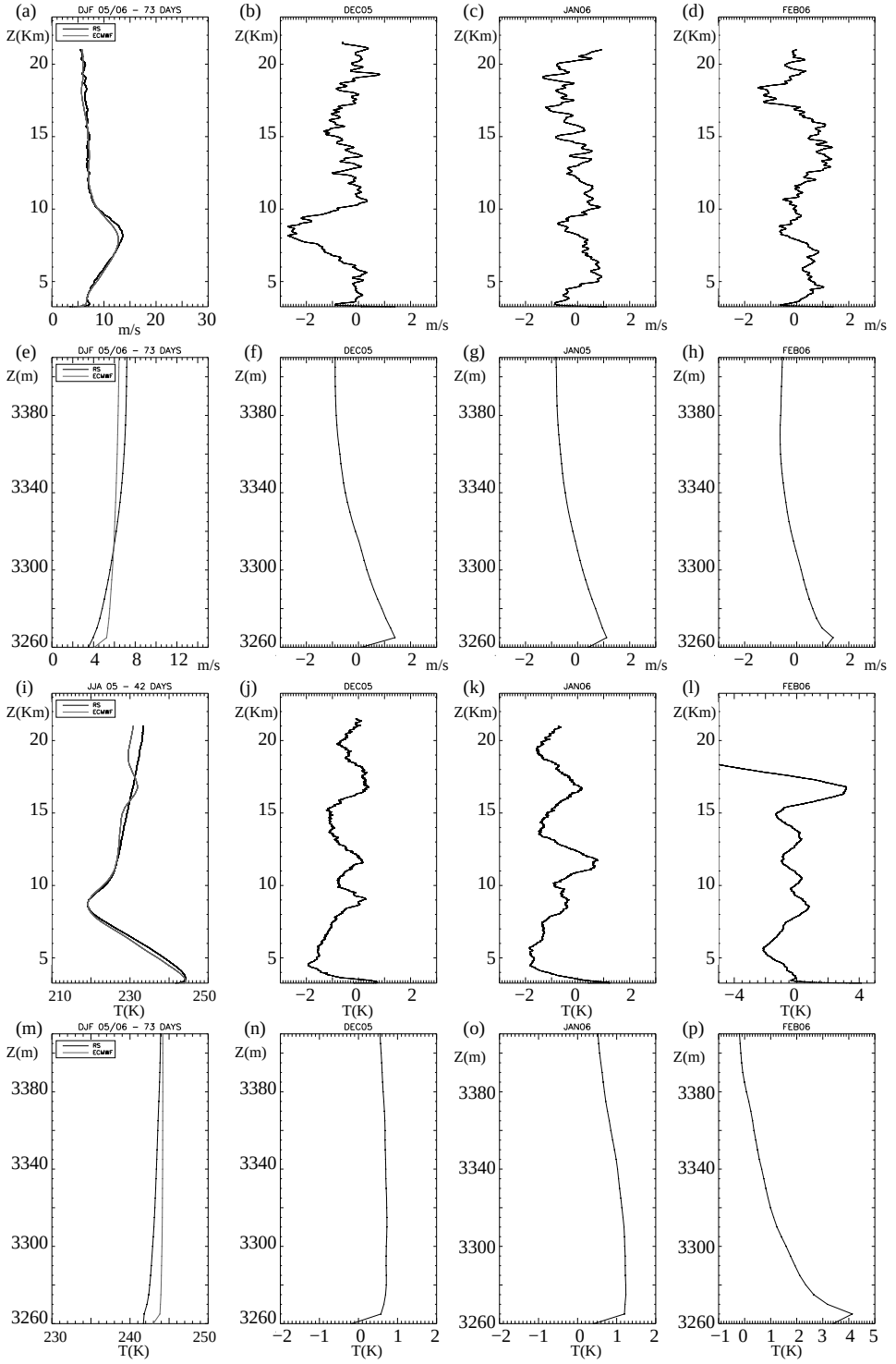

FIG. 1. Two first rows: (a)Mean vertical profiles of wind speed (in m/s) above Dome C from radiosoundings of PNRA (in grey) and ECMWF analyses (in black) in summer 2005/2006. Differences of mean vertical wind speed between ECMWF analyses and radiosoundings (b) in December 2005, (c) in January 2006 and (d) in February 2006. Profiles on (a), (b), (c) and (d) extends from the ground to 23 km. (e), (f), (g) and (h) like (a), (b), (c) and (d), respectively, but for the first 150 m. Two last rows: same as two first rows but for temperature (in °C).

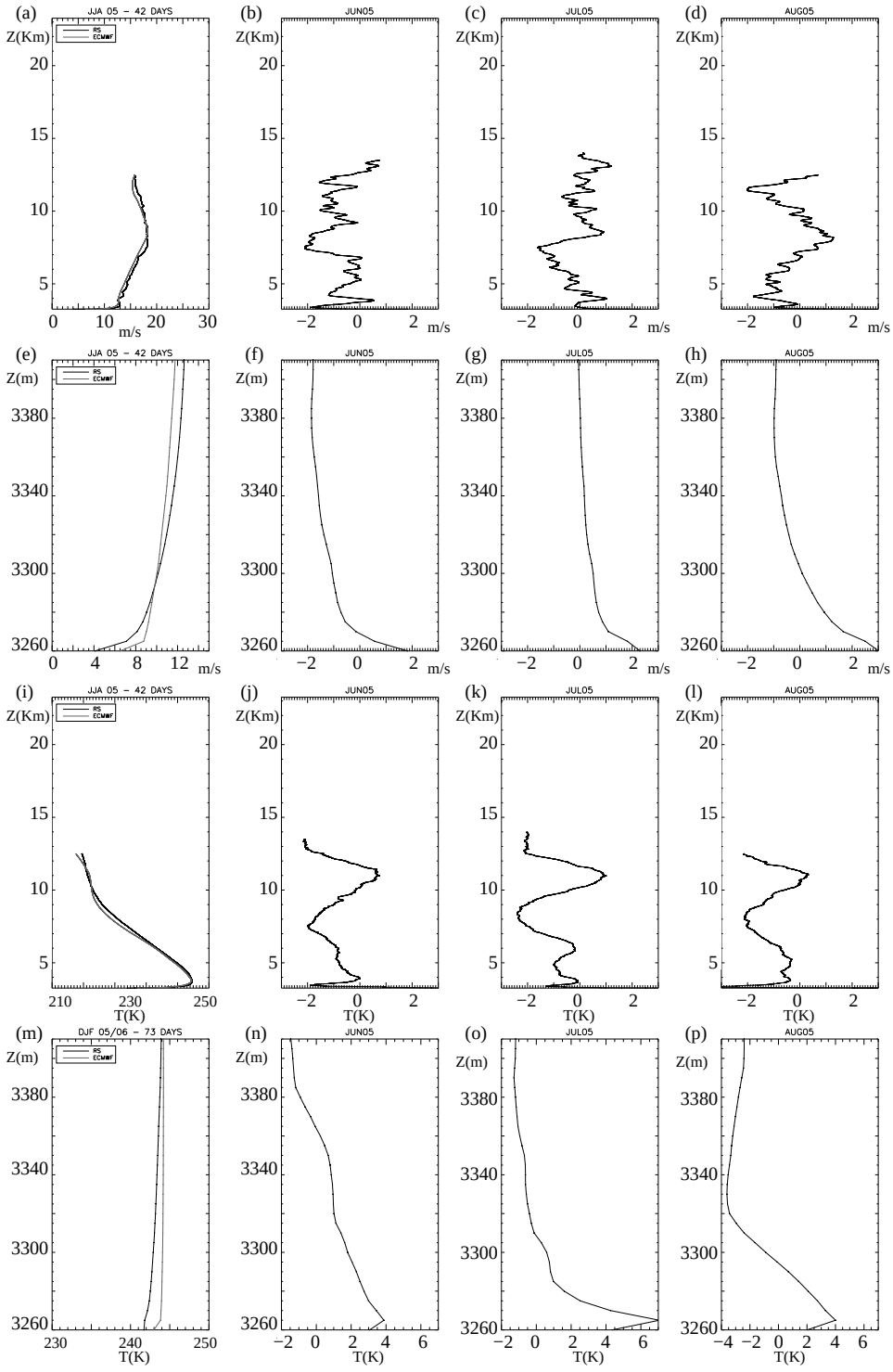

FIG. 2. Same as figure 1, but for winter 2005 (months of June, July and August).

winter, against 21 km in summer). Over the entire free troposphere the summer vertical profiles extracted from the ECMWF analyses are very close to the radiosoundings, as well for wind speed (Fig. 1a) as for temperature (Fig. 1i). The maximum wind speed difference reaches a peak smaller than 3 m/s in December at around 8 km, the level of the jet (Fig. 1b). The rest of the time this difference is rarely more than 1 m/s in absolute. In temperature, in summer, the differences on the mean values are smaller than 2°C up to 17 km where the differences in February are the most important (Fig. 1l). Even in winter the agreement is very good in the free troposphere (up to 12 km). The mean of the wind speed difference is less than 2 m/s, in June (Fig. 2b), in July (Fig. 2c) and in August (Fig. 2d). The temperature differs from less than 2°C. The results support the analyses done by Geissler and Masciadri 2006.

The first meters above the ground critical for astronomers are now investigated. It is well known that the boundary layer in Dome C is thinner than any mid-latitude site and even South Pole (Aristidi et al. 2005a; Lawrence et al. 2004). Thus it is crucial to have a good prediction of the evolution of the first hundred of meters of the atmosphere above the ground. To achieve it with atmospherical model, initial conditions are important. Looking at the first 150 m of the vertical profiles, it appears that the mean temperature from the ECMWF analyses is two warm: up to +4°C in summer, in February (Fig. 1p) and up to + 7°C in winter, in July (Fig. 2o), in the very first levels. The differences in wind speed are less important: around 1 m/s in summer (Fig. 1efgh) at the same level, and the difference can reach 3 m/s in winter at the surface (in August, Fig. 1h). In conclusion, the ECMWF analyses above Dome C appear to be reliable enough to allow for their use as initial and boundaries conditions of our mesoscale model. However, the differences near the ground, especially in temperature, could lead to a bad prediction of the evolution of the state of the lower atmosphere, essential to the evaluation of optical turbulence with the Meso-NH mesoscale model. We are therefore working on an optimization of the numerical code describing the physics of the ground surface to be able to run Meso-Nh on Antarctica.

In the next section we discuss the best way to configure the model in order to have the best prediction possible of the weather in the Dome C area.

3. Choice of the best configuration for the numerical model

Different configurations of Meso-Nh have been tested. Here we do not predict the optical turbulence yet. We focus on the first step of this work: having a configuration of the mesoscale model the most effective possible, in terms of prediction of standard meteorological parameters and computing time.

We examine the influence of the horizontal resolution, vertical resolution, of the two-way grid nesting interactive technique, and the choice of the surface scheme. The day chosen for our numerical simulations is the 22 July 2005 (a winter day). The simulations are initialized with the ECMWF analysis of 22 July at 1200 UTC and last for 12 hours. The vertical profiles of wind speed and temperature extracted from the ECMWF analysis are visible on figure 3.

a. Influence of the horizontal resolution

Swain and Gallée (2006) already performed simulations above Antarctica at low horizontal resolution (100 km mesh-size) using the MAR model validated above Antarctica (Gallée and Pettré 1998, Naithani et al. 2002). In order to identify which horizontal resolution is required to reproduce the meteorological parameters values above Dome C with the level of precision required we performed two simulations. One has a horizontal mesh-size of 100 km, and entirely covers

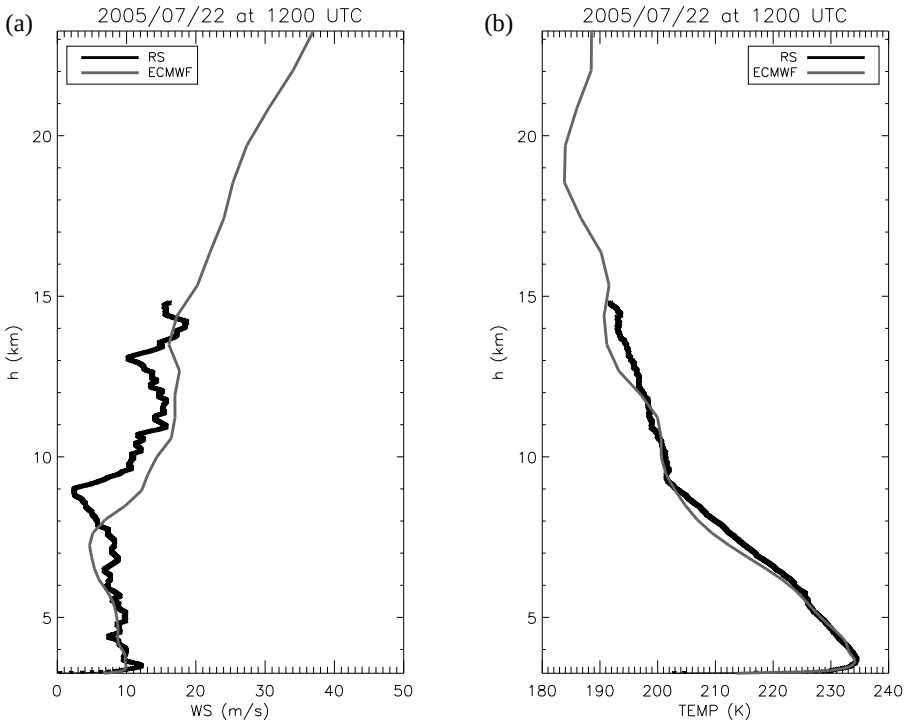

FIG. 3. Vertical profiles above Dome C on 22 July 2005 of (a) wind speed and (b) temperature. In grey: ECMWF analysis; in black: radiosounding.

Antarctica. The other one has a horizontal mesh-size of 1 km and is centered above Dome C. The topography of the domains is displayed figure 4.

To compare the results of the simulations we look at the vertical profiles of wind speed and

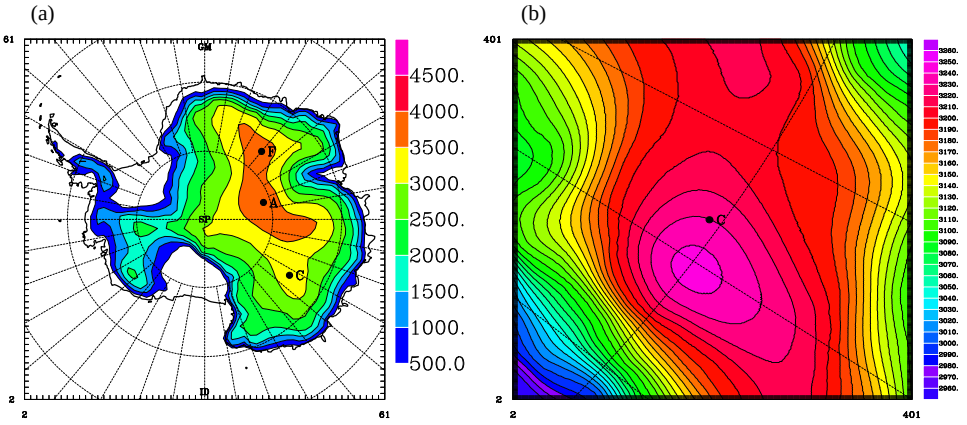

FIG. 4. Topography of Antarctica as seen by the Meso-NH model (a) with 60x60 points and a mesh-size of 100 km (isocontours every 500 m, starting at 500 m) and (b) with 400x400 points with a mesh-size of 1 km (isocontours every 10 m, starting at 2960 m) centered above the Concordia station at Dome C. Letters represent the location of different sites of interest: A for Dome A, F for Dome F and C for Dome C.

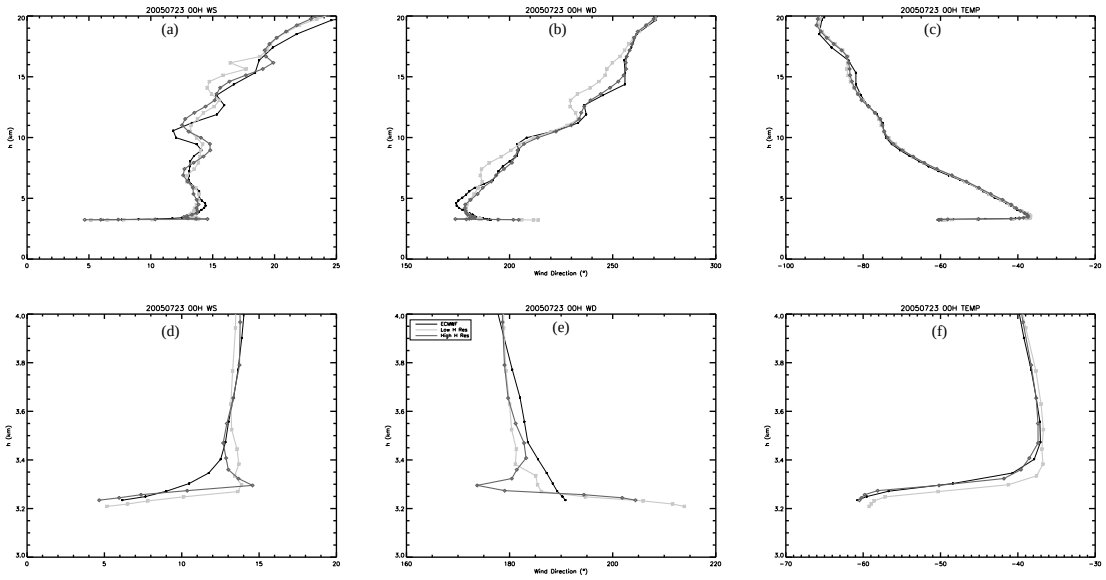

FIG. 5. Comparison of Dome C vertical profiles of ECMWF analysis and Meso-NH high and low horizontal resolution numerical simulations of (a) wind speed, (b) wind direction and (c) temperature, in the free troposphere and (d) wind speed, (e) wind direction and (f) temperature, in the first kilometer near the ground.

temperature above Dome C at the end of the simulation, i.e at 0000 UTC the 23 July 2005. As no radiosounding is available at this hour, we compare the results with profiles from the ECMWF analysis. This is shown on figure 5. It is important to highlight that the model with high-resolution shows the first grid point at a height more similar to the real height of the Dome C. Thus we have a better prediction of wind speed and temperature, especially in the lowest levels (figures 5d and 5f, respectively). Except in a layer close to the surface (figure 5e) the wind direction in the troposphere seems to be better predicted (figure 5b).

As expected, the use of high resolution improves the prediction of standard meteorological parameters above Dome C.

b. Influence of the vertical resolution

Here we look at the influence of the vertical resolution on the numerical simulations. The two simulations which results are shown figure 6 differ only by the vertical grid. One has 50 levels on the vertical, starting at 10 m above the ground and with 6 points in the first hundred of meters, a stretching up to 3500 m and then a constant Δ(h)=600 m up to 20 km. The second one has a higher vertical resolution: 60 levels on the vertical, with the first level at 2 m and 15 points in the first hundred of meters, a stretching up to 3500 m and then a constant Δ(h)=600 m up to 20 km.

This time the differences remain small, and are only located near the surface. The temperature in the first levels is colder in the simulation at high resolution (figure 6f). This could be considered as an optimization of the configuration for our model. Indeed we have seen in the second section that the ECMWF analyses are generally too warm near the surface.

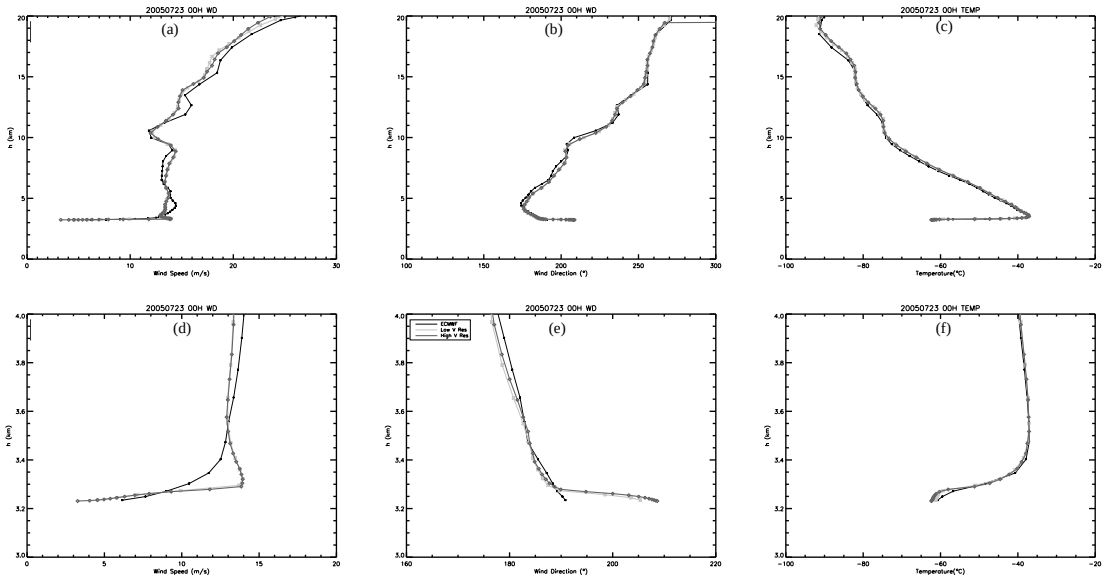

FIG. 6. Comparison of Dome C vertical profiles of ECMWF analysis and Meso-NH high and low vertical resolution numerical simulations of (a) wind speed, (b) wind direction and (c) temperature, in the free troposphere and (d) wind speed, (e) wind direction and (f) temperature, in the first kilometer near the ground.

c. Use of the grid-nesting technique

Now we test the use of the two-way interactive grid-nesting technique in Meso-NH. The simulation taken as a reference has a horizontal resolution of 2.5 km, without grid-nesting. The domain of computation is centered on Dome C and has 120x120 points. The grid-nested simulation make use of two imbricated domains. The first one has a horizontal resolution of 10 km, is centered on DomeC and has 100x100 points. The innermost domain is the same domain as in the simulation taken as a reference. The results are displayed figure 7. The major improvement obtained with the grid-nesting configuration comes from the first kilometer above the ground, with a better prediction of the wind speed (figure 7d) and wind direction (figure 7e).

d. Influence of the surface snow scheme

Some observations of surface temperature at Dome C are available (S. Argentini, personal communication). When output from mesoscale simulations with Meso-NH are compared with these observations (not shown here), it appears that the temperature at the surface is too warm. Prediction of a good surface temperature is crucial to allow for a further good prediction of optical turbulence. That's why the choice of a good surface snow scheme in Meso-NH is of prior interest in Antarctica, because of its very particular surface made only of ice and snow.

The results between a reference simulation using the standard ISBA scheme and a simulation using the ISBA-ES (Explicit Snow, Boone and Etchevers 2001) are compared. In the standard scheme the surface is described as a mixed snow-soil medium for computation of surface temperature and fluxes. In the multilayer ISBA-ES scheme, snow and soil are separated. Three more snow prognostic variables, depth dependent, are added: Snow Heat Content, Snow Liquid Water Equivalent and Snow Density. The results of the two simulations are visible figure 8. The only

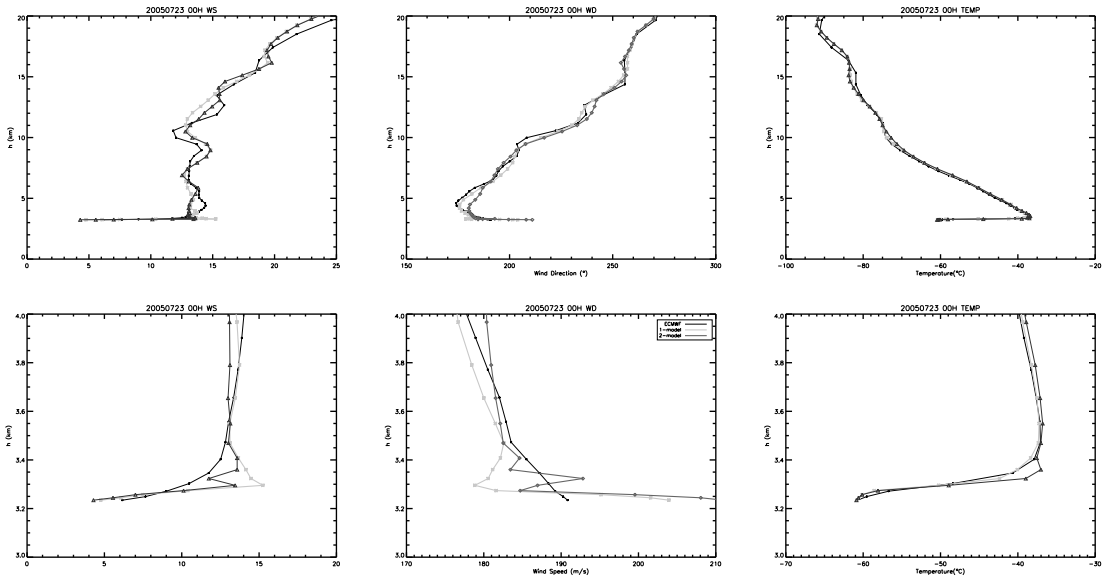

FIG. 7. Comparison of Dome C vertical profiles of ECMWF analysis and Meso-NH numerical simulations with (in dark grey) or without (in light grey) grid-nesting of (a) wind speed, (b) wind direction and (c) temperature, in the free troposphere and (d) wind speed, (e) wind direction and (f) temperature, in the first kilometer near the ground.

visible difference is in the very first levels of the atmosphere, with a cooling of about 3°C (figure 8f). The same remark than in the previous section about the use of vertical resolution can be done: this cooling can be considered as an improvement of the prediction.

4. Conclusion

We have performed different mesoscale numerical simulations with the non-hydrostatic model Meso-Nh above Antarctica. The goal was to define the best configuration possible for the model allowing a good short-term prediction of the evolution of the state of the atmosphere. We looked at different standard meteorological parameters (wind speed, wind direction, temperature) useful for the following step of this work which is forecasting of optical turbulence above a potential astronomical site. We chose one winter day to perform the simulation (22 July 205 from 12 UTC to 00 UTC). The conclusion is that the grid-nesting technique, with high horizontal resolution (of about 1 km), is essential to have a good prediction of wind and temperature. More over, a refinement in the initial conditions of the surface seems inevitable. Indeed the ECMWF analyses used for this study appear to be too warm in the first level, which could lead to a bad forecasting. The use of the ISBA-ES scheme tends to correct part of this discrepancy. Nevertheless to conclude about the intensity of this discrepancy in surface temperature, and of the possible positive impact of the ISBA-ES scheme, other simulations need to be performed under different thermodynamic conditions. Observations available at the end of the 12 hours integration are also important to finally validate our conclusions.

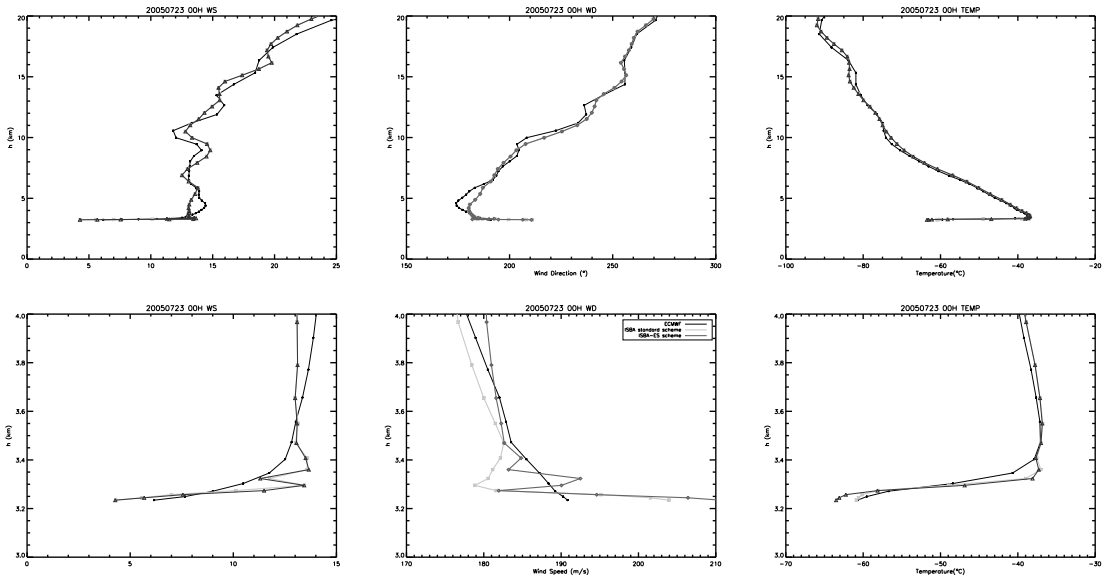

FIG. 8. Comparison of Dome C vertical profiles of ECMWF analysis and Meso-NH numerical simulations with ISBA standard surface scheme (in dark grey) or with ISBA-ES surface scheme (in light grey) of (a) wind speed, (b) wind direction and (c) temperature, in the free troposphere and (d) wind speed, (e) wind direction and (f) temperature, in the first kilometer near the ground.

Acknowledgments.

This work has been funded by the Marie Curie Excellence Grant (ForOT) - MEXT - CT - 2005 - 023878

References

Arakawa, A. and F. Mesinger, 1976: Numerical methods used in atmospheric model. *GARP Tech. Rep.*, **17**.

Aristidi, E. et al., 2005a: An analysis of temperatures and wind speeds above Dome C, Antarctica. *Astron. Astroph.*, **430**. 739-752.

Asselin, R., 1972: Frequency filter for time integrations. *Mon. Wea. Rev.*, **100**, 487-490.

Boone, A. and P. Etchevers, 2001: An intercomparison of three snow schemes of varying complexity coupled to the same land surface model: local-scale evaluation at an alpine site. *J. of Hydrometeo.*, **2**, 374-394.

Bougeault, P. and P. Lacarrère, 1989: Parameterization of orographic induced turbulence in a mesobeta scale model. *Mon. Wea. Rev.*, **117**, 1872-1890.

Cuxart, J., Bougeault, Ph. and Redelsperger, J.L., 2000: A turbulence scheme allowing for mesoscale and large-eddy simulations. *Q. J. R. Meteorol. Soc.*, **126**, 1,30.

Gal-Chen, T. and C.J. Sommerville, 1975: On the use of a coordinate transformation for the solution of the Navier-Stokes equations. *J. Comp. Phys.*, **17**, 209-228.

Gallée, H. and P. Pettré, 1998: Dynamical constraints on katabiatic wind cessation in Adélie Land, Antarctica. *J. Atmos. Sci.*, **55**, 1755-1770.

Geissler, K. and E. Masciadri, 2006: Meteorological parameter analysis above Dome C using data from the European Centre for Medium-Range Weather Forecasts. *PASP*, **118**, 1048-1065.

Lawrence, J. S., M. C. B. Ashley, A. Tokovinin and T. Travouillon, 2004: Exceptional astronomical seeing conditions above Dome C in Antarctica. *Nature*, **431**, 278-281.

Lipps, F. and R.S. Hemler, 1982: A scale analysis of deep moist convection and some related numerical calculations. *J. Atmos. Sci.*, **39**, 2192-2210.

Masson V. 2000: A physically based scheme for the urban energy budget in atmospheric models. *Bound. Layer Meteor.*, **94**, 357-397.

Naithani, J. H. Gallée and G. Schayes, 2002: Marine air intrusions into Adélie Land sector of East Antarctica. *J. Geophys. Res.*, **107**, no D11, p. ACL 6 1-16

Noilhan, J and S. Planton, 1989: A simple parameterization of land surface processes for meteorological models. *Mon. Wea. Rev.*, **117**, 536-549.

Swain, M. and H. Gallée, 2006: Antarctic boundary layer seeing. *PASP*, **118**, 1190-1197.

Space-based GPS for Monitoring Weather and Climate

Steven Businger*
University of Hawaii

and

Bill Kuo
UCAR COSMIC Project Office

ABSTRACT

The Constellation Observing System for Meteorology, Ionosphere & Climate (COSMIC) consists of six micro-satellites that use the radio occultation (limb sounding) technique to gather vertical profiles of atmospheric refraction index (Fig. 1). The refraction index profiles can then be processed to provide vertical profiles of temperature in the stratosphere, temperature and water vapor in the troposphere, and electron density in the ionosphere. The six COSMIC satellite orbits result in approximately 2000 profiles daily over the entire Earth and in all weather conditions (Fig. 2). The resulting data not only have great value for weather, climate, and space weather research and forecasting, but also for geodesy, gravity research, and other applications. Assimilation schemes are being developed to effectively integrate the COSMIC data stream into existing operational weather forecasting models. Early results from the European Center for Medium Range Forecasting show improvements in global weather model forecasts, with the greatest gains in the Southern Hemisphere and over the northern Pacific Ocean where the radiosonde network is least dense.

**Corresponding author address:* Steven Businger, University of Hawaii.
E-mail: businger@hawaii.edu

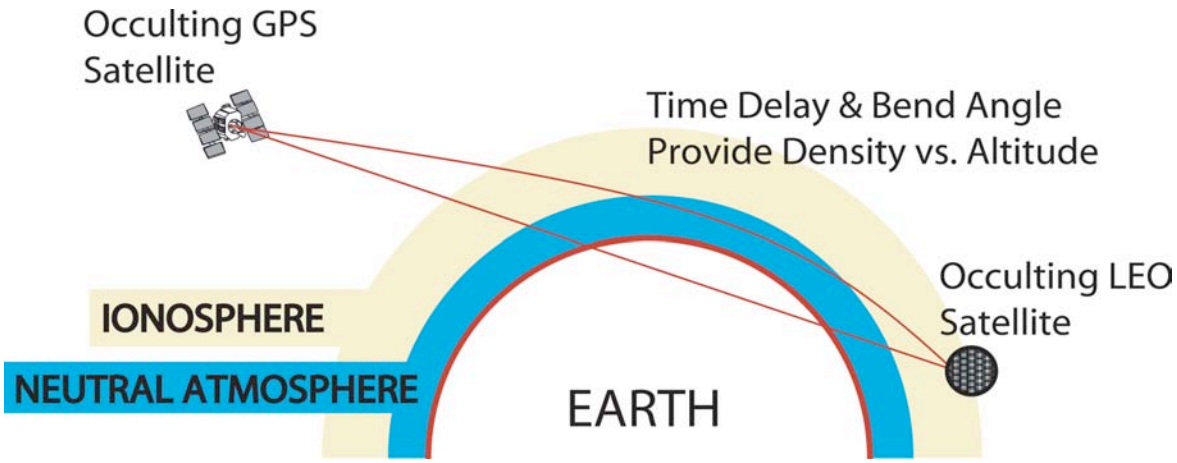

Fig. 1 Schematic diagram depicting a COSMIC low Earth orbiting satellite intercepting a signal from a GPS atellite at the time of occultation.

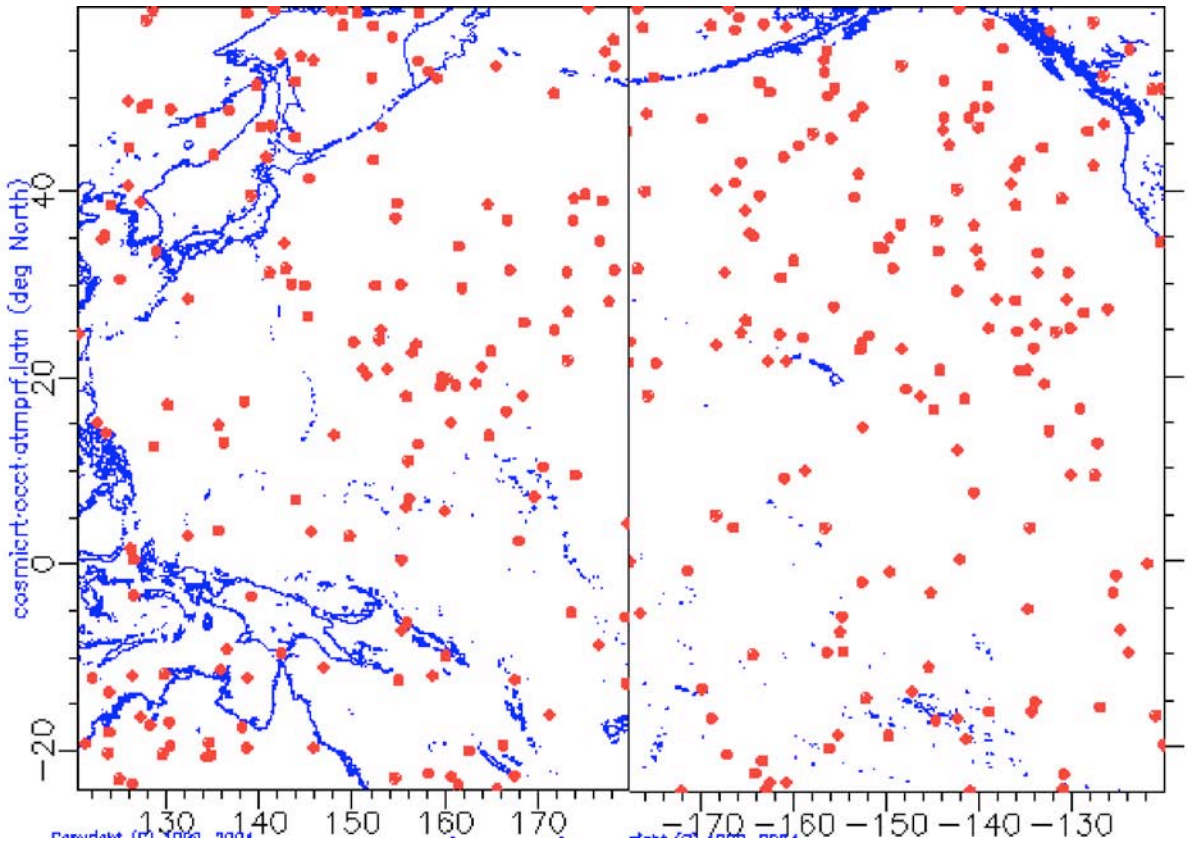

Fig. 2 COSMIC profile locations for 7 January 2007.

Modeling Optical Turbulence and Seeing over Mauna Kea: Algorithm Refinement

Tiziana Cherubini*, Steven Businger and Ryan Lyman
University of Hawaii

ABSTRACT

An optical turbulence algorithm has been running operationally since April 2005 at the Mauna Kea Weather Center. The algorithm makes use of the information on turbulence kinetic energy provided by a planetary boundary layer scheme available in the Penn State/NCAR mesoscale model (MM5). It provides an estimate of the turbulent fluctuations of the atmospheric refractive index, C_n^2, and therefore seeing for the summit area. The potential and limitations of the implemented optical turbulence algorithm are investigated and illustrated in this paper. One year of observed seeing data from four observatories are compared to the model forecast seeing and a statistical analysis is performed. Given the fact that a poor seeing prediction might be a consequence of a poor model forecast rather than a deficiency in the seeing algorithm performance, a sensitivity test regarding the accuracy of the underlying numerical weather forecasts is carried out. A sensitivity analysis of the model's eddy diffusivity scheme is also performed. It is anticipated that the optical turbulence algorithm is sensitive to the parameterization of the eddy diffusivity. Results from a simple calibration of the optical turbulence algorithm will be presented.

**Corresponding author address:* Tiziana Cherubini, University of Hawaii.
E-mail: tiziana@hawaii.edu

Modeling and Forecasting Optical Turbulence with DEEST

Sara C. Adair*
Atmospheric and Environmental Research, Inc., Lexington, MA 02421

George Y. Jumper
Air Force Research Laboratory, Hanscom AFB, MA, 01731-3010

Jean Vernin
L.U.A.N., UMR 6525, Nice, France

Gerard T. Fairley
Atmospheric and Environmental Research, Inc., Lexington, MA 02421

ABSTRACT

Seeing can be modeled and forecast with DEEST, the Directed Energy Environmental Simulation Tool. DEEST quantifies optical turbulence impacts along user-defined paths (e.g. from a telescope to the top of the atmosphere) for the refractive index structure constant, C_n^2, and C_n^2 derived values. The DEEST GUI can present results in a number of ways, for instance it can create horizontal cross-sections for vertically integrated values derived from C_n^2 (e.g. spherical Rytov, coherence length, isoplanatic angle and scintillation) and vertical cross sections and horizontal polar plots for spherical Rytov values. The surface layer, boundary layer and free atmosphere are represented with one or more C_n^2 models. DEEST combines these models into a consistent model atmosphere and is currently driven by widely available numerical weather prediction data. Flexibility was paramount in DEEST programming so DEEST can easily install other C_n^2 models (if need be) or to adapt to input from alternate mesoscale models. DEEST has processed weather model data to determine an opaque cloud representation. DEEST validation includes Generalized SCIDAR (GS) and balloon thermosonde data. GS, LIDAR and other types of data can be used to adjust DEEST models.

*Corresponding author address: Sara Adair, AER, Inc., 131 Hartwell Ave, Lexington, MA, 02421
E-mail: sadair@aer.com

Influence of Coastal Meteorological Processes on Aerosol Transport

Sethu Raman*
North Carolina State University

ABSTRACT

Observations from studies in two regions where aerosol transport is dominated by the coastal land-air-sea interaction will be presented. An observational and modeling study was performed over the Arabian Gulf region to investigate the coastal circulations and aerosol transport in the area. Climatological data and observations from the United Arab Emirates – Unified Aerosol Experiment (UAE2) were used to develop a better understanding of the complex meteorological processes in the Arabian Gulf region. The geography of this region is unique because it can cause land-sea-air-land interactions that will modify the overlying air masses. Measurements of aerosol concentration taken during the UAE2 experiment are used to investigate aerosols, namely dust, transported in the Arabian Gulf region. Vertical profiles of dust concentration along with vertical profiles of potential temperature and wind are used to determine the source region, transport distance, and height of the dust layer. The aircraft aerosol vertical profiles suggest highest dust concentrations occur near the surface.

Observations of aerosol distribution over another region, the Indian ocean, obtained during INDOEX(1999) will be presented in relation to their long range transport and the coastal meteorological processes. Highest concentrations occur immediately above the marine boundary layer.

*Corresponding author address: Sethu Raman, North Carolina State University
E-mail: sethu_raman@ncsu.edu

A Ten Year Cloud Climatology of the Hawaiian Islands as Derived by GOES

Randall Alliss*
Northrop Grumman IT - TASC

ABSTRACT

Cloud retrieval algorithms have been developed and applied to the current generation of National Oceanic and Atmospheric Administration (NOAA) Geostationary Environmental Operational Satellite (GOES) imagery to produce a twelve year climatology of cloudiness over the Continental United States (CONUS) and ten years over the state of Hawaii. The database contains cloud no cloud decisions at approximately fifteen minute and four kilometer resolution, respectively. Over 350,000 images have been processed over this twelve year period.

The GOES imager includes multi-spectral channels including one visible and four infrared. Cloud detection is accomplished by modeling the radiance of the ground in the absence of clouds and comparing with the actual radiance values from the imagery. A composite cloud decision is formed by objectively combining the results of the tests from the individual channels. The strength of using all bands as opposed to using a single band was demonstrated very early in the development. For example, low clouds radiating at a similar temperature to the earth are detectable at night with the use of the shortwave infrared channel. A combination of the visible and shortwave infrared channels helps to distinguish low and high clouds from snow cover.

To date, this database has been used to study the impacts of clouds on optical communications for the NASA – Jet Propulsion Laboratory. Since clouds adversely affect the transmission of an optical communications link, a reliable communication system is only possible through the use of multiple geographically diverse ground stations. The relatively high spatial and temporal resolution of this GOES database makes it possible to study the cloud correlations between different locations.

Results produced by this database indicate a measurable variability in cloudiness over many reporting stations across CONUS as well as Hawaii during the 1995 – 2006 time period. Mean cloudiness varies from less than 30% in the dessert regions and the

mountain peaks of Maui and the Big Island to greater than 70% in the Great Lakes region and Pacific Northwest. Results have been compared with cloudiness derived from a ground based Whole Sky Imager (WSI) for select locations and have produced very good agreement. This paper will present climatology of cloudiness over the Hawaiian Islands including the summits of Mauna Kea and Haleakala.

*Corresponding author address: Randall Alliss, Northrop Grumman IT – TASC.
E-mail: Randall.Alliss@ngc.com

Wind and turbulence models for Haleakala with wind models for diverse astronomical sites

Lewis C. Roberts, Jr.* and L. William Bradford
the Boeing Company, Kihei, Hawaii

1. Introduction

The movement of turbulent regions past an observer induces temporal variations in seeing. If wind speeds are sufficiently high that turbulence does not evolve significantly over a measurement period, we apply Taylor's hypothesis and treat the temperature fluctuations as quantities that are advected by the wind. Variations in wind velocities lead to speckle "boiling" and to constraints on the bandwidth of adaptive optical systems.

A generalized version of such a wind model is:

$$v(z) = v_G + v_T \exp\left(-\left[\frac{z\cos\zeta - H_T}{L_T}\right]^2\right)\left(\sin^2\phi + \cos^2\phi\cos^2\zeta\right)^2 \quad (1)$$

where v is the wind speed, z is the altitude, v_G is the wind speed at the ground or low altitude, v_T is the wind speed at tropopause, h_T is the altitude of the tropopause, L_T is the thickness of the tropopause layer, ζ is the zenith angle of the observation, and ϕ is the angle of the wind direction relative to the telescope azimuth. The wind direction term is often dropped.

Bufton (1973) is often cited as the source for this model, but that paper does not present an explicit wind model. The basic form of the model actually appeared in Greenwood (1977).

$$v(z) = 8 + 30\exp\left(-\left[\frac{(z\sin\theta - 9400)}{4800}\right]^2\right), \quad (2)$$

where z is the height in m, $v(z)$ is the wind speed in m/s, and θ is the angle from the Zenith. However, the unwary reader might miss the statement in the body of the original paper that the height $z = 0$ corresponds to a mean sea level (MSL) altitude of 3048 m. This is the height of the Maui Space Surveillance System on Haleakala, where the analysis was being used. So the height of the tropopause term, 9400 m, should really be 12448 m when the model is used for sites other than Haleakala. The model from Greenwood (1977) was derived by averaging radiosonde data collected from balloons launched from Lihue on the island of Kauai from 1950-1970 and from Hilo on the island of Hawaii from 1950-1974.

2. Data Analysis

We downloaded atmospheric sounding data for 1973 January till 2006 September for a number of stations close to an astronomical observatory. It seems to be a judgment call on how far away

*Corresponding author address: the Boeing Company, 535 Lipoa Pkwy, Suite 200, Kihei HI 96753. lewis.c.roberts@boeing.com

an observatory can be from a radiosonde launch station and still experience the same wind profile. Separation in latitude is generally more important than separation in longitude, reflecting the zonal nature of wind flows on Earth. Thus San Diego's wind profile differs significantly from Oakland's wind profile, but has a similar profile to Midland, Texas, even though Oakland is closer to San Diego than is Midland.

For each sounding, the wind speed is recorded as a function of height. The heights are irregularly measured, so the data were interpolated onto a fixed height grid with an increment of 400 m and then averaged for various time periods. We created the average wind speed and direction for each of the 12 months for each of the selected sites up to 30 km. The Gaussian wind model of Greenwood (1977) (Equation 2) only fit the tropospheric winds and ignored the stratospheric winds. It is possible to fit both of those winds if a Gaussian is summed with a quadratic expression,

$$v(z) = A_0 \exp - \left(\frac{z - A_1}{A_2} \right)^2 + A_3 + A_4 z + A_5 z^2. \quad (3)$$

The peak tropospheric wind speed has a well defined annual cycle. There is also a variation in the Gaussian width and height of the peak wind speed. The quadratic fits the upper level winds, but the terms do not have as much physical meaning as the the Gaussian terms in Equation 1. Most likely the stratospheric winds can be modeled with a Gaussian also, but we do not have data at high alitude to make the fit. If the stratospheric winds are not important to the details at hand, then coefficients A_4 and A_5 can be dropped.

We computed the standard deviation of the wind speeds and have determined that the Hilo and Lihue wind profiles are the same to within a standard deviation. Since the major astronomical observatories in Hawaii are closer to Hilo than Lihue, we have used Hilo as the basis for our Hawaii model. We also determined that the average wind profiles for San Diego, Tucson, Flagstaff, Albuquerque and Midland are all the same within a standard deviation. The sites are geographically separated by hundreds of kilometers, but they are all on a very similar latitude.

3. A Haleakala Turbulence Profile

Seeing at the top of Haleakala has been reported somewhat intermittently, for more than 40 years. Attempts to model the profile of the atmospheric turbulence strength have been made a few times. Beland (1993) discusses a particular model, the Maui Night Model, which arose from a series of thermosonde measurements in the 1980s.

For some years, the Maui Night Model was the profile of choice for Haleakala. However, the values for r_0 and for isoplanatic angle θ_0 did not agree with a series of optical measurements made from about 1986–1990 at the Maui Space Surveillance System. Since the balloon launches tended to cover on relatively small intervals of time, it was decided in 2003 that a new model based on the optical measurements would be undertaken. Since the balloon data that went into the Maui Night Model was the only profile data available, it was decided to modify the Maui Night Model until it yielded the median values of r_0 (12.9 cm) and isoplanatic angle θ_0 (9.6 μrad) from the optical measurements. The subsequent model is known as the Maui3 model.

References

Beland, R., 1993: Propagation through atmospheric optical turbulence. *The Infrared & Electro-Optical Systems Handbook*, Smith, F., Ed., SPIE Press, 157–232.

Bufton, J., 1973: Comparison of vertical profile turbulence structure with stellar observations. *Appl. Opt.*, **12**, 1785–1793.

Greenwood, D., 1977: Bandwidth specification for adaptive optics systems. *J. Opt. Soc. of Am.*, **67**, 390–393.

Testing turbulence model at metric scales with mid-infrared VISIR images at the VLT

Andrei Tokovinin*
Cerro Tololo Inter-American Observatory, La Serena, Chile

Marc Sarazin
European Southern Observatory, Garching bei München, Germany

Alain Smette
European Southern Observatory, Santiago, Chile

ABSTRACT

The wave-front coherence length r_0 reaches metric values at mid-infrared wavelengths, hence long-exposure images can probe the large-scale spatial structure of turbulence directly in a model-independent way. We obtained simultaneous mid-IR and optical images of a point source at the VLT using the VISIR instrument and the Shack-Hartmann sensor. The analysis shows that the departure of the phase structure function from a pure Kolmogorov model is very strong and can be adequately represented by the von Karman model with decametric outer scale. Various instrumental effects influencing the results are discussed.

This work has been accepted for publication in MNRAS (2007). See also astro-ph: 2007arXiv0704.0470T

*Corresponding author address: Andrei Tokovinin, Cerro Tololo Inter-American Observatory, Casilla 603, La Serena, Chile
E-mail: atokovinin@ctio.noao.edu

SESSION 4

APPLICATIONS OF OPTICAL TURBULENCE OBSERVATIONS AND CUSTOM FORECASTING IN TELESCOPE ASTRONOMY.

The "Missing Link" Between Meteorology and Astronomy

Douglas Simons* *(invited speaker)*
Gemini Observatory, Hawaii

and

Jean-Rene Roy
Gemini Observatory, Hawaii

ABSTRACT

Unlike most other scientists, astronomers are uniquely dependent on the whims of nature to succeed. For centuries astronomers have studied the heavens with only elementary weather forecasting skills, perhaps in the form of reading the shape of approaching clouds or the hand of a barometer. In recent decades, through the use of satellite imaging and computer generated forecasts, astronomers have been able to gain some advance warning of inclement weather which may dictate their ability to conduct nighttime observations. Nonetheless, even toward the end of the 20th century, this level of forecasting was rudimentary compared to what is possible today. We explain the unique interconnection between meteorology and astronomy, including the strategic importance of weather forecasting in the operations of modern observatories, touch on the history of the Mauna Kea Weather Center and its unique niche in astronomy, the interdisciplinary synergies it relies upon, and the challenge of providing this service in the global astronomy arena.

**Corresponding author address:* Douglas Simons, Gemini Observatory, Hawaii.
E-mail: dsimons@gemini.edu

Thermal Seeing Modeling as a Design and Performance Analysis Tool

Konstantinos Vogiatzis*, George Z. Angeli
Thirty Meter Telescope Observatory Corporation, Pasadena, California

Jacques Sebag and Srinivasan Chandrasekharan
National Optical Astronomy Observatory, Tucson, Arizona

ABSTRACT

Mirror, dome and enclosure local seeing are aspects of medium (air) induced seeing that greatly influence the optical performance of large ground-based telescopes. Site characterization measurement cannot predict the contribution of summit development and mirror/enclosure induced thermal seeing to Ground Layer (GL) seeing. This paper describes a strategy for modeling the effects of passive ventilation, enclosure-facilities configuration and topography on the optical performance of large telescopes such as the Thirty Meter Telescope (TMT) and the Large Synoptic Survey Telescope (LSST). Computational Fluid Dynamic (CFD) analyses are combined with thermal analyses to model the effects of turbulence and thermal variations within the airflow around and inside the telescope-enclosure configuration.

*Corresponding author address: Konstantinos Vogiatzis, TMT Observatory Corp., 2632 E. Washington Blvd., Pasadena, CA, 91107
E-mail: voyages@tmt.org

1. Modeling methodology

Previous implementation of the thermal models has been published by Vogiatzis and Angeli (2006).

a. Dome Seeing

CFD simulations are performed for a given venting configuration. The thermal boundary conditions are chosen to a) demonstrate the net effect of the enclosure to dome seeing and b) simulate a worst case expected ratio of dome to mirror seeing. It is noted that in this study "mirror seeing" refers to the seeing caused by temperature gradients and turbulence inside the primary mirror surface boundary layer, while "dome seeing" refers to seeing observed through the rest of the optical path up to 10m-25m above the opening. Therefore the primary mirror is given an adiabatic surface. The enclosure and building walls are expected to radiate and be cooler than ambient air temperature and are given a heat flux value, based on competing convection from the selected wind speed and radiation to an effective sky temperature 20K below surface temperature. More on the CFD methodology and validation can be found in MacMynowski et al (2006).

The seeing post-processing model relates mechanical and thermal turbulence output to refractive index structure function coefficient values. The theory behind the model is described by Wyngaard et al (1971). To that end velocity and temperature profiles, along with mechanical and thermal turbulent energy dissipation rate and eddy viscosity profiles are required and provided by the CFD calculations. Thus three-dimensional quasi-static C_N^2 fields are generated. Diameter values of the seeing disk encircling 80% of the energy (EE80) along a given optical path are estimated by integrating the corresponding profiles.

b. Mirror Seeing

A full year record of wind speed and ambient temperature at a current sampling rate of 2 min is used. A similar record of telescope elevation-azimuth positions is also available. Finally a map of venting efficiencies for various enclosure telescope orientations is generated from CFD results relating external wind speeds to U_{M1}, velocity above the primary mirror. The records are used to calculate the correct M1 velocity and thus heat transfer rate on the mirror surface at any given time during the night. The air temperature above M1 is assumed the same as ambient during the night. Night time is defined from sunset to sunrise. M1 temperature is calculated throughout the night. After sunrise a target temperature for the next sunset is estimated and a possible range of initial mirror temperatures for the next sunset are scanned in order to select the optimum for minimum expected average seeing for the upcoming night. If the exact temporal behavior of the coming night is not known in advance results can be produced assuming M1 is treated during the day so that its temperature at sunset is that of midnight of the previous night. Alternatively, a fixed initial ΔT for the entire year can be used.

To calculate the M1 temperature an analytical transient thermal model based on Newton's cooling law and incorporating a conduction heat flux and a radiation term is used. Empirical models then relate the observed temperature difference between the mirror surface and the ambient air to EE80. The model used for forced convection was introduced by Zago (1996), while for natural convection a model derived from the observed behavior of CFHT described by Racine et al (1991) is used.

2. Results

a. LSST – Dome Seeing

Several simulations for 9 different telescope orientations were performed; three zenith and three wind-telescope relative azimuth angles. In all cases the wind direction was kept fixed at 20° N-NE and the wind speed was chosen to have its expected median value. The integration of the resulting C_N^2 field was performed along the optical path starting 40m from the telescope elevation axis (outwards) all the way to the camera to estimate the overall contribution from the inside and outside of the enclosure. Intermediate results can also be obtained for any given segment of the optical path to investigate the individual contributions. The dome seeing results in mas are summarized in Table 1.

TABLE 1 LSST dome seeing results for the first 25m outside the enclosure (left) and inside the enclosure (right) in mas.

Zenith\Rel. azimuth	±90°	0°	180°
20°	73/49	70/117	105/125
40°	103/27	115/102	91/119
75°	57/73	46/53	53/126
Weighted average	92/36	98/104	93/121

The weighted average results take into account the expected telescope orientation probability distribution and the site wind rose. The overall weighted average is estimated at 93/61 mas. It is clear from the last row that when mirror flushing is adequate because of unobstructed flow-through (±90° rel. az.) the contribution of dome seeing is small relative to local seeing. In contrast, the seeing caused by the enclosure-exterior-generated turbulence seems to be uniform in azimuth, even though at high zenith angles (75°) the use of the roof windscreen makes the enclosure more aerodynamically efficient. At 180° azimuth no flow-through occurs through the optical path so seeing is worst.

b. TMT – Thermal Seeing

In case of TMT the probabilistic approach is taken to the next level. As mentioned earlier in the introduction, the CFD results are used by the thermal models. In particular, the mirror seeing model requires a matrix of M1 mean velocities (normalized by external wind) while the dome seeing model requires the complete 3D field of temperature and turbulence inside the enclosure up to ~10m beyond the aperture. For mirror seeing a zenith-azimuth dependent map of normalized wind speed (venting efficiency) is generated and is presented in Fig. 1. The dome seeing model yields the performance map shown in Fig. 2.

The framework that combines mirror and dome seeing spans the entire year solving for the M1 temperature interpolating for a venting efficiency based on the corresponding telescope orientation and for a corresponding dome seeing value. Mirror and dome seeing EE80 values are added in quadrature per time interval. Thus a time record of performance is generated. In Fig. 3 the cumulative distribution functions of mirror, dome and combined thermal seeing are shown. The sensitivity of the system to

design and environmental parameters can be assessed in order to maximize the % of time the system meets the performance specifications.

3. Conclusion

Numerical and analytical strategies of estimating mirror and dome seeing have been presented. Coupled with a wind buffeting model, they can identify the range of acceptable wind speeds that minimize the combined local seeing caused by an enclosure, provide critical insight into enclosure design and mirror passive ventilation and become useful design tools for the next generation of large telescopes such as TMT and LSST.

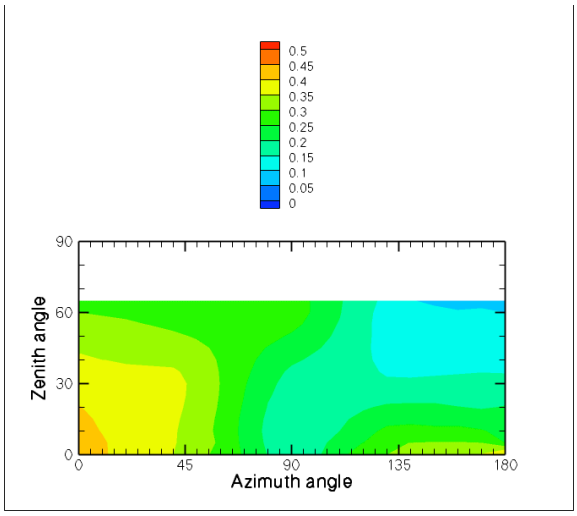

Fig. 1 Normalized M1 velocity map

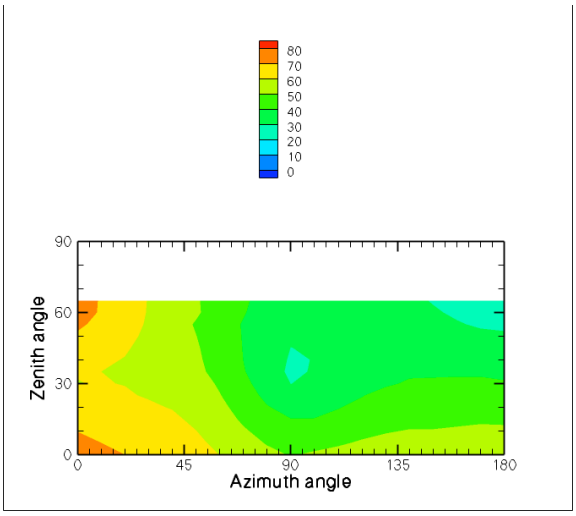

Fig. 2 Dome seeing map in mas

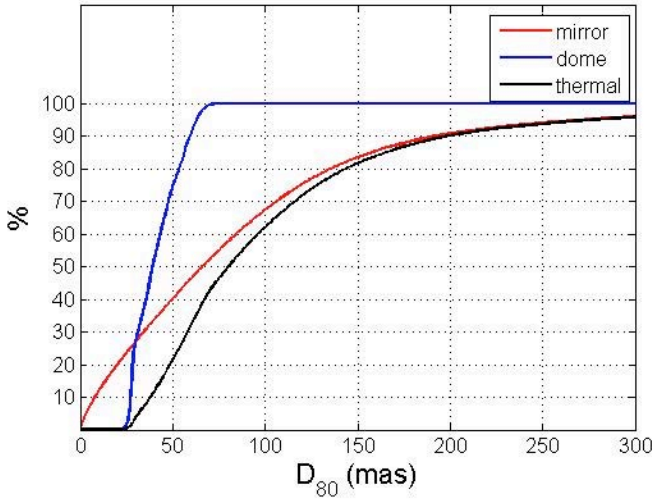

Fig. 3 Cumulative distribution probabilities of mirror, dome, and combined thermal seeing in mas

Acknowledgments
The authors gratefully acknowledge the support of the TMT partner institutions. They are the Association of Canadian Universities for Research in Astronomy (ACURA), the California Institute of Technology and the University of California. This work was supported as well by the Gordon and Betty Moore Foundation, the Canada Foundation for Innovation, the Ontario Ministry of Research and Innovation, the National Research Council of Canada, and the U.S. National Science Foundation.

References

MacMynowski, D. G., K. Vogiatzis, G. Z. Angeli, J. Fitzsimmons, and E. J. Nelson, 2006: Wind Loads on Ground-Based Telescopes. *J. Applied Optics,* **45** (30), 7912-7923.

Racine, R., D. Salmon, D. Cowley, and J. Sovka, 1991: Mirror, Dome, and Natural Seeing at CFHT. *Pub. Astr. Soc. Pac.,* **103**, 1020-1030.

Vogiatzis, K. and G. Z. Angeli, 2006: Strategies for Estimating Mirror and Dome Seeing for TMT. *SPIE 6271-27*.

Wyngaard, J. C., Y. Izumi, and S. A. Collins Jr., 1971: Behavior of the Refractive-Index-Structure-Parameter near the Ground. *J. Opt. Soc. Am.,* **61** (12), 1646-1650.

Zago, L., 1996: An Engineering Handbook for Local and Dome Seeing. *SPIE 2871,* 726-736.

Seeing Estimation from 200 mb wind speed in the ELT campaign in Morocco

Bounhir Aziza*
Département of Applied Physics, Faculty of Sciences and Techniques, BP 549,
University Cady Ayyad, Marrakech, Morocco.

Benkhaldoun Zouhair
Laboratory of High Energy Physics and Astronomy, Faculty of Sciences,
BP 2390, University Cady Ayyad, Marrakech, Morocco.

ABSTRACT

The purpose of this paper is to study wind layers, especially the 200 mb one, over a Moroccan observatory at 2760 m of altitude: Oukaimeden. The data used come from the National Center for Environmental Prediction/National Center for Atmospheric Research NCEP/NCAR Reanalysis. Statistical analyses of 200 mb wind speed since 1983 were performed. Inter comparison with the most famous observatories qualify Oukaimeden as one among the best observatories in terms of 200 mb wind statistics. A record of seeing measurements during the years 2003 and 2004 were analysed. It comes out from this study that the daily values of seeing of year 2003 correlate with 200 mb wind speed whereas the year 2004 gives no specific relationship. A long term record was needed to get more insight about the relation between wind speed at 200 mb and seeing. For that reason we have performed statistical analysis of 200 mb wind speed and seeing over La Silla and Paranal.

Corresponding author address: Bounhir Aziza, Département of Applied Physics, Faculty of Sciences and Techniques, BP 549, University Cady Ayyad, Marrakech, Morocco.
E-mail: bounhiraz@yahoo.fr

A new model to forecast seeing and Cn2 profiles from meteorological profiles.

Herve Trinquet* and JeanVernin
Université de Nice

ABSTRACT

A statistical study, performed over 145 profiles of meteorological balloons equipped with microthermal sensors, from the ground to the midstratosphere, put into evidence the correlation between the fluctuations of the buoyancy force, the vertical shear and the C_n^2. A model is adjusted to estimate the optical turbulence strength from the macroscopic meteorological parameters at low vertical resolution. This model is presented as a new way to estimate the ground seeing and the altitude of the turbulent layers from meteorological forecast. The model performances are quantified and compared with other already defined models.

*Corresponding author address: Herve Trinquet, Université de Nice.
E-mail: trinquet@unice.fr

Climatology of Sierra Negra

Esperanza Carrasco*, Alberto Carramiñana, José Luis Avilés
Instituto Nacional de Astrofísica, Óptica y Electrónica, Tonantzintla, México

Remy Ávila
Centro de Radioastronomía y Astrofísica, Morelia, México

Omar Yam
Universidad de Quintana Roo, Quintana Roo, México

ABSTRACT

Sierra Negra, one of the highest peaks in central Mexico, is the site of the Large Millimeter Telescope. It combines high altitude (4600m) and extremely low atmospheric water content. The water vapor opacity has been monitored since 1997 with radiometers working at 225 GHz showing that the zenith transmission at the site is better than 0.89 at 1 mm during 7 months of the year and better than 0.80 at 850 microns during 3 months of the year. Here one aspect of a complementary campaign initiated in 2000 to investigate the astronomical potential of the site is reported. The first results of a comprehensive analysis of the weather data measured in situ from October 2000 to December 2006 to be used as a reference for future activity in the site, are described. The conditions at the site are benign given its altitude: the median value for the temperature is 1.1°C, for the wind velocity is 3.6 m s^{-1}, for the relative humidity during the dry season is 56% and for the atmospheric pressure is 590.1 mbar. Given the site characteristics we show that our measurements are consistent with a warm standard atmosphere model.

*Corresponding author address: Esperanza Carrasco, Instituto Nacional de Astrofísica, Óptica y Electrónica, Luis Enrique Erro 1, Tonantzintla, 72840, Puebla, México.
E-mail: bec@inaoep.mx

1. Introduction

High altitude (>4 km) sites are scarce, specially considering the requirement of tolerable meteorological conditions. Sierra Negra, located at 18° 59′ 06″ North latitude, 97° 18′ 53″ West longitude and at an altitude of 4580m, is the site of El Gran Telescopio Milimétrico/The Large Millimeter Telescope (GTM/LMT), a 50-m antenna to work between 1 - 3 millimeters. The site is in the boundary between Puebla and Veracruz states. It is located at about 100 km from the Gulf of Mexico and 300 km from the closest Pacific coast. Sierra Negra, also known as Tliltepetl, is bounded to the north east by Pico de Orizaba, known as volcan Citlaltepetl, the highest mountain in Mexico that peaks at 5610 m.

2. Data

The weather station is on 5m tower at about 200 meter from the LMT site, located at the edge of a sharp slope facing north east. The station instruments are an anemometer, temperature and humidity sensors both enclosed on a radiation shield, a control console and a data logger. Specification accuracies are typically of a few percent.

TABLE 1. Data coverage and statistics. (*) indicates same coverage as the temperature.

Parameter	minutes	duty (%)	min	max	q_1	median	q_3
Temperature (°C)							
All	2355071	71.43	-10.6	11.8	-0.3	1.1	2.4
Day (8am-6pm)	980813	71.39	-10.4	11.8	0.8	2.2	3.4
Night (8pm-6am)	980777	71.39	-10.2	6.7	-0.8	0.4	1.4
Summer (May-Oct)	1153934	72.52	-4.5	11.8	0.5	1.4	2.6
Winter (Nov-Apr)	1201130	70.39	-10.6	9.9	-1.3	0.5	2.2
Wind speed (m s^{-1})							
All	2257986	68.48	0.0	36.2	2.2	3.6	5.8
Day (8am-6pm)	947966	69.00	0.0	35.8	2.2	3.6	5.4
Night (8pm-6am)	934365	68.01	0.0	34.4	2.2	4.0	6.2
Summer (May-Oct)	110657	69.54	0.0	27.8	2.2	3.6	5.8
Winter (Nov-Apr)	115459	67.48	0.0	36.2	2.2	4.0	5.8
Relative humidity (%)							
All	2355071	(*)	1	100	43	83	100
Day (8am-6pm)	980813	(*)	1	100	50	85	100
Night (8pm-6am)	980784	(*)	1	100	36	80	100
Summer (May-Oct)	1153941	(*)	3	100	76	99	100
Winter (Nov-Apr)	1201130	(*)	1	100	22	56	90
Atmospheric pressure (mbar)							
All	2355071	(*)	567.3	603.3	589.2	590.1	591.0
Day (8am-6pm)	980813	(*)	575.6	598.0	589.2	590.2	591.1
Night (8pm-6am)	980784	(*)	567.3	599.9	589.2	590.1	591.0
Summer (May-Oct)	1153941	(*)	567.3	597.7	589.5	590.4	591.2
Winter (Nov-Apr)	1201130	(*)	575.3	603.3	588.9	589.8	590.7

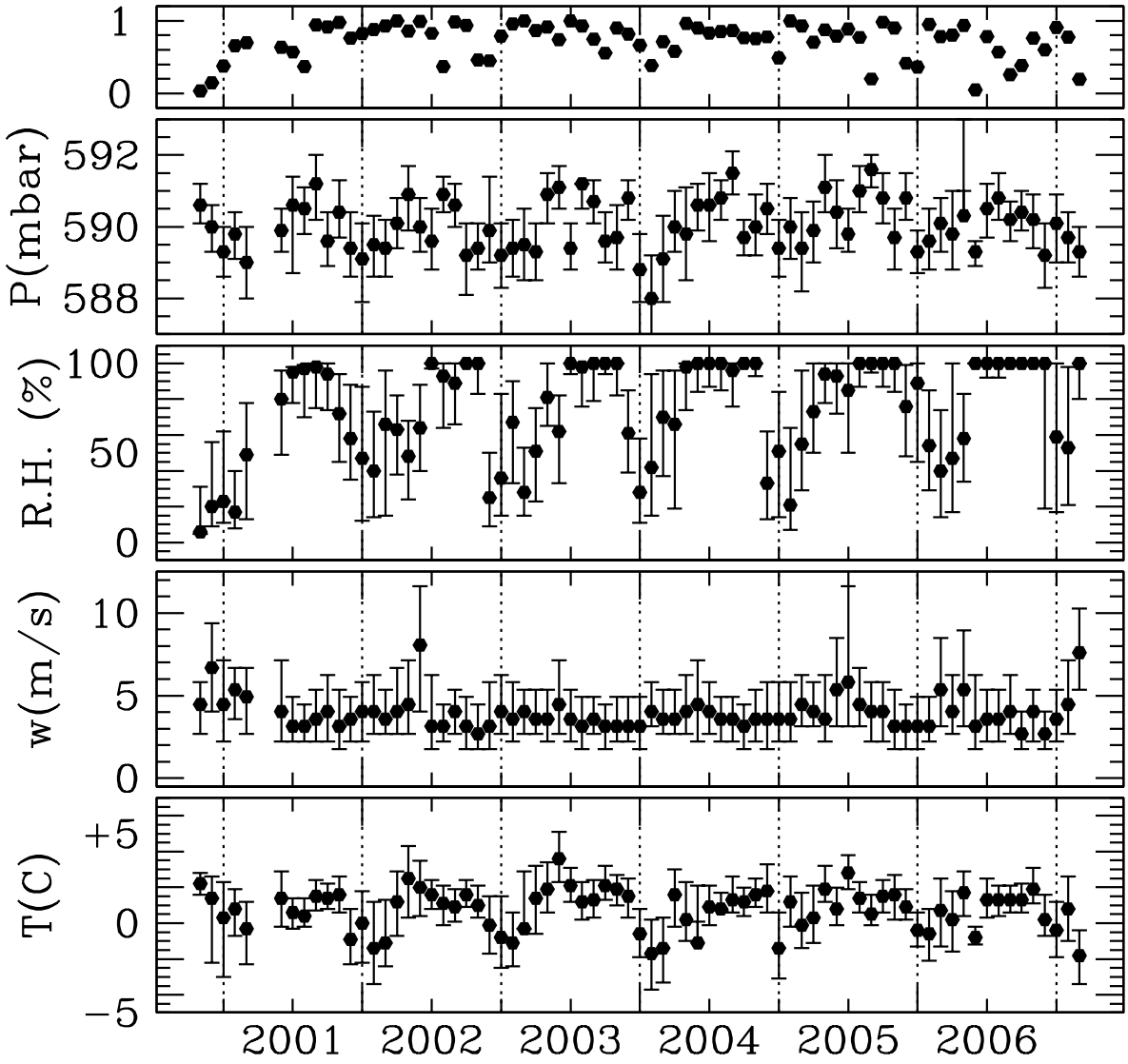

FIG. 1. Monthly statistics of all data. Points are medians with error bars going from the first to the third quartile. The upper panel is the relative coverage of each month.

Data presented here span 2289.672 days equivalent to 6.269 years. We define daytime as a 10 hr interval from 8:am to 6:pm and nighttime from 8:pm to 6:am. To coincide approximately with the dry and wet semesters of the year we define winter from November 1st to April 30, that covers 181 days, and summer from May 1st to October 31st, covering 184 days. The present data have 1185 winter days and 1105 summer days. The wind has a slightly less coverage as seen in table 1. Most of the data were taken with 1 or 5 minutes sampling and in four periods with a 30 minutes sampling.

The summary of our results are shown in table 1 where the statistics for the meteorological parameters are shown for all the data points, by day, night, summer and winter, as defined above. The first column shows the number of minutes measured, the duty column is the percentage of temporal coverage and the following columns shown the minimum, maximum, first, second and third quartile values. In figure 1, we show a summary per month of the main parameters, the top panel is the temporal coverage, in the panels below the dots are the median values and the bars go from the first to the third quartile. The temperature median is 1.1°C with a daily cycle of less than 2°C. The difference between summer and winter is less than 1°C. The minimum temperature value is -10.2 °C and the maximum 11.7°C. The wind temporal coverage is a few percentage less than for the other parameters with a wind median of 3.6 m s^{-1}. When the winds are stronger during the nights, seventy five percent of the time the wind median is less than 6.2 m s^{-1}. For the LMT, the wind speed limit to operate at 1 mm is 10 m s^{-1} that happens 90% of the time, to operate at 3 mm the wind speed limit is 25 m s^{-1} while the survival wind speed is 70 m s^{-1}. The maximum wind speed reported has been 36.2 m s^{-1} with strong winds lasting 4 hours on February 22, 2002. While the temperature, wind velocity and barometric pressure are mildly dependent of the seasons, the relative humidity is strongly seasonal dependent. During the winter months 56% of the time the relative humidity is less than 50% and a quarter of the time is extremely low, only 22%. In contrast, during the summer months a quarter of the time relative humidity is less than 76%. However, it must be pointed out that relative humidity is a local phenomena and high values do not necessarily imply that water opacity at the site is high.

The lowest layer of the standard atmosphere model has a constant temperature gradient $\theta = -dT/dz = 6.5^\circ$ C/km, resulting in:

$$T(z) = T_0 - \theta z, \quad P(z) = P_0(1 - \theta z/T_0)^\alpha, \tag{1}$$

with $\alpha = \mu m_H g/k\theta \simeq 5.256$ and $\mu = 28.9644$ the mean atomic mass of air. At Sierra Negra we measured $T(4.58$ km) = 1.1°C, which extrapolates using the canonical value of θ to $T_0 = 31$°C $\simeq 304K$. The measured pressure, $P(4.58$ km) = 590 mbar is in a very good agreement with $P = P_0(T/T_0)^\alpha \simeq 589.7$ mbar, showing that our data are consistent with what one expects for a site at the Sierra Negra altitude and latitude.

3. Conclusions

In spite of being one of the highest astronomical sites available worldwide, Sierra Negra has relatively mild temperature and wind conditions, making it a manageable site and a suitable place for scientific facilities benefiting of the thin atmosphere.

The Role of Weather Forecasts in Gemini Scientific Operations

Dennis Crabtree*, Inger Jorgensen and Michael West
Gemini Observatory, Hawaii

ABSTRACT

Over 90% of Gemini's observing time is done in queue scheduling mode. One of the advantages of queue mode is that observations can be taken in the observing conditions required by the science. For example, adaptive optics observations can be taken on nights of good seeing and mid-IR observations can be done during periods of low water vapor. We will discuss the use of current weather products available in Hawaii and Chile in nightly planning of Gemini's queue observing. We will also look ahead and discuss additional products that help Gemini's science operations.

Corresponding author address: Dennis Crabtree, Gemini Observatory, Hawaii.
E-mail: dcrabtree@gemini.edu